Development of New Position-Sensitive Detectors for Positron Emission Tomography

高性能位置検出器の開発とポジトロン・エミッション・トモグラフィーへの応用に関する研究

Takeji Yamashita

山下 武司

Development of New Position-Sensitive Detectors for Positron Emission Tomography

Takaji Yamashita

Ph. D. Thesis

Manuscript Date : August, 1993

ACKNOWLEDGMENTS

First of all, I wish to express my thanks to Professor Mikio Takagi of Institute of Industrial Science, University of Tokyo for giving me the opportunity to accomplish this dissertation and also for his guidance and helpful suggestion. I also thank many professors of University of Tokyo; Professor Masao Saito of Institute of Medical Electronics, Faculty of Medicine, Professors Kunio Tada and Takeshi Kamiya of Department of Electronic Engineering, Faculty of Engineering, and Professor Mitsutoshi Hatori of Department of Information and Communication Engineering, Faculty of Engineering, for their useful advises and guidance.

This work has been performed as an R&D program of Hamamatsu Photonics K.K. during the last fifteen years. I would like to thank Mr. Teruo Hiruma, President of Hamamatsu Photonics K.K., and Dr. Yoshiji Suzuki, Director of Central Research Laboratory of Hamamatsu Photonics K.K., for their support for this work.

I have been fortunate to work with extremely talented people. I especially wish to thank Dr. Eiichi Tanaka of Hamamatsu Photonics K.K., for his very useful discussion and suggestion. Dr. Tanaka was willing to impart his knowledge and skills. I am grateful for his time and effort on my behalf. I also thank Dr. Yutaka Tsuchiya, Deputy Director of the Central Research Laboratory for his kind suggestion and encouragement. He has continuously been encouraging me to accomplish this thesis in English.

I acknowledge Drs. Norimasa Nohara, Takehiro Tomitani, Mikio Yamamoto and Hideo Murayama of The National Institute of Radiological Sciences for their useful discussions concerning PET detectors and systems. Thanks are also due to Dr. Henry N. Wagner Jr. of The Johns Hopkins University, Drs. Yukio Tateno, Toshiro Yamasaki and Osamu Inoue of The National Institute of Radiological Sciences, Associate Professor Yoshiharu Yonekura of Kyoto University, and Dr. Yasuyoshi Watanabe of Osaka Bioscience Institute for their kind advises for the development of PET from their professional knowledge and great experiences in the use of PET.

I also appreciate the interaction and support of members of The Fifth Research Group of Central Research Laboratory of Hamamatsu Photonics K.K. In particular, I'd like to thank Mr. Hiroshi Uchida for his Monte Carlo calculation and effort on the development of PS-PMT

detectors, Mr. Mitsuo Watanabe for his effort on the development of animal PET systems, Mr. Keiji Shimizu for his effort on the development of 3D detector and designing electronics, Mr. Tomohide Ohmura for his effort on the study of signal processing, Messrs. Hiroyuki Okada and Nakahiro Satoh for the mechanical design of PET systems, Messrs. Shinsuke Mori, Etsuji Yoshikawa, Hugh Lyshkow and Tsuyoshi Kosugi for their contribution to the software development, and Dr. Hideo Tsukada for his useful advises from the point of view of a researcher using PET.

I also thank Mr. Shigeki Nakase of Solid State Division and Mr. Yutaka Yamashita of Central Research Laboratory of Hamamatsu Photonics K.K. for their efforts on the development of measurement techniques for PET detectors. We had worked together to develop very early stage of PET detectors as an R&D program of MITI (Ministry of International Trade and Industry) for three years from 1979. Thanks are also due to Messrs. Takehiro Kurono and Tamiki Takemori of the Central Research Laboratory for their technical support through an R&D program of JRDC (Research and Development Corporation of Japan).

I acknowledge Mr. Dennis E. Persyk of Siemens Gammasonics for his educating me scintillation detectors and a great American life. I also thank Mr. James K. McCormick of Hamamatsu Corporation for his introducing me to many researchers in PET and also teaching me English. My experience in the U.S.A. from 1978 to 1980 was the most fruitful and pleasant time in my life.

I have benefited greatly from the efforts of many people in Electron Tube Division of Hamamatsu Photonics K.K. I especially thank Mr. Jun-ichi Takeuchi, Director of the First Electron Tube Division for his understanding our demands for PMTs and kindly supporting our studies by offering new devices. Thanks are also due to Mr. Shin-ichi Muramatsu of Electron Tube Division for his skillful manufacturing of new PS-PMTs and improving them according to our request.

Thanks are due to Mr. Toshihiko Ryuo of Shin-Etsu Chemical for his cooperation in trial manufacturing of new BGO arrays, and Dr. Charles L. Melcher of Schulumberger-Doll Research for the loan of an LSO crystal.

I thank Mr. Keith Jeffries of The Johns Hopkins University for making corrections on English in a draft of this thesis.

Finally, I am deeply indebted to the late Professor Tatsuro Hayashi of Hamamatsu University School of Medicine for his contribution to our work in this field. I had worked under him for ten years since I joined Hamamatsu TV Co. Ltd. (the former name of Hamamatsu Photonics K.K) in 1974. I would like to thank him for his contribution to my education in detection of photons, photodetectors, methods for research and development, and also the philosophy of life through his way of life.

A part of this work was carried out through R&D programs supported by MITI and JRDC.

TABLE OF CONTENTS

LIST OF ILLUSTRATIONS

LIST OF TABLES

ABSTRACT

Positron Emission Tomography (PET) has been used for the last two decades to obtain functional images with positron-emitting radiotracers in the body. PET is expected to be a very promising tool for both basic and clinical research, because it makes possible the study of regional chemistry within multiple organs of the body in living human beings and experimental animals. As PET has become to play an important role in research and clinical fields, the demand for improving system performance has increased. In response to this demand the imaging properties of PET have improved significantly, but there still exists a strong demand for better quality of images. Many efforts in PET instrumentation have been directed toward higher spatial resolution to obtain more accurate and quantitative information of distributions of radioactivity. Spatial resolution achieved with current PET systems is, however, limited to a great extent by the intrinsic resolution of the detector. The intrinsic resolution achieved with the detectors developed up to the present is still far from the theoretical limit of the spatial resolution of PET (1.5 mm - 2.0 mm).

The work presented here describes new PET detectors that brought better system performance characteristics including spatial resolution. To overcome the difficulty to improve the resolution with the conventional schemes of detectors, a new scheme of high resolution block detector has been developed which consists of small segments of a bismuth germanate (BGO) array and a position-sensitive photomultiplier tube (PS-PMT). The coincidence detector resolution of less than 2.0 mm in full width at half maximum (FWHM) was achieved with the new detector, which is very close to the theoretical resolution limit of PET system.

Several attempts have been pursued to improve the performance of the block detector using the PS-PMT for a practical use, and a high resolution PET system dedicated to animal studies has been developed, to which the block detector was applied. A spatial resolution of 3.0 mm was achieved with the animal PET system, and it was confirmed that the new scheme of detector could provide the superior performance characteristics to the conventional detectors.

As a further development of the position-sensitive detector scheme, two kinds of PET detectors were proposed which providing the system with uniform resolution over the entire field of view. In high resolution PET systems using thin slender crystals, the radial resolution degrades toward the peripheral field of view because of a parallax error. The proposed detectors can detect the depth-of-interaction of γ-rays in the scintillators, so that they can reduce the parallax error and thus improve the resolution uniformity. One of the proposed detectors has bundled pillar shaped BGO elements coupled to two PS-PMTs at their both ends. A prototype detector module was constructed using 32 BGO pillars and preliminary experiments have been carried out. The detector showed little variation of spatial resolution for different angles of γ-ray incidence. The other new detector consists of the PS-PMT and a block BGO crystal having comb-shaped slits in it. The detector can provide a single bit of depth information of γ-ray interaction in the BGO block as well as the position information. Since the detector structure is very simple, it can be easily applied to the animal PET system mentioned above.

As a future prospect, it is desired to develop detectors for three dimensional PET (3D-PET) and Clinical PET. Removal of interplane septa in the 3D-PET, combined with the acceptance of all possible coincidences over the axial field of view, increases the sensitivity dramatically, while the increases of single events, scattered and accidental coincidence events are much larger than that of true coincidence events. Detectors for 3D-PET are strongly required to have a higher count rate capability, better time and energy resolution than those for the conventional 2D-PET. A multi-anode PS-PMT and a small size of PS-PMT having improved dynodes are the possible detectors for this application.

Chapter 1

Introduction

Positron Emission Tomography (PET) is an important Nuclear Medicine Technique, which is used to determine the distribution of the administered tracer substances labeled with positron emitting nuclides. It is continually evolving as a valuable tool for the study of biological functions and diseases. The imaging properties of PET have improved significantly, but there still exists a strong demand for better quality of images, especially for better spatial resolution.

This dissertation will focus on the radiation detectors for 511 keV annihilation γ-ray detection. In particular, new detector schemes yielding better spatial resolution for PET will be described. The goal of the research described here is to develop novel detectors for better PET instrumentation, where the emphasis is especially placed on their development for a practical use in PET. The new detectors use small segments of a bismuth germanate (BGO) array and a position-sensitive photomultiplier tube (PS-PMT).

1.1 Positron Emission Tomography : PET

1.1.1 Basic Principle of PET

Positron Emission Tomography (PET) is a three dimensional imaging technique that noninvasively measures the concentration of radiopharmaceuticals in the body that are labeled with positron-emitting nuclides. As the changes of the radiotracer distribution in a living tissue are also obtained with a temporal resolution of ten seconds to several minutes, PET provides four dimensional information; three dimensions in space and one dimension in time.

The radioisotopes used for PET studies are produced by a cyclotron that adds positive charges (protons) to stable isotopes by high-energy bombardment of the stable nuclei with protons or deuterons. The primary positron-emitting radionuclides used in biological studies are oxygen-15 (half life $t_{1/2}$, 2 min), nitrogen-13 ($t_{1/2}$, 10 min), carbon-11 ($t_{1/2}$, 20 min), and fluorine-18 ($t_{1/2}$, 110 min). The nuclear reactions to produce these positron-emitting nuclides are summarized in Table 1-I.

Table 1-I Nuclear reactions to produce positron-emitting nuclides

Nuclide	Nuclear Reaction
C-11	^{10}B (d, n) ^{11}C
	^{14}N (p, α) ^{11}C
N-13	^{12}C (d, n) ^{13}N
	^{16}O (p, α) ^{13}N
O-15	^{14}N (d, n) ^{15}O
F-18	^{18}O (p, n) ^{18}F
	^{20}Ne (d, α) ^{18}F

When a positron-emitting nuclide decays in the body, the nucleus rids itself of the excess positive charge by emitting a positive electron (positron), which loses its energy through multiple collisions with electrons in the surrounding tissue. After losing most of its kinetic energy, it combines with one of these electrons and annihilates. In the annihilation process, the masses of the electron and positron are converted into electromagnetic radiation in the form of two equal γ-rays (511 keV). They are emitted at 180° to each other under restriction of momentum conservation law. A pair of annihilation γ-rays can be detected externally using the coincidence technique as shown in Fig.1-1.

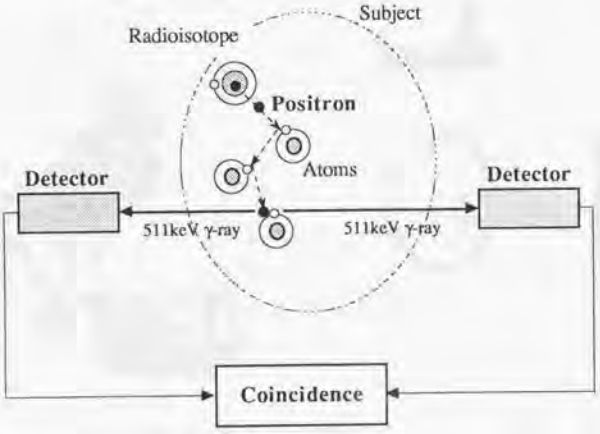

Fig.1-1 Schematics of positron annihilation and coincidence detection

Considerable advantages of utilizing positron-emitting labels can be achieved through the coincidence collimation of the annihilation radiation, which include high efficiency and constant sensitivity for the sources lying between two opposite detectors.

Current PET systems consist of one or more circular rings of detectors which surround the subject. A coincidence event between two detectors on a ring across the subject defines a line along which the positron annihilation must have occurred. Millions of coincidence counts between the thousands of possible combination of detectors are collected and stored on storage media such as computer memories or a hard disk. As data is acquired, the coincidence

detector pair address is rearranged into projection data for each coincidence ray angle which is called a "sinogram." It permits the reconstruction of the positron distribution in the body through a mathematical procedure such as a filtered back projection technique, which is familiar in X-ray computed tomography (X-ray CT). Figure 1-2 illustrates the principle of PET, its detector construction and image formation.

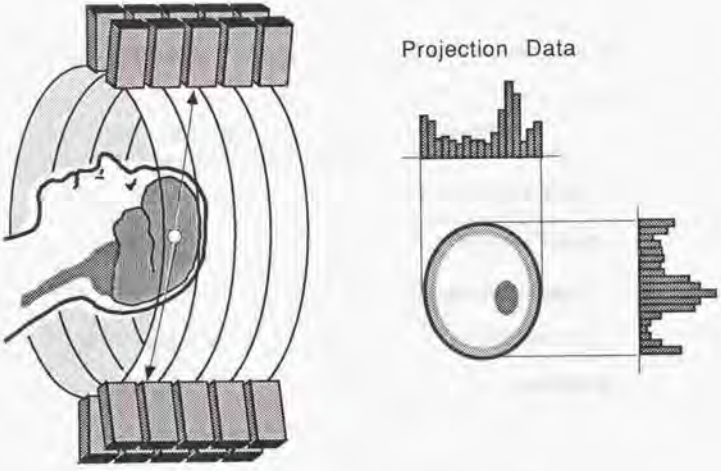

Fig.1-2 Principle of PET : detector construction and image formation

1.1.2 Tracers Labeled with Positron Emitters

Positron-emitting nuclides including carbon (^{11}C), oxygen (^{15}O), and nitrogen (^{13}N) are useful for nuclear imaging because stable elements of these nuclides are naturally contained in the pharmaceuticals or biological compounds to be labeled, therefore not introducing any alien to the compounds to be measured. The choice of nuclides, C, N, O being the most naturally abundant biological elements, means that almost any biologically present substance, such as water or glucose can be labeled and traced within the organism in question. Fluorine (^{18}F) can be used as a substitute for hydrogen (H) or other functional groups. There is the potential for

developing tracer materials for investigating a wide range of physiological functions. Thus, with the proper tracer compounds labeled with positron-emitting nuclides, PET can be used to measure metabolism, blood flow, or other physiological values *in vivo*. More than 200 biological substances, their analogs and other drugs have been labeled by ^{11}C, ^{13}N, ^{15}O and ^{18}F. A partial list of the compounds labeled with positron-emitting nuclides is shown in Table 1-II.

Table 1-II Example of compounds labeled with positron emitters

Labeled Compounds	**Applications**
$H_2{}^{15}O$, $C^{15}O_2$, $^{13}NH_3$	Cerebral blood flow
^{11}CO, $C^{15}O$	Cerebral blood volume
$^{15}O_2$	Oxygen consumption
^{18}F-fluorodeoxyglucose	Glucose metabolism
^{13}N-amino acids	Amino acid metabolism
^{11}C-N-methylspiperone	Dopamine D_2 receptor
^{11}C-Ro15-1788	Benzodiazepine receptor

1.1.3 Medical and Research Use of PET

Significant advances in understanding the normal and diseased organs including the brain have been achieved with PET by many investigators. PET can measure noninvasively the functional activity in humans, and can image the working parts of the organs. PET studies are categorized into three types; studies on regional blood flow, substrate metabolism, and chemical recognition sites such as receptors and enzymes. Regional mapping of blood flow and metabolism in the brain has led to a better understanding of strokes and brain tumors. The development of agents to measure neurotransmission systems within the brain is expected to

bring new insights on brain abnormalities in psychiatric and degenerative brain diseases. PET is now used to study a large number of disorders, including schizophrenia, epilepsy, depression, Parkinson's disease, Alzheimer's disease, and Huntington's disease. Studies in the heart using PET are useful techniques for assessing damage to heart muscle following infarct. A number of PET studies have demonstrated the value of PET for assessing the effects of therapy on tumors. PET can be used not only to detect disease, but also to plan its treatment and monitor the effectiveness of the treatment.

Researchers are also using PET to examine the response of the human brain to various psychological or physiological stimuli, e.g. changes in local glucose metabolism or blood flow in response to some stimulus. It is also expected to use PET for studies of higher cognition functions such as learning, thinking, and memory.

Some researchers have applied PET to basic studies using experimental animals. The functional map of monkey brains has been studied using micro electrodes by many researchers in neurophysiology. While the measurements using micro electrodes provide neuronal activities point-by-point in the brain, PET provides three dimensional images of brain functions with blood flow or glucose metabolism. On the contrary, the temporal resolution of PET for this application is 40 - 90 seconds, while the micro electrodes can pick up neuron activities in a millisecond range. Thus PET may be used in combination with the micro electrodes complementarily. The other possible application of PET to animal studies is investigation of drug efficacy and behavior *in vivo*. New organic compounds or drugs can be evaluated or screened through the animal experiments with PET, before their administration to human subjects.

1.1.4 Feature of PET: Advantage and Limitation

PET is a scientific tool for *in vivo* studies for biological and physiological process in the body. PET is unique because it allows examination of a particular chemical species. On the other hand, magnetic resonance imaging (MRI) or X-ray CT provides anatomic information about tissue density (X-ray CT), proton density (MRI) and spin lattice relaxation time (MRI). Since much disease has a chemical origin, biochemical changes due to disease are often prior to changes in organ size, position or density. PET has, therefore, a capability to measure the

disease due to biochemical changes in the tissue long before MRI or X-ray CT scans show any evidence of disease. Another advantage of PET is the use of radioactive tracers, because the tracer technique is extremely sensitive to small concentration of chemicals to be measured; for example it can measure picomol or subpicomol receptors in the body. Magnetic resonance spectroscopy (MRS) imaging may be a competitive technique with PET, but continues to suffer from poor sensitivity and spatial resolution; it requires long observation time (30 minutes to hours) to obtain an image with 1 - 2 cm resolution.

PET is often compared to single photon emission tomography (SPECT) which also utilizes radio-tracers and thus provides functional information. If we compare their performance, PET is evidently superior to SPECT by virtue of the use of positron-emitting radiotracers:

- More freedom in synthesis of tracers (especially with ^{11}C)
- Mostly non-analog tracers
- Shorter decay time of the tracers
- Less absorption of γ-rays in the body
- Quantitative measurement thanks to exact attenuation correction for γ-rays
- Higher sensitivity due to electronic γ-ray collimation instead of using mechnaical colliamtors

PET studies require a number of researchers and assistant staffs; medical doctors, chemists, physicists, nurses and technicians. PET studies also consume much expenses including personnel and material expenses, and that of depreciation for instrument, nevertheless the number of PET studies per day is limited. Those factors above now limit a wide scale of clinical application of PET. Most PET systems used in the field have spatial resolutions of 5 - 7 mm, while that of MRI or X-ray CT is less than 1.0 mm: The temporal resolution of PET is 10 - 40 seconds, while that of X-ray CT is several seconds or even less than a second. Those immature performance of PET also limits its wide use in research and clinical fields.

1.2 PET Performance Criteria

1.2.1 Spatial Resolution

There are two fundamental factors limiting the spatial resolution of PET; the effect of non-colinearity of annihilation γ-rays and the effect of finite range of positrons traveling in the tissue before annihilation. Although the two annihilation γ-rays emerge nearly back-to-back, there is a small angular deviation that depends on the material within which the annihilation event occurs. The angular deviation spread is expressed by a Gaussian function of which the full-width at half-maximum (FWHM) is approximately 0.5° [1]. Thus the amount of resolution loss in the PET images is proportional to the detector ring diameter. This effect will range 1 mm for a 50 cm diameter to 2 mm for a 100 cm diameter tomograph. The resolution loss due to the positron range depends on the energy of positrons. The degradation on the FWHM resolution is relatively small (< 1 mm) for positron energy less than 1 MeV, i.e., ^{18}F (0.649 MeV) and ^{11}C (0.968 MeV), and moderate (1 - 2 mm) for energies from 1 MeV to 2 MeV, i.e., ^{13}N (1.22 MeV) and ^{15}O (1.68 MeV) [2][3].

Although there exist physical limitations above, the spatial resolution of current PET systems is limited to a great extent by the intrinsic resolution of the detector which depends primarily on the width of scintillators. A major technical obstacle to obtaining narrower detectors has been the unavailability of photomultiplier tubes (PMT) small enough to couple efficiently to narrow scintillators.

The resulting spatial resolution achievable in a PET system is determined by the following factors: the angular deviation of annihilation γ-rays, the positron range effect, the intrinsic detector resolution, geometry of the detector arrangement, and other factors relating to image reconstruction such as data sampling density, pixel size in images and frequency characteristics of reconstruction filters.

1.2.2 Counting Statistics and PET Performance

Spatial resolution, sensitivity, signal-to-noise-ratio (S/N), and temporal resolution are all of prime importance as PET performance characteristics. They are related to each other through

the counting statistics (Fig.1-3), because PET images are reconstructed from sinogram data which is a two dimensional histogram of counting events.

Intrinsic spatial resolution of the system is defined in the condition that a large amount of events are accumulated and the statistical accuracy of the data is good enough. In the practical use of PET, however, both the data acquisition time and the dose to a patient are limited, so that the statistical noise degrades the image quality.

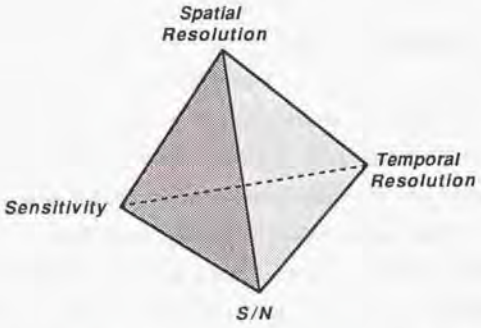

Fig.1-3 Relation of PET performance through counting statistics

The S/N ratio (S/N) at the center of a three dimensional image of a spherical object (diameter d) is related to the total counts obtained (n_t) and the effective resolution element size (r) by the formula [4]-[6]:

$$S/N = k\sqrt{n_t} \times \frac{r^2}{d^2}, \qquad (1\text{-}2\text{-}1)$$

where k is a constant. To improve the spatial resolution by a factor of two, while maintaining the same S/N ratio, it is necessary to increase the total counts accumulated by a factor of 16.

To improve the S/N ratio, spatial smoothing is often introduced through the image reconstruction process or after forming an image, and consequently degrades the image resolution. It is desirable to acquire the counting data as much as possible during a certain

period for attaining statistical accuracy. Thus the system sensitivity is important to obtain high resolution images.

The shortest period to acquire the counting data much enough to form reasonable quality of images is the temporal resolution of PET system. In general, a high sensitivity system provides good temporal resolution. A high spatial resolution image is hard to obtain in a short temporal frame due to the limitation of total number of counts collected.

1.2.3 Background Noise in PET Measurement

In considering S/N in images, there are two major noise components besides the statistical fluctuation of the acquired counts, which are scattered coincidence events and accidental coincidence events. Some of the annihilation photons have an interaction of Compton scattering in human tissue, and most of those are scattered in the forward direction. The origin of scattered events is all parts of the body that are simultaneously in line of sight with two coincident detectors. In a PET system, the coincidence events are distinguished by whether the two events occur within a certain time window (coincidence time window). Because of the finite width of the time window, there is a probability that unrelated photons accidentally produce the coincidence signals. For a given detector geometry, the true coincidence rate (R_t), and the accidental coincidence noise rate (R_r) are expressed by $R_t = k_t \varepsilon^2 A$ and $R_r = \tau\, k_s^2 \varepsilon^2 A^2$, respectively, where k_t and k_s are constants, ε is the detector efficiency for incident γ-rays, τ is the coincidence time window width, and A is the activity in the object. From these equations, we have

$$\frac{R_r}{R_t} = \tau \left(\frac{k_s}{k_t} \right)^2 \frac{1}{\varepsilon^2} R_t \qquad (1\text{-}2\text{-}2)$$

The accidental coincidence rate is proportional to the coincidence time window. Since the coincidence time window is usually set to a value slightly larger than the FWTM (full-width at tenth-maximum) of the coincidence time resolution of the detectors, timing properties of the detectors are important to decrease the accidental to true coincidence ratio.

If we define the useful maximum true coincidence rate ($R_{t\,max}$) by the true coincidence rate at which it equals to the accidental coincidence rate, we have

$$R_{t\,max} = \frac{1}{\tau}\left(\frac{k_t}{k_s}\right)^2 \varepsilon^2. \qquad (1\text{-}2\text{-}3)$$

The equation (1-2-3) implies that the useful maximum true coincidence rate is proportional to the square of the detector efficiency.

1.3 Detector Performance Required in PET

The spatial resolution of current PET systems depends primarily on the size of the detectors. Coincidence resolution is measured by passing a point source or a narrow line source of positron emitter between coincident detectors to give a count profile as a function of position along a line perpendicular to the axis of the detector pair as shown in Fig.1-4.

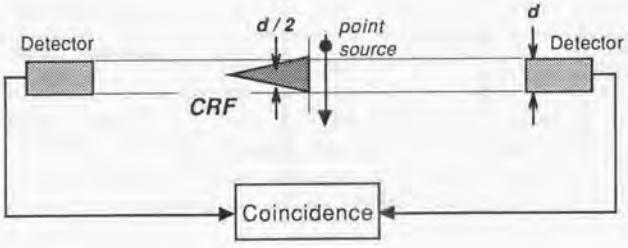

Fig.1-4 Coincidence response function (CRF) of PET detector

This profile is called the coincidence response function (CRF). The width of the CRF of detector pairs is a common measure of detector resolution in PET. A pair of rectangular detectors yield a triangle CRF at the center between the two detectors, of which the FWHM is approximately 50% of the detector width. Thus using small size of detectors is of essential importance to achieve high resolution in PET systems.

The system sensitivity of PET is directly proportional to the square of each detector sensitivity because of the use of coincidence detection. In order to detect high energy γ-rays (511 keV) efficiently, materials having both high atomic number and high density are used as scintillators. The characteristics of various scintillation materials are shown in Table 1-III.

Table 1-III Characteristics of scintillators used for PET detectors

	NaI(Tl)	BGO	GSO	CsF	BaF_2
Density (g/cc)	3.67	7.13	6.71	4.61	4.8
Linear attenuation coefficient for 511 keV γ (1/cm)	0.328	0.903	0.6	0.42	0.438
Relative light yield	100	15	27	5	5 (fast) 30 (slow)
Scintillation decay time (ns)	230	300	60	2.5	0.8 (fast) 620 (slow)
Emission peak wavelength (nm)	415	480	430	390	225 (fast) 310 (slow)
Refractive index	1.85	2.15	1.9	1.48	1.56
Hygroscopic ?	yes	no	no	yes	no

The most efficient material is bismuth germanate ($Bi_4Ge_3O_{12}$: BGO) with a linear attenuation coefficient for 511 keV γ-rays of 0.903 cm^{-1}, while the light yield is 15 % of NaI(Tl), and the decay time is 300 ns which is much longer than that of BaF_2 (0.8 ns) or CsF (2.5 ns) scintillator. To detect the weak scintillation light emitted from BGO, photomultiplier tubes (PMTs) having high quantum efficiency and high amplification gain are used as photodetectors. By virtue of the high amplification of 10^6 , the timing information can be picked up at a single photoelectron level, so that the time resolution of a few nanoseconds is achievable with the slow BGO scintillator.

It is desirable to place the detectors on a ring as closely as possible together in a PET system, because the detector packing fraction affects the system sensitivity in the same manner

as the detection efficiency of the detectors. To pack the detectors closely together on a ring, the optimum shape of the scintillation crystals is a rectangle.

The detectors for PET are also required to have fast time resolution and good energy resolution to reduce the background noise of accidental events and scattered events efficiently. The single event-rate is 50 to 100 times larger than the true coincidence event-rate, because the solid angle for coincidence event detection is much smaller than that for single event detection. When the single event-rate is high, a detector unit having a large detection area and slow scintillation decay time may cause pulse pile-up, and consequently limits the count rate capability of the PET system. Since thousands of detectors are used in one PET system, the stability of the individual detector is of essential importance. The detector performance required in PET systems is summarized in Table 1-IV.

Table 1-IV Detector performance required in PET

PET Performance	Detector Performance Required
Spatial resolution	Small detector size High stopping power (BGO)
Sensitivity	High stopping power Close detector packing (Rectangular shape)
Accidental noise	Good timing resolution
Scattered noise	Good energy resolution
Count rate performance	Short scintillation decay time Small detector unit area
Stability	Count rate independency Temperature stability Long term gain stability

1.4 Review of Detector Development for PET

1.4.1 Historical Remarks

PET has been developed through the efforts of many investigators. Since the detector performance is of prime importance in the realization of better PET instrumentation, new detectors have been developed corresponding to the system innovations.

The positron scanner was proposed in 1951 by Wrenn [7] and Sweet [8] independently, and the first system was developed by Brownell et al. in 1953 [9]. In 1959, Anger reported a positron imaging device using scintillation cameras [10]. These systems were designed and used for planar imaging of positron-emitting tracer distribution in the human body.

The first system for transverse-section positron imaging was developed by Rankowitz et al. in 1962, which used a circular array of 32 NaI(Tl) detectors [11]. The transverse-section images were reconstructed using linear superposition of backprojections (simple backprojection).

The current design of PET system was developed by Phelps and Ter-Pogossian et al. in 1975 (PETT II) [12][13]. It consisted of a hexagonal array of NaI(Tl) detectors and utilized a Fourier-based CT algorithm with attenuation correction. Phelps et al. reported the first whole body PET (PETT III) in 1976 [14]. This system was subsequently redesigned and commercially produced as ECAT by EG&G/ORTEC.

In 1976, Cho et al. developed a circular ring PET system employing 64 NaI(Tl) detectors [15]. Circular ring PET systems have also been developed by Yamamoto et al. in 1977 [16], by Bohm et al. in 1978 [17], and by Derenzo et al. in 1979 [18]. Tompson et al. used BGO detectors in the PET system for the first time [19], while the introduction of the BGO detectors for a PET system was originally proposed by Cho et al [20].

The first PET systems having multiple-slice imaging capability include the system developed by Brownell et al. in 1977, which was a dual-headed planar camera having two dimensional detector arrays [21]. Muhllehner et al. also developed a dual-headed rotating scintillation camera system for positron imaging in 1976 [22]. Multiple-layer detector ring PET

systems (PETT IV and PETT V) have been developed by Ter-Pogossian et al. in 1978 [23][24]. PETT IV had a hexagonal arrangement of NaI(Tl) cylindrical detectors and was a system for whole body studies, while PETT V had a circular arrangement of NaI(Tl) detectors and was designed for brain studies. Phelps and Hoffman developed a five-image plane system called NeuroECAT with BGO detectors in 1981 [25].

Ter-Pogossian et al. developed the first PET system (Super PETT) utilizing time-of-flight (TOF) information of annihilated γ-rays in 1981 [26], where the employment of a TOF technieque and fast CsF scintillators for PET was originally proposed by Allemand et al. in 1980 [27].

A circular PET using small BGO detectors (Neuro PET) was developed for brain studies by Brooks et al. in 1980 [28]. Circular ring BGO systems were also developed, by Carroll et al. of Cyclotron Corporation in 1979 [29], by Nohara et al. in 1980 [30], and by Eriksson et al. with Scanditronix in 1982 [31]. Kanno et al. have developed a hybrid PET/SPECT system using NaI(Tl) detectors in 1981 [32]. Hitachi and Shimazu in Japan, and AECL in canada developed commercial PET systems in 1980 -1982.

In 1983, Muhllehner et al. developed a hexagonal arrangement of NaI(Tl) bar detectors each which was one dimensional scintillation camera [33]. It was extended to a multi-ring system by applying two dimensional detectors (PENN-PET).

NaI(Tl) detectors had been gradually replaced with BGO detectors, because BGO has the capability of providing better spatial resolution and higher efficiency. CsF and BaF_2 detectors were used in fast PET systems, which may be adequate for an application to cardiac studies. The use of PET has gradually moved toward clinical applications from a research stage. According to the increasing clinical application of PET, various commercial PET systems have been developed, most of which are whole-body scanners. At present, the spatial resolution achieved in the current commercial PET systems is 4.0 mm - 6.0 mm.

1.4.2 Recent Development of PET Detectors

A major concern in recent PET design is spatial resolution. In order to improve the spatial resolution in PET, the size of the scintillators has become smaller. Various scintillator/PMT coupling schemes have been proposed to efficiently detect the scintillation light from small

scintillators. The simplest scheme is individual BGO/PMT coupling in one-to-one correspondence, which potentially provides the best spatial resolution and the highest count rate capability for the system. As the crystals become smaller, however, it becomes difficult to individually couple a PMT to a crystal because of limitations in the size of a PMT.

Derenzo et al. (1987) developed a unique detector ring geometry in which 13 mm diameter PMTs are individually coupled to 3 mm wide BGO crystals at their top, bottom or side planes [34] as shown in Fig.1-5. However, this detector construction only provided a single detector ring due to the geometrical limitation. The author et al. (1990) adopted a new multi-segment PMT to form a five ring PET system in which a BGO/PMT individual coupling scheme was used [35] as shown in Fig.1-6.

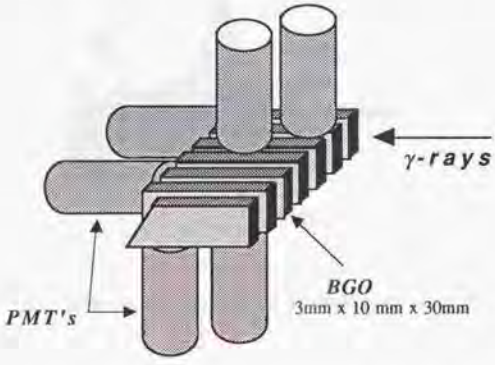

Fig.1-5 Individual BGO/PMT coupling detector developed by Derenzo et al. [34]

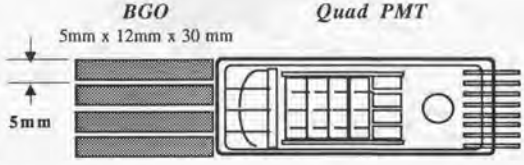

Fig.1-6 Quad-PMT detector developed by Yamashita et al. [35]

In order to overcome the difficulty in the individual coupling scheme, group coupling detectors using different coding schemes have been designed, where a large number of crystals are coupled to a small number of PMTs. Murayama et al.(1982) proposed a quad BGO detector in which four BGO crystals were coded by two PMTs [36] (Fig.1-7). Burnham et al. (1982) adopted an Anger camera scheme to a PET detector ring, where BGO crystals are coupled to a PMT array through a circular light guide [37] (Fig.1-8).

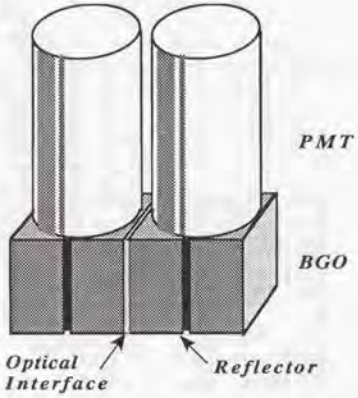

Fig.1-7 Quad-BGO detector developed by Murayama et al. [36]

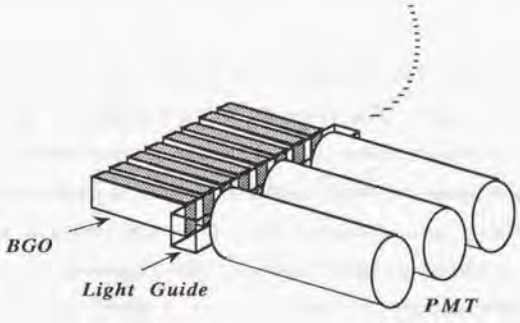

Fig.1-8 Anger camera scheme of detector developed by Burnham et al. [37]

Casey et al. (1986) developed a multi-crystal 2D modular detector using a 4x8 matrix of BGO crystals which were coupled to four rectangular PMTs through a square light guide [38]. The original design is now changed to adopting slits in a BGO block instead of the light guide and the crystal array has changed to an 8x8 matrix (Fig.1-9).

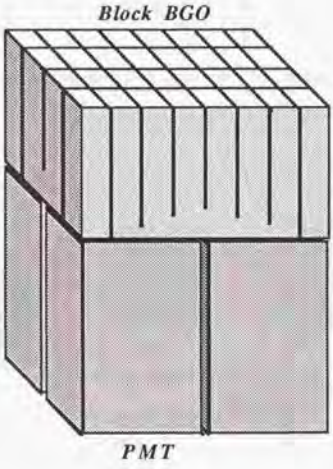

Fig.1-9 Two dimensional BGO block detector developed by Casey et al. [38]

A dual segment PMT, Hamamatsu R1548, was originally developed to provide a PET detector using an individual coupling scheme (the author et al., 1982 [39]). Since then, many researchers have proposed a variety of detectors using the dual segment PMTs coupled to a BGO array in different manners: Roney et al. (1984) coupled four wedge shape BGO crystals to the PMT, where the glass window of the PMT was used as a light guide [40] (Fig.1-10), Yamamoto et al. (1986) developed a unique design of twisted light guides to code eight BGO crystals with one dual PMT [41] (Fig.1-11), Erickson et al. [42] (1987) and Min et al. [43] (1987) developed a 2D modular detector using a 4x4 BGO matrix and two dual PMTs (Fig.1-12).

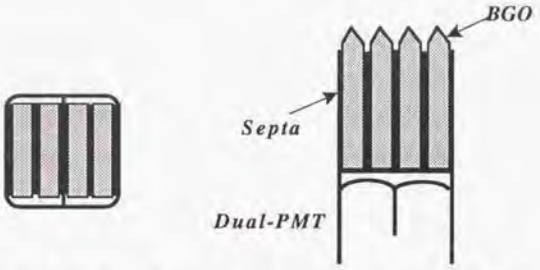

Fig.1-10 Coding scheme using dual-PMT by Roney et al. [40]

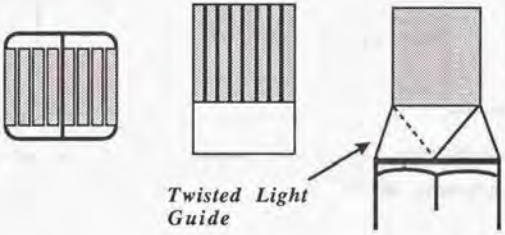

Fig.1-11 Coding scheme using dual PMT by Yamamoto et al. [41]

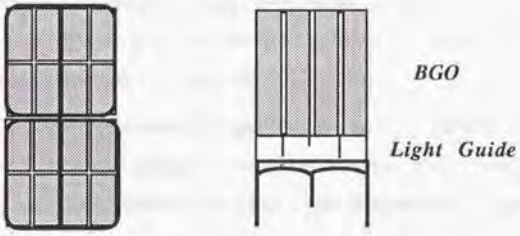

Fig.1-12 Coding scheme using dual PMTs by Eriksson et al. [42]

Moreover, various unique ideas have been introduced to PET detectors. Erickson et al. (1983) proposed a Phoswich detector having a BGO and a Gd_2SiO_5 (GSO) crystals coupled to a 13 mm diameter PMT, where either of BGO/GSO crystals was identified by means of a pulse shape discriminator [44] (Fig.1-13 (a)). Murayama et al. (1984) also developed a coding scheme using a pulse shape discriminator and a unique design of half-gated PMT [45] (Fig.1-13 (b)).

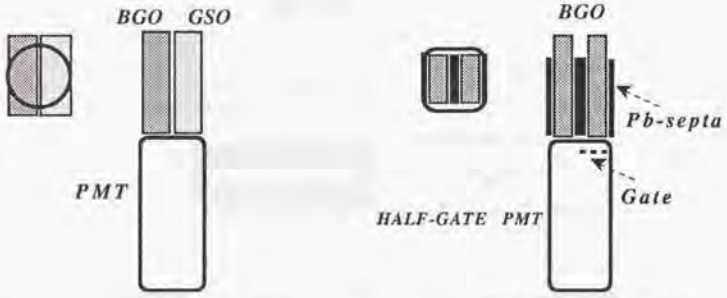

(a) BGO/GSO phoswich detector developed by Erikson et al. [44]

(b) Half-gate PMT detector developed by Murayama et al. [45]

Fig.1-13 Coding schemes using pulse shape discriminators

Derenzo et al. (1989) proposed a use of silicon photodiodes to identify a flashed segment among BGO crystals and the depth information of γ-ray interactions in each BGO, where a small PMT was used to detect timing and energy information [46] (Fig.1-14). Lightstone et al. (1986) developed a detector module having two BGO crystals, each which was individually coupled to an avalanche photodiode [47] (Fig.1-15).

Bateman et al. (1983) applied multi-wire proportional chambers (MWPC) to PET, which employed a stack of 21 lead foil cathodes sandwiched between MWPC anode planes [48]. Mine et al. (1987) proposed an application of a BaF_2-TMAE multi-wire chamber detector to PET [49]. The wire chamber contains a mixture gas of tetrakis-(dimethylamino)-ethylen

(TMAE) and a quencher, where the TAME gas is ionized by 220 nm scintillation photons emitted from BaF_2.

The development of various PET detectors is summarized in Table 1-V.

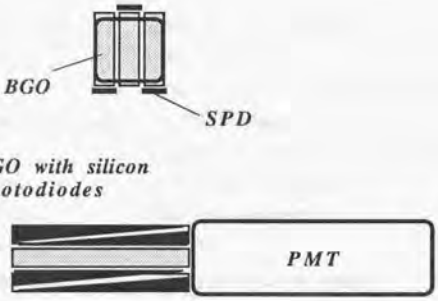

Fig.1-14 Hybrid detector composed of PMT/BGO/SPD proposed by Derenzo et al. [46]

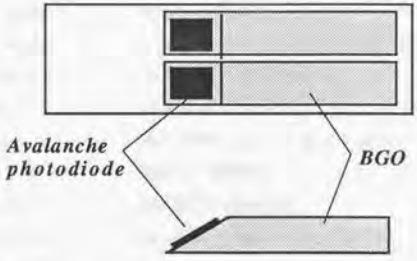

Fig.1-15 BGO/APD detector developed by Lightstone et al. [47]

Table 1-V Development of Detectors for PET

1951	F.R.Wrenn, W.H.Sweet	NaI probe pair detector
1959	H.O.Anger et al.	Gamma camera and single probe
1969	G.L.Brownell	Opposing bank of detectors (NaI probe array)
1977	G.Muehllehner et al.	Opposing gamma cameras
	S.E.Derenzo et al.	NaI+Light guide
	Z.H.Cho	Proposal of BGO scintillator for PET
1978	M.M.Ter-Pogossian et al.	Bar NaI between PMTs
		Cascade NaI blocks coded by two PMTs
1980	R.Allemond et al	Proposal of CsF detector for TOF PET
1982	H.Murayama et al	Quad BGO detector
	T.Yamashita et al.*	Dual PMT
1983	G.Muehllehner et al.	Hexagonal NaI bar camera
	L.Erikson et al	BGO/GSO poswich detector
	J.E.Bateman et al	Stack MWPC
	M.Laval et al	BaF_2 detector
1984	C.A.Buhnham et al	Small BGO coded by PMT array through LG
	H.Murayama et al.	Half-gated PMT
1986	H.Uchida et al.*	PS-PMT + Mosaic BGO
	M.W.Casey et al.	4x8 BGO block detector
	A.W Lightstone et al.	APD + BGO
	S.Yamamoto et al.	8 BGO + twisted LG + dual PMT
	S.E.Derenzo et al.	BGO-PMT 1:1 coupling
1987	L.Erikson et al.	4x4 BGO array + LG + dual PMTs
	H.B.Min et al.	4x4 BGO array + dual PMTs
	P.Mine et al.	BaF_2 + MWPC
1989	K.Shimizu et al.*	3D BGO detector
	S.E.Derenzo et al.	Wedge shape PD and PMT
1991	T.Yamashita et al.*	4 segment PMT
	T.Yamashita et al.*	Comb-slit BGO + PS-PMT

* Developed by the author of this thesis, et al.

1.5 Proposal of New Detector Scheme

1.5.1 Discussion of Detector Schemes

As reviewed in Section 1.4.2, the PET detector schemes developed up to the present are divided into two categories, individual coupling methods and group coupling methods. The individual scintillator/PMT coupling in one-to-one correspondence is a simple scheme, but it potentially provides the best spatial resolution and the highest count rate capability. However, there is a resolution limit in this scheme due to the size of a PMT. Since the proportion of useful area on a photocathode becomes smaller with smaller PMTs, efficient optical coupling between a PMT and a scintillator is difficult to be obtained, and thus the timing and energy resolution degrade. The other drawback of this scheme is that the cost for the total detectors in a PET system is relatively high compared to that for detectors using group coupling schemes.

The use of solid state detectors such as a p-i-n silicon photodiode (SPD) or an avalanche photodiode (APD) may overcome those drawbacks, but studies of the solid state detectors for PET are still in a preliminary stage, and there exist many engineering problems to be solved for their practical uses. A SPD having a small area (e.g. 3 mm in diameter) shows a root-mean-square noise level of 300-400 electron-hole pairs equivalent combining with a low noise amplifier. As the number of BGO photons produced by a 511 keV γ-ray is 1,500-2,000, the signal pulse height is marginal over the electronic noise level. Fairly good noise discrimination is obtained only by cooling the detector, when the thermal noise is suppressed and the light amount from BGO increases as well.

The time resolution of an APD is limited by the existence of excess noise. The signal pulses from an APD are amplified through a timing amplifier of which shaping time is in a microsecond range. The band-limited amplifier suppresses the noise, while providing amplified signal pulses having a slow rise time. Because the timing pick-off is performed with those amplified pulses, the time resolution of an APD/BGO detector is poorer than that of a PMT/BGO detector. In addition, since the gain of APD is temperature dependent, the detector system requires temperature stabilization, which is not a desirable feature in the practical application to PET.

The spatial resolution attained with the coding scheme detectors is generally restricted by the size of a PMT or of its segments, and by statistical fluctuation of photon number emitted from BGO crystals. The manner by which photon statistics affect the spatial resolution in those coding schemes is similar to that in scintillation cameras, where the spatial resolution is limited by the spatial spread of the scintillation light which is optimized for the PMT size or pitch. The detector pair resolution obtained with the conventional coding schemes is 3.0 - 4.0 mm FWHM.

Detectors using MWPCs have potential capabilities of providing high intrinsic spatial resolution. The disadvantage of MWPC is its low detection efficiency for 511 keV γ-rays. Even the detection efficiency of a detector using a photosensitive MWPC coupled with BaF_2 scintillators is low. Since BaF_2 has much lower stopping power for 511 keV γ-rays than BGO, it is necessary to use long scintillators in depth in order to obtain the detection efficiency comparable to that of BGO, which results in the degradation of the spatial resolution due to Compton scattering among the crystal segments. Because of the deterioration of the TMAE gas, it is necessary to use a system to recycle the gas in the chamber, which is not a desirable feature for a practical system.

1.5.2 Advantageous Use of Position-Sensitive PMT for PET

A new approach to attain higher resolution than that in the conventional schemes is the use of a position-sensitive PMT (PS-PMT) coupled to a BGO array having small segments [50][51]. Since the PS-PMT has a very high intrinsic resolution capability, a spatial resolution less than 2.0 mm is obtained by coupling to properly designed BGO crystals. The schematic drawing of the detector using PS-PMT is shown in Fig.1-15. Scintillation photons produced in one BGO segment travel to the photocathode, and are converted to photoelectrons which are multiplied by $5x10^5$–10^6, and reach the crossed-wire anodes encoding position information. The position is calculated by a charge division method in the X and Y directions independently. Since the PS-PMT has no structural difference between the X and Y directions, it has a high resolution capability in the both directions. The other advantage is its cost effectiveness. The PMT cost normalized by the useful detection area can be decreased, and the number of read-out

electronics used in the whole system can be reduced in comparison with that in PET systems using conventional detectors.

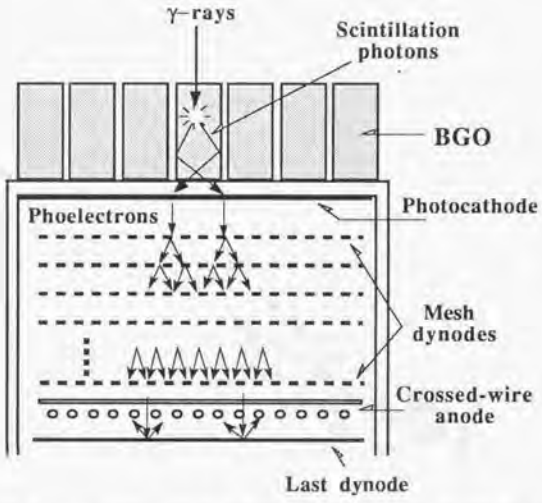

Fig.1-15 Schematic drawing of a BGO block detector using PS-PMT

A high resolution PET dedicated to animal studies has been developed using the PS-PMT. A spatial resolution of 3 mm FWHM has been achieved with this PET system. Figure 1-16 shows the evolution of spatial resolution of PET systems developed during the last fifteen years, in which the resolution achieved in the PET system using PS-PMT is also shown.

An intrinsic resolution less than 1.5 mm FWHM can be obtained with a coincidence detector pair having the PS-PMTs coupled to very narrow BGO crystals of 1.0 - 1.5 mm in width. Thus, the PS-PMT has a potential capability to provide a PET system having a spatial resolution close to a theoretical limit (1.5 mm - 2.0 mm).

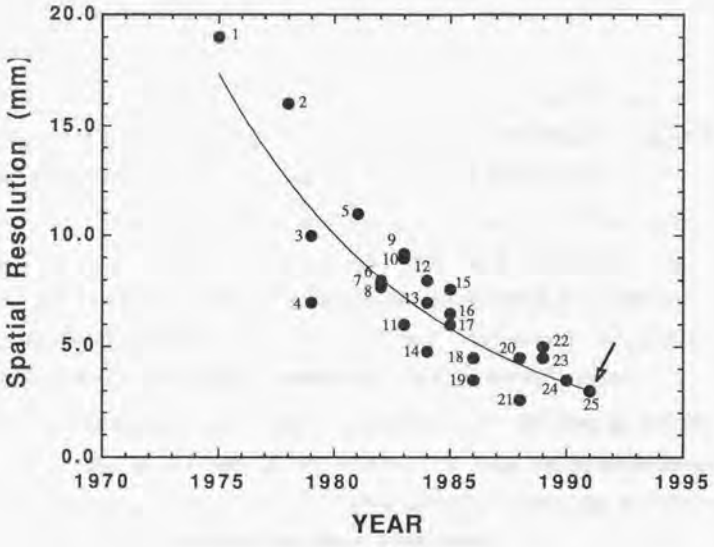

1: PETT III, 2: ECAT II, 3. Donner 280, 4: Positologica I, 5: Headtome I, 6: Neuro ECAT,
7: PETT VI, 8: Karolinska PET, 9: Neuro PET (NIH), 10: Positologica II, 11: TOF-PETT (W.U.),
12: PCR-I (MGH), 13: McMaster PET, 14: PENN PET, 15: Hitachi PCTW-II, 16: TTV-03 (LETI),
17: Headtome III, 18: NIRS Animal PET, 19: ECAT III, 20: Headtome IV, 21: Donner 600,
22: Scanditronix PC-2048, 23: CTI 931/953,
24: Hamamatsu SHR-1200: Developed by the author et al.
25: Hamamatsu SHR-2000 : PET using PS-PMT detector developed by the author et al.

Fig.1-16 Evolution of spatial resolution of PET during the last fifteen years (Resolution of a PET using the PS-PMT detector is indicated by an arrow in the figure)

1.6 Scope of the Dissertation

Designing and building a high intrinsic resolution detector for PET is the primary concern of this study. As this is the first effort in building a PET detector system composed of a position-sensitive PMT, we have investigated and discovered many interesting characteristics of the detector and a PET system using it.

Chapter 2 describes the results of fundamental studies on the PET detectors which include optimal design of BGO scintillators, development of techniques to quantitatively evaluate the detector performance and analysis of the detector characteristics.

In Chapter 3 the basic design of a new detector using a PS-PMT is described. Resolution limits of the detector are also discussed in this chapter. Position calculation for the PS-PMT is analyzed and it is shown that the scintillation light spread on the photocathode is a primary factor affecting the intrinsic resolution of the PS-PMT detector. A new BGO block detector is presented, which was developed for a practical use in a PET system.

A PET system dedicated to animal studies has been developed using the new PS-PMT, and a spatial resolution of 3.0 mm has been achieved. The design and the construction of the PET system is described in Chapter 4. The physical performance of the system and the results of PET experiments with animals are also shown in this chapter.

In Chapters 5 and 6, new detectors detecting depth-of-interaction of γ-rays are discussed. This work has been motivated by a need for uniform resolution over the entire field of view. The detectors proposed here are variations from the original design of the detector using PS-PMT. The effectiveness of the depth-of-interaction detection was evaluated by measuring the coincidence response function for different incident angles of γ-rays.

Finally, in Chapter 7, we summarize the results and offer some possible directions for future work, where discussions on detectors for 3D-PET and clinical PET are included.

References

(1) S. De Benedetti, C.E. Cowan, W.R. Konneker et al., "On the angular distribution of two-photon annihilation radiation," *Phys. Rev.*, vol.77, pp.205-212, 1950

(2) Z.H. Cho, J.K. Chan, L. Eriksson et al., "Positron range obtained from biomedically important positron emitting radionuclides," *J. Nucl. Med.*, vol.16, pp.1174-1176, 1975

(3) S.E. Derenzo, "Mathematical removal of positron range blurring in high resolution tomography," *IEEE Trans. Nucl. Sci.*, vol.33, pp.565-569, 1986

(4) N.M. Alpert, D.A. Chesler, J.A. Correia et al., "Estimation of the local statistical noise in emission computed tomography," *IEEE Trans. Med. Imag.*, vol.1, pp.142-146, 1982

(5) G. Muhllehner, "Effect of resolution improvement on required count density in ECT imaging - A computer simulation," *Phys. Med. Biol.*, vol.30, pp.163-173, 1985

(6) E. Tanaka and H. Murayama, "Properties of statistical noise in positron emission tomography," In *Proceedings of International Workshop on Physics and Engineering in Medical Imaging, IEEE Comput. Soc.* 82CH1751-7, pp.158-164, Pacific Grove, 1982

(7) E.R. Wrenn, M.L. Good and P. Handler, "The use of positron emitting radioisotopes for the localization of brain tumors," *Science*, vol.113, pp.525-527, 1951

(8) W.H. Sweet, "Uses of nuclear disintegrations in the diagnosis and treatment of brain tumors," *N. Engl. J. Med.*, vol.245, p.875, 1951

(9) G.L. Brownell and W.H. Sweet, "Localization of brain tumors with positron emitters," *Nucleonics*, vol.11, p.40, 1953

(10) H.O. Anger and D.J. Rosenthal, "Scintillation camera and positron camera," *Medical Radioisotope Scanning*, pp.59-68, 1959

(11) S. Rankowitz, J.S. Robertson, W.A. Higinbotham et al., "Positron scanner for locating brain tumors," *IRE Int. Conv. Rec.*, vol.9, pp.49-56, 1962

(12) M.E. Phelps, E.J. Hoffman, N.A. Mullani et al., "Application of annihilation coincidence detection to transaxial reconstruction tomography," *J. Nucl. Med.*, vol.16, pp.210-223, 1975

(13) M.M. Ter-Pogossian, M.E. Phelps, E.J. Hoffman et al., "A positron emission transaxial tomograph for nuclear medicine imaging (PETT)," *Radiology*, vol.114, pp.89-98, 1975

(14) M.E. Phelps, E.J. Hoffman, N.A. Mullani et al., "Design considerations for a positron emission transaxial tomograph (PETT III)," *IEEE Trans. Nucl. Sci.*, vol.23, pp.516-522, 1976

(15) Z.H. Cho, J.K. Chan and L. Eriksson, "Circular ring transverse axial positron camera for 3-dimensional reconstruction of radionuclide distribution," *IEEE Trans. Nucl. Sci.*, vol.23, pp.613-622, 1976

(16) Y.L. Yamamoto, C.J. Thompson, E. Meyer et al., "Dynamic emission tomography for study of cerebral hemodynamics in cross section of the head using positron emitting ^{68}Ga-EDTA and ^{77}Kr," *J. Comput. Assist. Tomogr.*, vol.1, pp.43-56, 1977

(17) C. Bohm, L. Eriksson, M. Bergstrom et al., "A computer assisted ring detector positron camera system for reconstruction tomography of the brain," *IEEE Trans. Nucl. Sci.*, vol.25, pp.624-637, 1978

(18) S.E. Derenzo, T.F. Budinger, J.L. Cahoon et al., "The Donner 280 crystal high resolution positron tomograph," *IEEE Trans. Nucl. Sci.*, vol.26, pp.2790-2793, 1979

(19) C.J. Thompson, Y.L. Yamamoto and E. Meyer, "Positome II: A high efficiency positron imaging system for dynamic brain studies," *IEEE Trans. Nucl. Sci.*, vol.26, pp.582-589, 1979

(20) Z.H. Cho and M.R. Farukhih, "Bismuth germanate as a potential scintillation detector in positron cameras," *J. Nucl. Med.*, vol.18, pp.840-844, 1977

(21) G.L. Brownell, C.A. Burnham, D.A. Chesler et al., "Transverse section imaging of radionuclide distribution in heart, lung and brain," In *Reconstruction Tomography in Diagnostic Radiology and Nuclear Medicine*, University Park Press, Boston, pp.293-306, 1977

(22) G. Muhllehner, M.P. Buschin, and J.H. Dudek, "Performance parameters of positron imaging camera," *IEEE Trans. Nucl. Sci.*, vol.23, pp.528-537, 1976

(23) M.M. Ter-Pogossian, N.A. Mullani, J.T. Hood et al., "A multislice positron emission computed tomograph (PETT IV) yielding transverse and longitudinal images," *Radiology*, vol.128, pp.477-484, 1978

(24) M.M. Ter-Pogossian, N.A. Mullani and J.T. Hood, "Design considerations for a positron emission transverse tomograph (PETT V) for imaging of the brain," *J. Comput. Assist. Tomogr.*, vol.2, pp.539-544, 1978

(25) M.E. Phelps, E.J. Hoffman, S.C. Huang et al., "The NeuroECAT: A new high resolution multiplane positron computed tomograph for imaging the brain," *J. Nucl. Med.*, vol.22, p.38, 1981

(26) M.M. Ter-Pogossian, N.A. Mullani, D.C. Ficke, "Photon time-of-flight-assisted positron emission tomography," *J. Comput. Assist. Tomogr.*, vol.5, pp.227-239, 1981

(27) R. Allemand, P. Gresset and J. Bacher, "Potential advantages of a cerium fluoride scintillator for a time-of-flight positron camera," *J. Nucl. Med.*, vol.21, pp.153-155, 1980

(28) R.A. Brooks, V.M. Sank, G. DiChiro et al., "Design of high resolution positron emission tomograph: The neuro-PET," *J. Comput. Assist. Tomogr.*, vol.4, pp.5-13, 1980

(29) L. Carroll, "Design and performance characteristics of a production model positron imaging system," *IEEE Trans. Nucl. Sci.*, vol.25, pp.606-614, 1979

(30) N. Nohara, E. Tanaka, T. Tomitani et al., "Positologica: A positron ECT device with a continuously rotating detector ring," *IEEE Trans. Nucl. Sci.*, vol.27, pp.1128-1136, 1980

(31) L. Eriksson, C. Bohm, M. Kesselberg et al., "A four ring positron camera for emission tomography of the brain," *IEEE Trans. Nucl. Sci.*, vol.29, pp.539-543, 1982

(32) I. Kanno, K. Uemura, S. Miura et al., "Headtome: A hybrid emission tomograph for single photon and positron emission imaging of the brain," *J. Comput. Assist. Tomogr.*, vol.5, pp.216-226, 1981

(33) G. Muhllehner and J.G. Colsher, "Use of position sensitive detectors in positron imaging," *IEEE Trans. Nucl. Sci.*, vol.27, pp.569-571, 1980

(34) S.E. Derenzo, R.H Huesman, J.L. Cahoon et al., "Initial Results from the Donner 600 crystal positron tomograph," *IEEE Trans. Nucl. Sci.*, vol.34, pp.321-325, 1987

(35) T. Yamashita, H. Uchida, H. Okada et al., "Development of a high resolution PET," *IEEE Trans. Nucl. Sci.*, vol.37, pp.594-599, 1990

(36) H. Murayama, N. Nohara, E. Tanaka et al., "A quad BGO detector and its timing and position discrimination for positron computed tomography," *Nucl. Instr. Meth.*, vol.192, pp.501-511, 1982

(37) C. Burnham, J. Bradshaw, D. Kaufman et al., "Application of a one dimensional scintillation camera in a positron tomographic ring detector," *IEEE Trans. Nucl. Sci.*, vol.29, pp.461-468, 1982

(38) M.E. Casey and R. Nutt, "A multicrystal two dimensional BGO detector system for positron emission tomography," *IEEE Trans. Nucl. Sci.*, vol.33, pp.460-463, 1986

(39) T. Yamashita, M. Itoh and T. Hayashi, "New dual rectangular photomultiplier tube," In *Proceedings of International Workshop on Physics and Engineering in Medical Imaging, IEEE Comput. Soc.* 82CH1751-7, pp.209-211, Pacific Grove, 1982

(40) J.M. Roney and C.J. Thompson, "Detector identification with four BGO crystals on a dual PMT," *IEEE Trans. Nucl. Sci.*, vol.31, pp.1022-1027, 1984

(41) S. Yamamoto, S. Miura, S. Iida et al., "A BGO detector unit for a stationary high resolution positron emission tomography," *J. Comput. Assist. Tomogr.*, vol.10, pp.851-855, 1986

(42) L. Eriksson, C. Bohm, M. Kesselberg et al., "Design studies of two possible detector blocks for high resolution positron emission tomography of the brain," *IEEE Trans. Nucl. Sci.*, vol.34, pp.344-348, 1987

(43) H.B. Min, J.B. Ra, K.J. Jung, et al., "Detector identification in a 4x4 BGO crystal array coupled to two dual PMTs for high resolution positron emission tomography," *IEEE Trans. Nucl. Sci.*, vol.34, pp.332-336, 1987

(44) L. Eriksson, C. Bohm, M. Kesselberg et al., "A high resolution positron camera," In *Proceedings of VII Nobel Conference on The metabolism of the human brain studied with positron emission tomography,* Stockholm, 1983 (In Raven Press, New York, pp.33-46, 1985)

(45) H. Murayama, E. Tanaka, N. Nohara et al., "Twin BGO detectors for high resolution positron emission tomography," *Nucl. Instr. Meth.*, vol.221, pp.633-640, 1984

(46) S.E. Derenzo, W.W. Moses, H.G. Jackson et al., "Initial characterization of a BGO-photodiode detector for high resolution positron emission tomography," *IEEE Trans. Nucl. Sci.*, vol.36, pp.1084-1089, 1989

(47) A.W. Lightstone, R.J. McIntyre, R. Lecomte et al., "A bismuth germanate - avalanche photodiode module designed for use in high resolution positron emission tomography," *IEEE Trans. Nucl. Sci.*, vol.33, pp.457-459, 1986

(48) J.E. Bateman, JJ.F. Connolly, R.Stephenson et al., "The development of MWPC-based systems for imaging X-rays and charged particles in application in medicine, material science and biochemistry" *Nucl. Instr. Meth.*, vol.217, pp.77-88, 1983

(49) P. Mine, J.C. Santiard, D. Scigocki et al., "Test of a BaF_2-TMAE detector for positron-emission tomography," *IEEE Trans. Nul. Sci.*, vol.34, pp.458-460, 1987

(50) H. Kume, S. Suzuki, J. Takeuchi et al., "Newly developed photomultiplier tubes with position sensitive capability," *IEEE Trans. Nucl. Sci.*, vol.32, pp.448-452, 1985

(51) H. Uchida, T. Yamashita, M. Iida et al., "Design of a mosaic BGO detector system for positron CT," *IEEE Trans. Nucl. Sci.*, vol.33, pp.464-467, 1986

Chapter 2

Study of Detector Design for PET

This chapter describes fundamental characteristics of scintillation detectors for PET. PET detectors are specifically required to have good temporal and spatial resolution, while most characteristics required for them are common to those with other radiation detectors.

In Section 2.1, optical and geometrical design of scintillators to obtain better detector characteristics is demonstrated. Section 2.2 presents methods for valid evaluation of the detectors which are essential for the improvement or the development of new detectors. We have constructed instrument to measure the performance of PET detectors developed in the last fifteen years, some of which were developed on the basis of the previous work. Section 2.3 shows the analysis of the time resolution with a BGO detector.

2.1 Optical and Geometrical Design

2.1.1 Characteristics Matching between Scintillator and PMT

BGO ($Bi_4Ge_3O_{12}$), BaF_2, CsF and NaI(Tl) scintillators have been used in PET systems because of their high stopping power for 511 keV γ-rays and short scintillation decay time [1][2]. Various types of PMTs have been coupled to scintillators in different manners. In any detector scheme, the matching characteristics between the scintillator and the PMT are of prime importance. Figure 2-1 shows the emission spectra of BGO, NaI(Tl) and BaF_2, which are used in current PET systems.

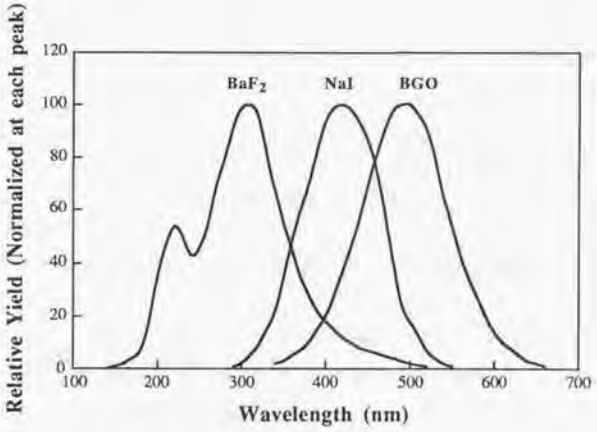

Fig.2-1 Emission spectra of scintillators used in PET

The emission spectra of the scintillators have their emission peaks in the wavelength region below 500 nm, so that bialkali photocathode can provide the highest conversion efficiency from scintillation photons to photoelectrons among numerous photocathode materials [3]. Since BGO has the highest stopping power among the scintillators, most current PET systems use BGO in order to obtain both high spatial resolution and high sensitivity. An ideal bialkali photocathode has a quantum efficiency over 20% at the BGO emission peak of

480 nm as shown in Fig.2-2. As a good quality of BGO scintillator has an energy conversion efficiency of approximately 1.5% (from 511 keV γ-rays to visible photons), the number of photoelectrons emitted from the photocathode is calculated to be 400 – 500 in one event.

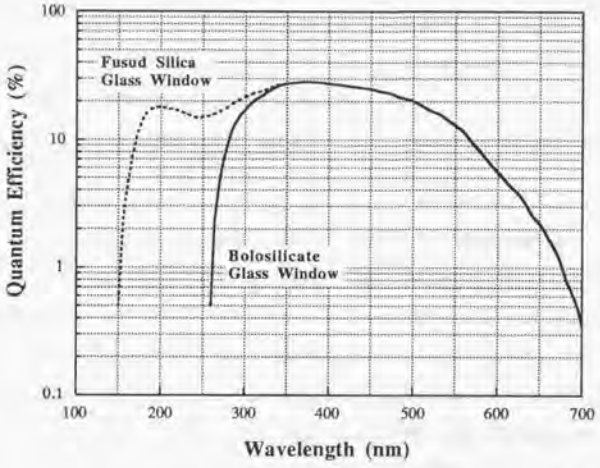

Fig.2-2 Spectral quantum efficiency of bialkali photocathode

In a practical use, however, there are two dominant factors that reduce the conversion efficiency from γ-rays to PMT current signals: one is the loss of scintillation photons through the light propagation process from the scintillation point to the photocathode, and the other is the photoelectron collection efficiency of the first dynode in a PMT. The former factor largely depends on the optical and geometrical design of the scintillator and the PMT, which includes surface smoothness, transparency (self-absorption in a scintillator), reflectance of the reflector, scintillator shape, properties of the optical coupling compound between the scintillator and the PMT, refractive indices of the PMT glass window and the photocathode, and the PMT window geometry (its shape and thickness). The latter factor is determined by the design of electron optics in a PMT which largely depends on the PMT shape (cylindrical or rectangular) and the dynode structure. The net efficiency including both the photocathode quantum efficiency and the photoelectron collection efficiency is called effective quantum efficiency.

The effective photoelectron number in one event is estimated to be 200–300 for 511 keV γ-rays with a small diameter PMT coupled to a BGO.

Very fast timing properties are not required for PMTs coupled to BGO crystals, while they are of prime importance for a PMT using with fast scintillators such as BaF_2 or CsF. Since BGO has a relatively slow scintillation decay time and poor light output, the dominant factor affecting the time resolution is the number of effective photoelectrons in one event. The time resolution for BGO photons is discussed in Section 2.3.

2.1.2 Light Output from BGO Scintillators

Crystal growth technology with BGO has greatly advanced since BGO's scintillation properties were discovered by Weber and Monchamp in 1973 [4]. At present light output from the best quality BGO crystal reaches 20 % of NaI(Tl). The attenuation length of BGO photons (mean free path) is larger than 100 cm, so that the efficiency loss due to self-absorption in the crystal is negligible [5]. The dominant factor affecting the BGO light output is absorption by a reflector material. As the number of reflections on a reflector increases in a BGO crystal, the light output from the crystal decreases. Especially, in a slender BGO having a smaller cross section area and a longer depth, the light output becomes smaller because of an increasing number of reflections on the reflector walls.

The dependence of light output on the crystal surface condition was studied with slender BGO crystals, where each BGO specimen has a 3 mm x 3 mm cross-section area and a 15 mm depth. The experimental results are shown in Fig.2-3. BGO crystals having five mirror-polished surfaces and one coarsely ground (#1000) surface on the top provide the highest light output. Since the refractive index of BGO is 2.15, the critical angle for total reflection is 28° at the air boundary and 44° at the boundary to a PMT window. If the all surface planes of a BGO crystal are mirror-polished, a large fraction of scintillation photons are trapped in the BGO. On the other hand, if they are all coarsely ground, the number of reflections on the reflector material increases, and consequently the light output decreases due to the reflection loss.

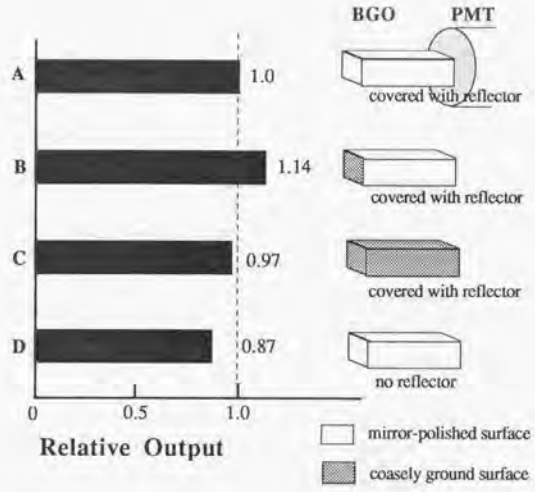

Fig.2-3 BGO light output dependence on the surface condition

We carried out a simulation study of the light output from BGO crystals having different areas of square cross-section and different depths using the Monte Carlo method [6]. In the simulation, all BGO crystals have five mirror-polished surfaces and one coarsely ground surface on the top. The calculation was performed on the following hypotheses:

(1) All photons in one event are emitted simultaneously from a given point in a BGO, into random directions.

(2) When a photon reaches the BGO surface, it undergoes the Fresnel law with both reflection and refraction. If a photon strikes the diffused reflector, the distribution of reflection angles is given by the Lambert law.

(3) The calculation for one history is stopped, if the number of reflections exceeds a given maximum value.

(4) The light attenuation is caused only by two factors; absorption in the BGO and reflection loss at the diffused reflector.

In this calculation, we assumed that the optical attenuation length in a BGO was 200 cm and the reflectivity on the diffused reflector was 98 %. The maximum number of reflections were set to 100. Figure 2-4 summarizes the results of the calculation. As shown in the figure, a BGO crystal having a smaller cross-sectional area and a longer depth loses more scintillation photons before their escape from the crystal.

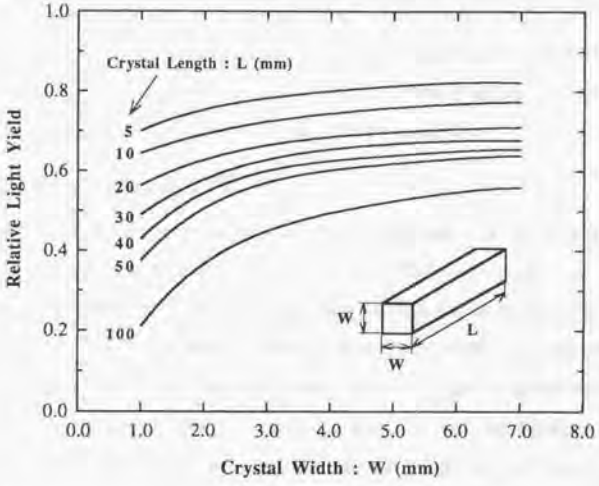

Fig.2-4 Light output dependence on the length and width of BGO crystals (Simulation study by the Monte Carlo calculation)

There are many reflector materials for BGO such as $BaSO_4$, TiO_2, Al_2O_3 and MgO. It is reported that the primary factor affecting reflection efficiency is the particle size of the reflector material, not the material itself [7]. The other important factor for better light output is the existence of thin air gaps between the crystal and the reflector, because the total reflection at the crystal-air boundary causes no optical loss and the probability of the total reflection is large with a high refractive index of BGO. The powder materials are usually retained to a BGO wall with adhesive materials (binder) which generally degrades the reflection efficiency. Thus there is a trade-off between the mechanical strength of the powder

reflector on a crystal and the reflection efficiency. By contrast with the powder materials, Teflon (polytetrafluoroethylene) is a convenient reflector material for a practical use, because it has reasonably good reflection efficiency, and a crystal can be easily lapped using thin Teflon sheets having uniform thickness.

2.2 Evaluation of PET Detector Characteristics

An accurate evaluation of detector characteristics is necessary for the design and development of PET detectors. We have constructed various apparatus to measure the detector characteristics; PMT transit time spread, scintillation decay time, coincidence time resolution, PMT count rate performance, and detector intrinsic spatial resolution.

2.2.1 Transit Time Spread (TTS)

Transit time spread (TTS) is one of the most important measures for evaluation of the timing properties of a PMT. For a given illuminated area on a PMT photocathode, the arrival time of electron pulses at the anode fluctuates event by event. TTS is characterized by a probability density function of the transit time from the photocathode to the anode, when the photocathode is illuminated with very weak light pulses providing only a single photoelectron per pulse. The measurement apparatus we built is shown in Fig.2-5. Fast light pulses of 800 nm wavelength are emitted from a laser diode, and converted to pulses having 400 nm wavelength through a nonlinear crystal, called second harmonic generator (SHG). They are irradiated onto the full cathode area of a PMT after passing through several filters, a filter removing 800 nm light and neutral density (ND) filters attenuating the intensity of light pulses down to a single photon level.

2.2.2 Scintillation Decay Time

Scintillation decay time is measured using the delayed-coincidence method of Bollinger and Thomas, as modified by Moszynski and Bengtson [8][9]. Figure 2-6 shows an apparatus for the scintillation decay time measurement. A BaF_2 or a plastic scintillator detector is used for a reference probe and the timing signal through a constant fraction discriminator (CFD) is led into a time-to-amplitude converter (TAC) as the stop timing trigger. Scintillation light from a scintillator specimen is detected by a fast PMT having a small aperture on the photocathode,

and the output signal through a CFD is used as the start timing trigger into the TAC. The timing accuracy of the measuring system is 200 ps - 300 ps which primarily depends on the timing properties (mainly TTS) of the start channel PMT. Since 511 keV γ-rays may cause scintillation or Cherenkov radiation in the glass window of a monitor PMT (in the start channel), a lead shield is placed between a positron source and the PMT.

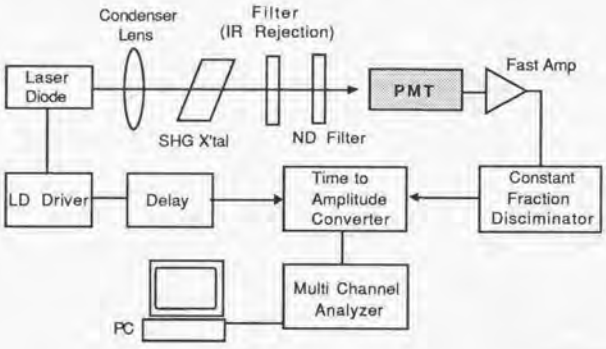

Fig.2-5 Measurement apparatus of transit time spread (TTS)

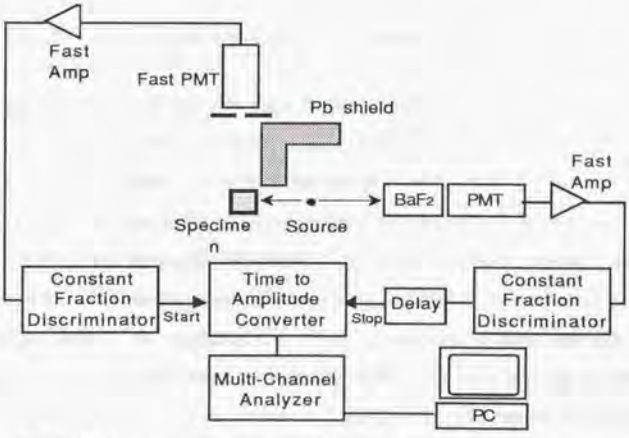

Fig.2-6 Measurement apparatus of scintillation decay time

2.2.3 Coincidence Time Resolution

Figure 2-7 shows measurement apparatus for coincidence time resolution, which uses a fast-slow coincidence technique. For slow scintillators such as BGO, the energy discrimination is performed with pulses integrated for a period long enough compared to the decay time in order to attain a good statistical accuracy.

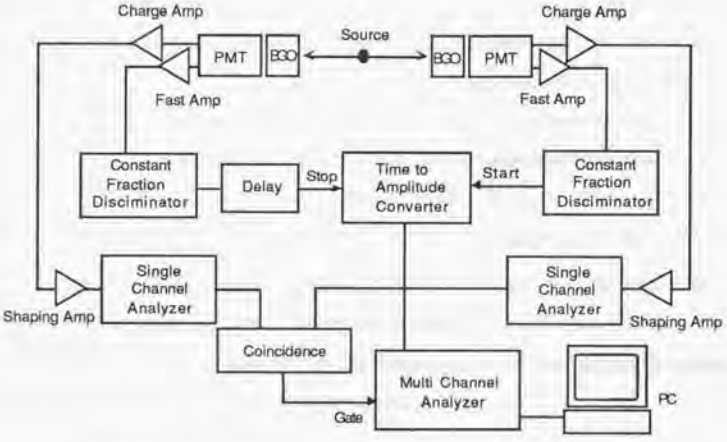

Fig.2-7 Measurement apparatus of coincidence time resolution

In the measurement setup shown in Fig.2-7, the last dynode signal and the anode signal are independently taken out, where the positive signal from the last dynode is used for energy discrimination, and the negative signal from the anode is used for timing pick-off. Anode pulses are amplified through fast current amplifiers and introduced to constant fraction discriminators (CFD). The timing discrimination is performed at a single photoelectron level. In our experiments, ARC timing method (amplitude and rise time compensated timing method) provided better time resolution than TCR timing method (true constant fraction timing method). To apply ARC timing method, we set the delay time between the fractional inverted signals and the delayed input signals at 1 ns or less. The reason for the superior timing with the ARC timing method, may be explained by the fact that the rising part of BGO

pulse is composed of piled-up single photoelectron events and thus the rise time may fluctuate event by event because of the poor photon statistics.

2.2.4 Count Rate Dependence of PMT and Voltage Divider

Electron pulses in a PMT are gradually amplified through a multiple secondary electron emission process at cascade dynodes. The current level of signals increases exponentially towards the later stages of the dynodes. The signal current flows through resistors of a voltage divider in the opposite direction against the feeder current. Thus it may cause a voltage drop at the later dynodes, when the PMT is illuminated with high count-rate light pulses. Since the total applied voltage to the voltage divider is always kept constant by an external voltage power supply, the voltage drop at the later stages of dynodes is redistributed towards the photocathode, and consequently the electron multiplier gain increases. In order to operate a PMT at a constant gain, the anode current should be kept at a level below 2% - 5% of the feeder current. The count rate capability is measured using the apparatus shown in Fig.2-8.

Although large feeder current improves the count rate capability, it results in large power dissipation through the resistor chain. As the signal current level is large only at the later stage of dynodes, especially at the anode and the last dynode, the count rate capability is improved by using a separate power supply for the later dynodes.

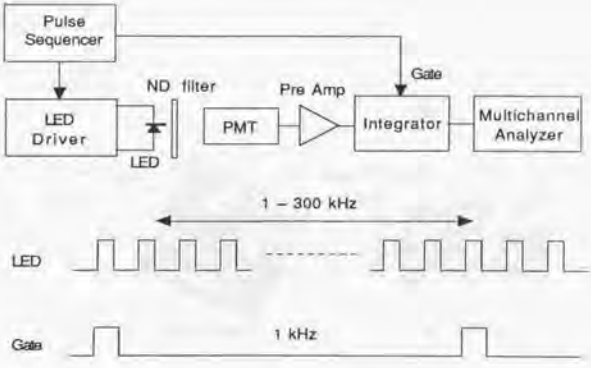

Fig.2-8 Measurement apparatus of count rate performance

2.2.5 Intrinsic Spatial Resolution of PET Detector

The spatial resolution of a PET detector can be evaluated by the coincidence response function (CRF) as described in Section 1.3. However, the CRF measured with an opposed detector pair in coincidence includes other physical factors, positron range and angular deviation, besides the detector intrinsic resolution. We can evaluate the detector intrinsic resolution by the following procedure.

First, a single detector response function (DRF) is measured as a response to a sweeping collimated source maintaining the incident angle constant as shown in Fig.2-9. The CRF is then calculated from the single DRF by taking the product of the differential efficiency curves for coincidence between two opposing detectors. For the intrinsic DRF of $g(X)$, Lecomte et al. induced the CRF $f(X,\varepsilon)$ as follows [10] :

$$f(X,\varepsilon)=\int_0^{X_0} g(x)g\{X+\varepsilon\,(X-x)\}dx, \qquad (2\text{-}2\text{-}5)$$

where $\varepsilon=r_1/r_2\ (r_2>r_1)$ is the eccentricity in the position of the source relative to the coincidence detectors, and X_0 is the effective channel width defined by the projection of the detector active volumes at the considered incidence angle (refer Fig.2-11). For a source located halfway between the detectors ($\varepsilon=1$), the CRF takes on a value equivalent to the auto-convolution of the DRF.

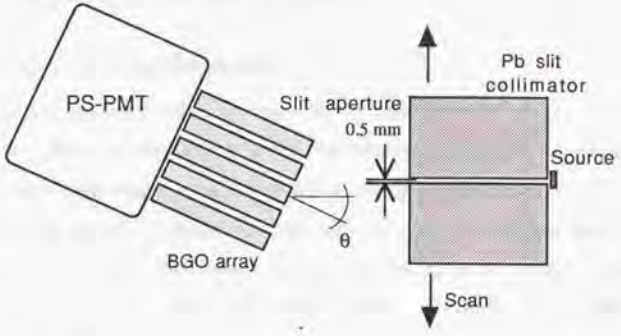

Fig.2-9 Measurement apparatus of detector response function (DRF)

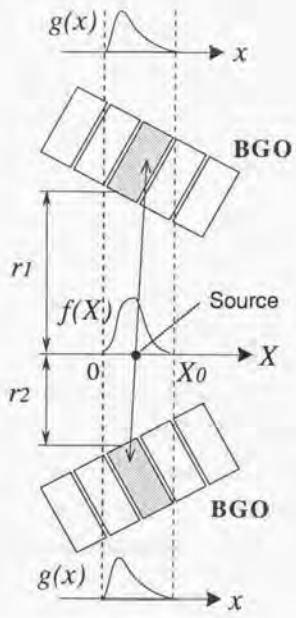

Fig.2-10 Geometrical Parameters for calculation of coincidence response function

2.3 Time Resolution of BGO Detectors

2.3.1 Calculation of Time Resolution

For a slow and low light yield scintillator such as BGO, the best time resolution is obtained when the anode signal corresponding to the first photoelectron arriving at the first dynode is used as a timing pick-off trigger. The variance in its arrival time is then given by $(\tau / N_e)^2$ as reported by Post and Schiff [11], where N_e is the mean value of photoelectron number in one event and τ is a scintillation decay constant. In the condition above, it is assumed that a PMT is illuminated by a single exponential light pulse and also that the PMT has no TTS. In an actual case, however, the illumination function has a finite rise time due to the transit time

jitter of the scintillation photons in a scintillator, and a PMT has transit time fluctuation (TTS). In consideration of these factors, we analyzed the time resolution for a given geometry of a BGO detector [12].

We assume that the time resolution of a BGO detector (σ) is given by the following equation:

$$\sigma^2 = \sigma_{sc}^2 + \sigma_{pm}^2 , \qquad (2\text{-}3\text{-}1)$$

where σ_{sc}, and σ_{pm} are the standard deviations of the time jitter for a scintillator and a PMT, respectively.

The photon transit time distribution from BGO can be calculated using the Monte Carlo method described in Section 2.1.2. Figure 2-11 shows an example of the photon transit time distribution calculated for a 12 mm wide x 24 mm high x 24 mm deep BGO, where a PMT is fully coupled to a 12 x 24 mm^2 plane of the BGO. The BGO has five coarsely-ground planes and one mirror-polished plane contacting with the PMT.

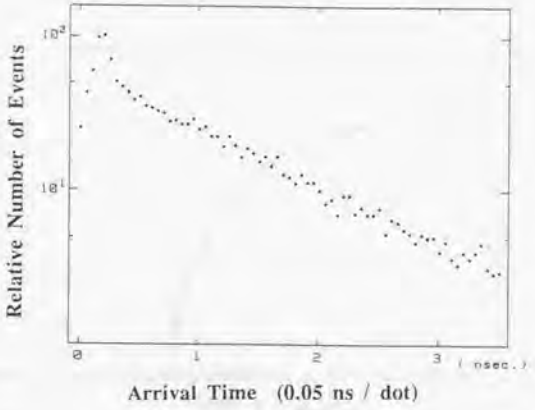

Fig.2-11 Photon transit time distribution calculated by the Monte Carlo method (BGO has five coasely-ground planes and one mirror-polished plane contacting with PMT)

As shown in the figure, the distribution has fast and slow transit components. The fast component is due to the photons which reach the output plane directly or after a few reflections, while the slow component is due to the multiple reflections in the BGO.

The illumination function (light input on a PMT) $H(t)$ is described by the convolution between a BGO scintillation decay function $G(t)$ and the photon transit time distribution $I(t)$ as follows:

$$H(t) = I(t) \otimes G(t). \tag{2-3-2}$$

We measured the BGO intrinsic decay function for the 12 x 24 x 24 mm^3 BGO by adopting the measurement technique described in Section 2.2.2, where we used a microchannel-plate (MCP) PMT in the start channel and a plastic scintillator in the stop channel. The timing accuracy of the system was about 300 ps. BGO has two decay components as reported by Moszynski et al [13]. The measured decay time constants were about 60 ns (including 10% of the total photons) and 300 ns (90% photons), which agreed with the values obtained by Moszynski et al. The illumination function obtained by calculation using eq.2-3-2 is shown in Fig.2-12.

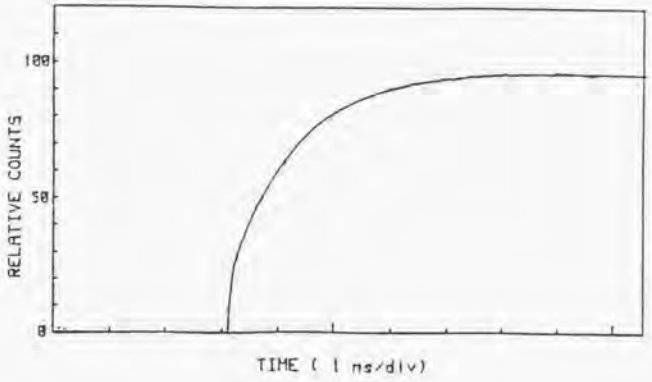

Fig.2-11 Illuminating function calculated for a BGO having five coasely-ground planes and one mirror-polished plane contacting with PMT.

The probability $P(T)$ that the first photoelectron arrives at the first dynode within a small interval of ΔT between the time T and $T+\Delta T$ is obtained using Poisson statistics as follows:

$$P(T)\Delta T = \exp\left\{-N_e\int_0^T H(t)dt\right\}\left[1-\exp\left\{-N_e H(T)\Delta T\right\}\right], \qquad (2\text{-}3\text{-}3)$$

where N_e is the number of photoelectrons in one event.

We measured the pulse height for single photoelectron events and compared it to the pulse height for 511 keV γ-rays. The ratio of 320 was obtained, i.e. N_e=320. The BGO coincidence timing spectrum is then given by the auto-convolution of $P(T)$. Figures 2-13 (a) and (b) show the calculated and measured coincidence timing spectra, respectively. In the measurement, dual PMTs having two 12 x 24 mm^2 segments (Hamamatsu R1548) were used with fully coupled to the BGO crystals. The values of FWHM of the distributions are 2.22 ns and 2.9 ns for the calculated and measured spectra. The discrepancy between the calculation and the measurement can be explained by the fact that the effect of PMT transit time spread (TTS) is included in the measurement data, but not accounted for in the calculation. Inaccuracy in the estimation of N_e, associated with the pulse height measurement for single photoelectron events, might be also introduced in the calculation of the coincidence timing spectra.

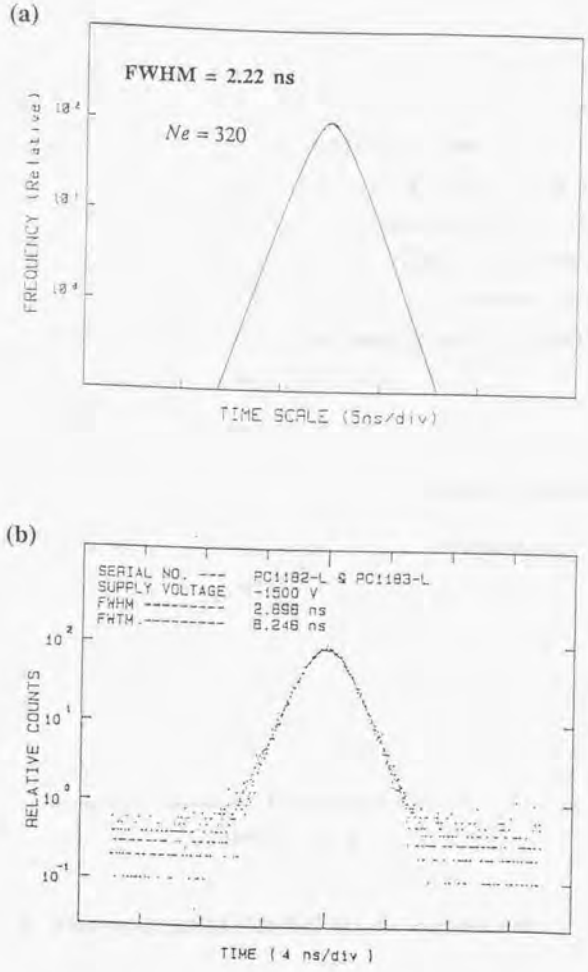

Fig.2-13 Coincidence timing spectra obtained by calculation (top) and by measurement (bottom).

2.3.2 Illumination Functions from BGO Crystals with Different Conditions

We assume that a 13 mm diameter PMT (e.g. Hamamatsu R647) is coupled to the BGO (12 x 24 mm^2 cross section by 24 mm depth) at a 12 mm x 24 mm plane, where the PMT is partially coupled to the BGO. All surface areas on the BGO except the area optically coupled to the PMT is covered with a $BaSO_4$ reflector. The BGO has five coarsely-ground planes and one mirror-polished plane contacting with the PMT. We calculated the transit time distribution of the scintillation photons and the illumination function. Figure 2-14 shows the rising part of the illumination function obtained by the calculation. It is found that the rise time of illumination function is slow with a BGO crystal partially coupled to a PMT (Fig.2-14), compared to that with a BGO fully coupled to a PMT (Fig.2-12).

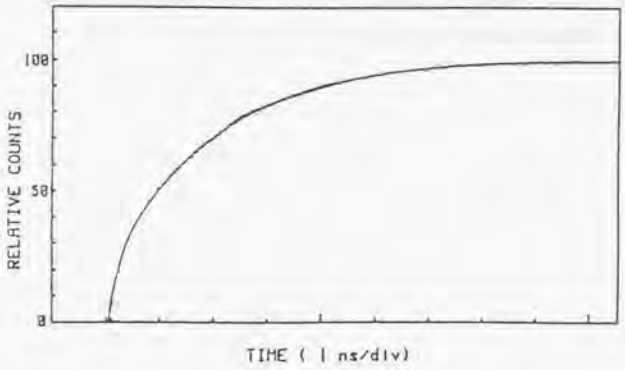

Fig.2-14 Illumination function from BGO partially coupled to PMT.

We also calculated the photon transit time distribution and the illumination function with a BGO crystal having a different optical condition. The calculation was performed with a BGO (12 x 24 x 24 mm^3) having five mirror-polished planes and one coarsely ground plane on the top which was fully coupled to a PMT. The results are shown in Figures 2-15 and 2-16.

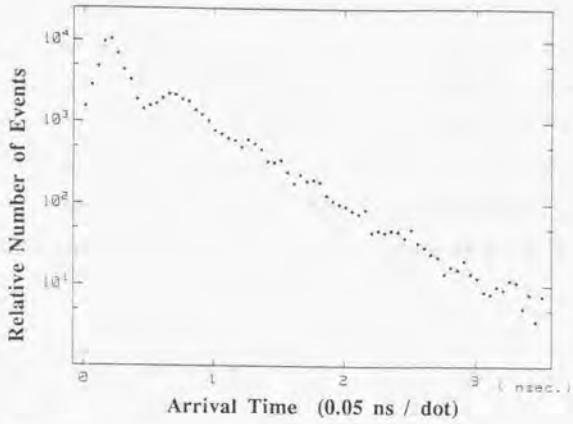

Fig.2-15 Photon transit time distribution calculated for a BGO having five mirror-polished surface palnes and one coasely ground plane on the top.

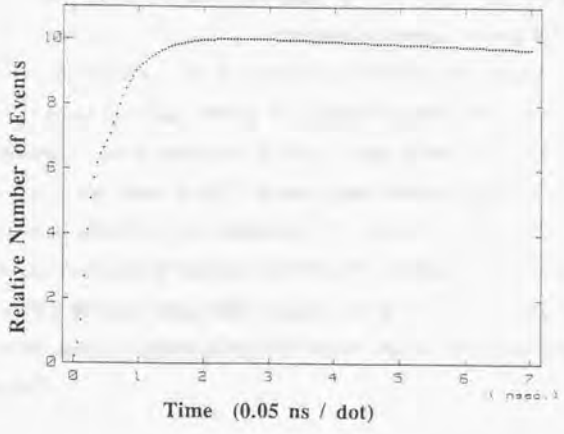

Fig.2-16 Illumination function calculated for a BGO having five mirror-polished surface planes and one coasely ground plane on the top.

Figure 2-15 shows the photon transit time distribution of the BGO. As shown in the figure, two peaks corresponding to fast transit components are clearly seen, which are followed by a slow exponential transit component. The first peak corresponds to scintillation photons which directly reach the PMT, and the second peak corresponds to photons which are once reflected at the BGO-PMT interface and reach the PMT after a reflection at the top surface plane. Figure 2-16 shows the rising portion of the illumination function from the BGO, which has a sharp rising part followed by a relatively slow rising part.

We assume the following empirical function to approximate the shape of the rising portion of the illumination function,

$$I(t) \equiv k\left\{1-\exp(-t/\tau_r)\right\}, \qquad (2\text{-}3\text{-}5)$$

where k is a function of the photon transit time distribution and scintillation decay time but not of time t, and τ_r is a time constant of the rising part. Although the function above is not a good approximation for the illumination function of a BGO having a large fraction of fast photon transit components shown in Fig.2-16, it helps our intuitive understandings how the illumination function affects the time resolution of BGO detectors. We calculated the coincidence time resolution corresponding to illumination functions having different rise time. Figure 2-17 shows the calculation result, where the FWHM values of the coincidence time resolution of BGO detectors having different illumination functions are shown as a function of the number of photoelectrons in one event. If we use a high quality BGO crystal (12 x 24 x 24 mm^3) coupled to a 50 mm diameter PMT having a good effective quantum efficiency and a good TTS (e.g. Hamamatsu R329), the values of $t_r < 1$ ns and $N_e \equiv 400$ are obtained, and thus the coincidence time resolution of less than 2 ns FWHM is obtained. This is a goal of the time resolution of a PET detector using BGO, where it is important to design a detector in consideration of the optical condition of the BGO crystal and the shape matching between the crystal and the PMT.

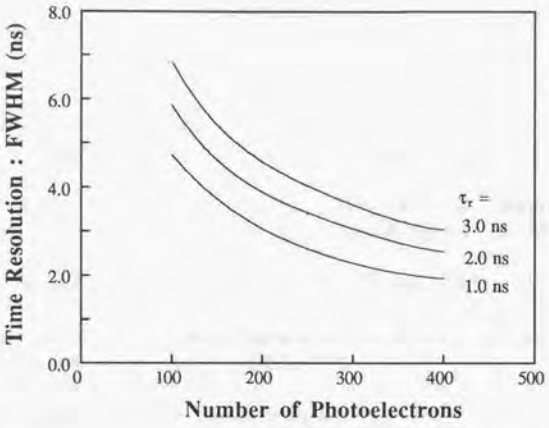

Fig.2-17 Coincidence time resolution for illumination functions having different rise time as a function of the number of photoelectrons in one event

References

(1) M.R. Farukhi, "Recent developments in scintillation detectors for X-ray CT and positron CT applications," *IEEE Trans. Nucl. Sci.*, vol.29, pp.1237-1248, 1982

(2) M. Laval, M. Moszynski, R. Allemand et al, "Barium Fluoride - Inorganic scintillator for subnanosecond timing," *Nucl. Instr. Meth.*, vol.206, pp.169-176, 1983.

(3) *Hamamatsu Photonics Catalog*, "Photomultiplier Tubes" (1993)

(4) M.J. Weber and R.R. Monchamp, "Luminescence of Bi4Ge3O12: spectral and decay properties," *J. Appl. Phys.*, vol.44, p.5496-, 1973

(5) *Crismatec Catalog*, "Bismuth germanate crystals"

(6) H. Uchida, T. Yamashita, M. Iida et al., "Design of a mosaic BGO detector for positron CT," *IEEE Trans. Nucl. Sci.*, vol.33, pp.889-893, 1986

(7) T. Ryuo, S. Makihara and T. Mori, "Radiation Detector," *U.S.A. Patent*, No.5061855

(8) L.M. Bolinger and G.E. Thomas, "Measurement of the time dependence of scintillation intensity by a delayed coincidence method," *Rev. Sci. Instr.*, vol.32, pp.1044-1050, 1961

(9) M. Moszynski and B. Bengtson, "Light pulse shapes from plastic scintillators," *Nucl. Instr. Meth.*, vol.142, pp.417-434, 1977

(10) R. Lecomte, D. Schumitt and L. Lamoureut, "Geometry study of a high resolution PET detection system using small detectors," *IEEE Trans. Nucl. Sci.*, vol.31, pp.556-561, 1984

(11) R.F. Post and L.I. Schiff, "Statistical limitations on the resolving time of a scintillation counter," *Phys. Rev.*, vol.80, p.113-120, 1950

(12) H. Uchida, Y. Yamashita, T. Yamashita et al., "Advantageous use of new dual rectangular photomultiplier tube for positron CT," *IEEE Trans. Nucl. Sci.*, vol.30, pp.451-454, 1983

(13) M. Moszynski, C. Gresset, J. Vacher et al., "Timing properties of BGO scintillator," *Nucl. Instr. Meth.*, vol.188, pp.403-409, 1981

Chapter 3

Development of BGO Block Detector Using Position-Sensitive PMT

This chapter presents our studies on the spatial resolution of a position-sensitive PMT (PS-PMT) and the development of a block detector using the PS-PMT, where the emphasis is placed specifically on the development of a PET detector for a practical use.

In Section 3.1, a position calculation of a resistor charge division method is discussed and the spatial resolution with a BGO block detector using a PS-PMT is analyzed. The performance capability of BGO detectors is demonstrated in Section 3.2. A block detector developed for an animal PET system is described in Section 3.3.

3.1 Basic Studies on Position-Sensitive PMT

3.1.1 Position-Sensitive PMT for PET

Up to the present, a variety of position-sensitive PMTs (PS-PMTs) have been developed [1][2]. Conventional PS-PMTs employed microchannel plates (MCP) as their electron multipliers. Such devices may include image intensifier tubes and photon counting image tubes, which are now widely used in many application fields. The MCP as a position-sensitive electron multiplier has a number of features such as excellent spatial resolution (50 μm - 100 μm), very fast timing properties (TTS < 30 ps), and thin flat plate structure (0.5 mm - 1.0 mm in thickness) [3]. The PS-PMTs using MCPs, however, have drawbacks in consideration of applying them to PET. The maximum output current of MCP is several hundred nA, and thus limits the count rate capability of the PMT. The open aperture ratio of MCP is approximately 50% (defined as the ratio of the active hole area to the whole input area) and each channel input has a relatively low secondary electron emission ratio (δ=2–3), so that the net conversion efficiency from scintillation photons to primary electrons is low.

To overcome these problems with MCPs, new position-sensitive electron multipliers have been developed, which use multiple-layer of mesh dynodes [4]-[6]. Most of them were originally designed with the aim of application to detectors for high energy physics (HEP) experiments. In the HEP experiments the energy of particles or γ-rays detected is over a several MeV range, while the energy of γ-rays is 511 keV in PET. Thus the light amount per event on a PMT is considerably low in PET. For example, BGO scintillators commonly used in PET emit only about 1,500 photons per event for 511 keV γ-rays. In order to obtain good statistical accuracy in energy resolution, timing resolution and spatial resolution in PET, the PS-PMT is required to have high photocathode sensitivity, reasonably good timing properties and good electron collection efficiency. On the other hand, the pulse height linearity is not of prime importance with PET detectors, because the peak current level of output pulses is not large, especially with slow scintillators such as BGO. For applications to PET systems and scintillation cameras, a new PS-PMT (Hamamatsu R3941) has been developed, which has a 66

x 60 mm bialkali photocathode, transmission dynodes having an improved collection efficiency and a high multiplication gain, and two sets of crossed multi-wire anodes.

3.1.2 Position Calculation with Resistive Current Divider

Position calculation with PS-PMT can be analyzed in an analogy to that with a scintillation camera which has been studied by Tanaka et al. and other researchers [7][8]. Figure 3-1 shows the principle of scintillation camera.

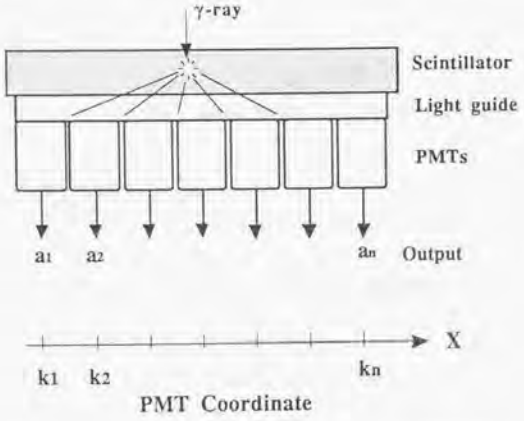

Fig.3-1 Schematic drawing of scintillation camera : Principle

In a scintillation camera, the position of an incident γ-ray, X, is calculated as a function of all PMT output $a_1, a_2, \cdots, a_n$.

$$X = X(a_1, a_2, \cdots, a_n) \tag{3-1-1}$$

Deviations of each PMT output Δa_i produces a deviation of the calculated position ΔX as follows:

$$\Delta X = \frac{\partial X}{\partial a_1}\Delta a_1 + \frac{\partial X}{\partial a_2}\Delta a_2 + \cdots + \frac{\partial X}{\partial a_n}\Delta a_n . \tag{3-1-2}$$

The variance of X, σ_X^2, is given by

$$\sigma_X^2 = \left(\frac{\partial X}{\partial a_1}\right)^2 \sigma_{a_1}^2 + \left(\frac{\partial X}{\partial a_2}\right)^2 \sigma_{a_2}^2 + \cdots = \sum_{i=1}^{n} \left(\frac{\partial X}{\partial a_i}\right)^2 \sigma_{a_i}^2 , \qquad (3\text{-}1\text{-}3)$$

where $\sigma_{a_i}^2$ is the variance of a_i. In the linear resistor weighting method, the event centroid is calculated from a position weighed average of all PMT signals. Thus,

$$X = \sum_{i=1}^{n} k_i a_i \Big/ \sum_{i=1}^{n} a_i , \qquad (3\text{-}1\text{-}4)$$

where k_i is the x coordinate of the i-th PMT center. From eq.3-1-4, we derive

$$\frac{\partial X}{\partial a_i} = \frac{k_i \sum a_i - \sum k_i a_i}{\left(\sum a_i\right)^2} = \frac{k_i - X}{\sum a_i} . \qquad (3\text{-}1\text{-}5)$$

From equations 3-1-3, 3-1-4 and 3-1-5, we derive the following equation:

$$\sigma_X^2 = \sum \frac{\left(k_i - X\right)^2}{\left(\sum a_i\right)^2} \sigma_{a_i}^2 . \qquad (3\text{-}1\text{-}6)$$

We consider a model of a PS-PMT assuming that there is no spatial spread in the electron multiplication process in the PS-PMT. When scintillation light having a spatial spread of $f(x)$ is incident upon the photocathode, and distributed on each segment (#1 - #n) as an amount of $(N_1, N_2, \cdots, N_n)$ in terms of photoelectron number arriving at the first dynode. The mean number of electrons ($\overline{a}_i$) arriving at each anode is

$$\overline{a}_i = \overline{N}_i \cdot \overline{\mu} , \qquad (3\text{-}1\text{-}7)$$

where μ is the electron multiplier gain, and it is assumed that the mean electron multiplier gain ($\overline{\mu}$) is constant for all segments. When a stochastic process having a mean value of m_1 and a relative variance of σ_1^2 is followed by another stochastic process having a relative variance of

$\sigma_{k_2}^2$, the variance resulting from their cascade process, σ_k^2, is given by $\sigma_k^2 = \sigma_{k_1}^2 + \sigma_{k_2}^2 / m_1$. The variance of a_i, $\sigma_{a_i}^2$, is thus calculated as follows:

$$\frac{\sigma_{a_i}^2}{\overline{a}_i^2} = \frac{\sigma_{N_i}^2}{\overline{N}_i^2} + \frac{1}{\overline{N}_i}\frac{\sigma_\mu^2}{\overline{\mu}^2}, \tag{3-1-8}$$

where $\sigma_{N_i}^2$ is the variance for the number of photoelectrons arriving at the first dynode, and σ_μ^2 is the variances for the number of electrons arriving at the anode.

If each N_i obeys Poisson statistics, $\sigma_{N_i}^2 = \overline{N}_i$. Thus,

$$\sigma_{a_i}^2 = \overline{N}_i\ \overline{\mu}^2\left(1 + \frac{\sigma_\mu^2}{\overline{\mu}^2}\right). \tag{3-1-9}$$

From the equations 3-1-6 and 3-1-9, we derive

$$\sigma_X^2 = \frac{1}{N^2}\left(1 + \frac{\sigma_\mu^2}{\overline{\mu}^2}\right)\sum \overline{N}_i (k_i - X)^2, \tag{3-1-10}$$

where $N = \sum_{i=1}^{n} N_i$. If we denote $N_i = N \cdot f_i$ and $\sum f_i = 1$, where f_i implies the fraction of scintillation light entering the i-th segment, then we derive

$$\sigma_X^2 = \frac{1}{N}\left(1 + \frac{\sigma_\mu^2}{\overline{\mu}^2}\right)\sum (k_i - X)^2 f_i . \tag{3-1-11}$$

The term $\sum (k_i - X)^2 f_i$ in the equation above is the variance of spatial spread function *f(x)* of the scintillation on the photocathode. The uncertainty of the calculated position (σ_X : standard deviation) is given by

$$\sigma_X = \frac{1}{\sqrt{N}}\sqrt{1 + \sigma_\mu^2}\ \sigma_e \tag{3-1-12}$$

$$\sigma_e = \sqrt{\sum (k_i - X)^2 f_i}, \tag{3-1-13}$$

where σ_e is the standard deviation of the scintillation spread function, and σ_{κ_μ} $(=\sigma_\mu/\bar{\mu})$ is the relative standard deviation for the electron multiplication. If the secondary electron emission from a dynode obeys Poisson statistics, $\sigma_{\kappa_\mu}^2$ is given by the following equation:

$$\sigma_{\kappa_\mu}^2 = \frac{1}{\delta_1} + \frac{1}{\delta_1\delta_2} + \cdots + \frac{1}{\delta_1\delta_2\cdots\delta_i}, \qquad (3\text{-}1\text{-}14)$$

where δ_1, δ_2,$\cdots$, δ_i are the ratio of the number of secondary electrons to that of the primary electrons (the secondary electron emission ratio). If each dynode has the same secondary electron emission ratio of δ=4, the value of $\sqrt{1+\sigma_{\kappa_\mu}^2}$ in eq.3-1-12 is approximately 1.15. The statistical fluctuation of the electron multiplier gain dose not largely affect the position resolution of a PS-PMT.

The equation 3-1-12 implies that decreasing the scintillation light spread on the photocathode and increasing the effective quantum efficiency are primary factors in order to obtain a good spatial resolution for a PS-PMT. In order to reduce the light spread from the crystal, we decided to use a discrete BGO array rather than a large plate scintillator as used in scintillation cameras.

3.1.3 Light Response Function

BGO has a large refractive index value of 2.15, while the glass window of a PMT and an optical coupling compound have refractive index values of 1.5 and 1.47, respectively. Thus, the output light from a BGO crystal spreads over the photocathode through the glass window as shown in Fig.3-2.

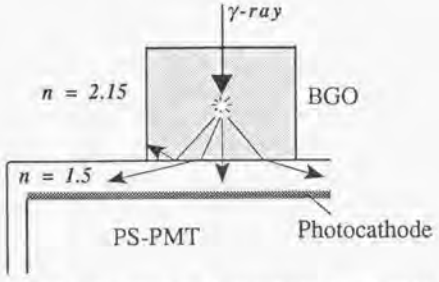

Fig.3-2 Schematic of BGO light spread on photocathode though PMT window

Using the Monte Carlo method described in Section 2.1.2, we calculated the spatial spread of scintillation photons from a 3 x 3 mm^2 cross section by 15 mm deep BGO on a photocathode through different thicknesses of glass windows. Figures 3-3 (a) to (d) show the light spread calculated for PMT glass windows of 1 mm, 2 mm, 3 mm and 4 mm in thickness. As shown in the figures, the light spread is largely affected by the window thickness, and thus a PS-PMT having a thinner glass window provides better spatial resolution with BGO.

The electron spread at the wire-anodes is calculated by the convolution between the light spread on the photocathode and the electron spread in the electron multiplier. The electron spread at the anodes in a PS-PMT was measured for a small spot illumination on the photocathode. The electron spread is near a Gaussian distribution having approximately 7 mm FWHM. We also measured the anode response function by scanning a 3 mm wide BGO on the face plate of the PS-PMT. A distribution function obtained convolving the calculated light spread with the measured electron spread, coincides well with the anode response measured for a 3 mm wide BGO crystal as shown in Fig.3-4.

We measured the image of a single BGO scintillator coupled to a PS-PMT. Figure 3-5 shows the profiles of the images measured with different widths of BGO crystals from 1 mm to 5 mm. It was found that the FWHM value of the profile is independent of the BGO width from 1 mm to 4 mm. It should be noted that the FWHM values are in the range of 1.3 mm–1.35 mm even though the crystal width ranges up to 4.0 mm. This suggests that closely packed array of crystals having 2.0 mm width or wider can be sharply separated, which is a great advantage in the use of PS-PMTs.

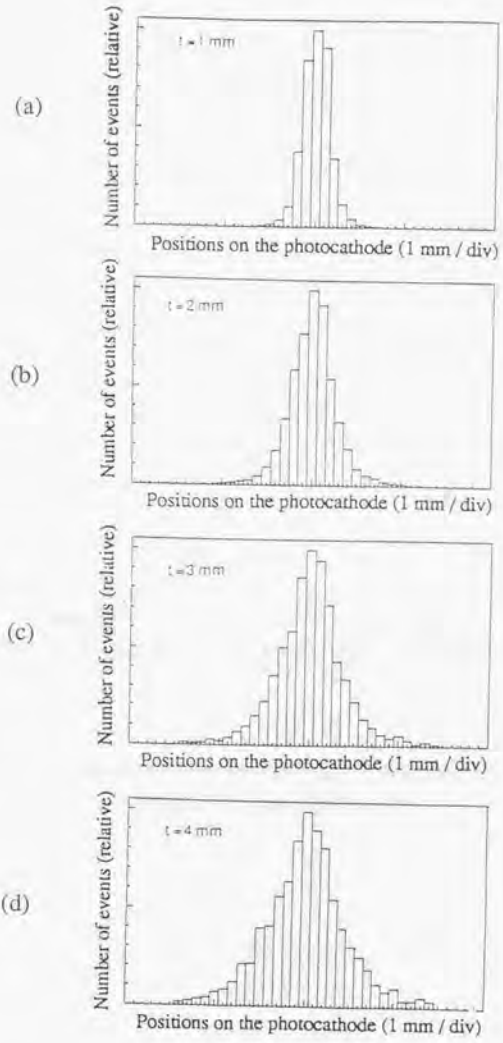

Fig.3-3 Light spread on photocathode calculated with different thicknesses of PMT windows (t : thickness of PMT glass window)

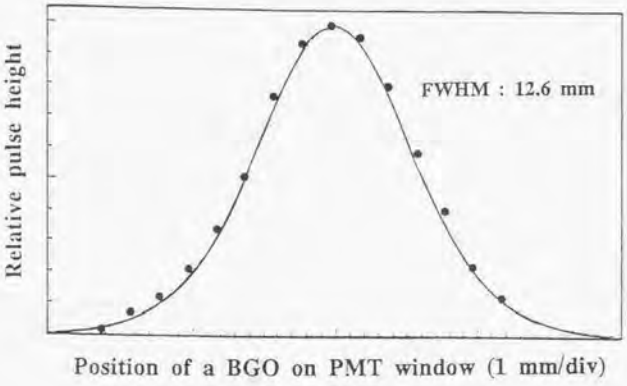

Fig.3-4 Anode response functions obtained by calculation (shown by solid line) and by measurement (shown by filled circles)

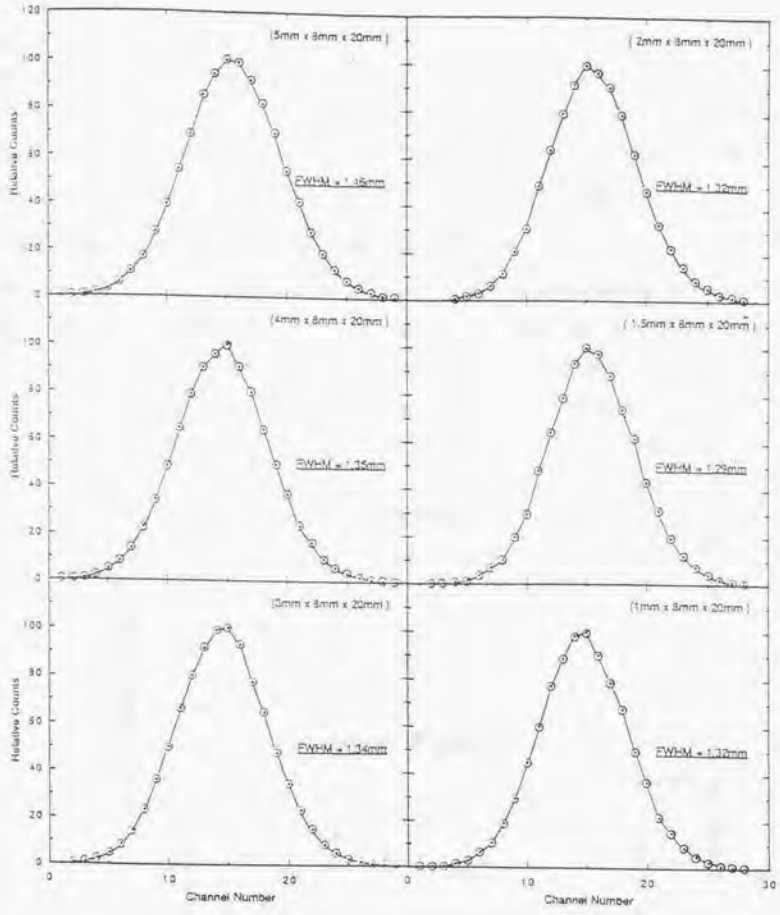

Fig.3-5 Image profiles measured with single BGO crystals having different widths (BGO : 8 mm in height and 20 mm in depth)

3.2 Performance Capability of BGO Detectors

It is important to use a thinner BGO crystal for attainment of high spatial resolution PET. A practical limit of the crystal width was studied [9]. BGO arrays having different widths of segments were prepared and their performance characteristics were measured. The segment width in each BGO array was 1 mm, 1.5 mm, 2 mm, 3 mm, 4 mm, 5 mm, and all had the same height and depth, 8 mm in height and 20 mm in depth. Each array had 5 segments and 0.5 mm thick reflectors between segments.(refer to the figure at top-right in Fig.3-8)

3.2.1 Energy and Time Resolution of Thin BGO

We measured the light output, energy resolution and coincidence time resolution of those BGO arrays using 2" diameter PMTs: Hamamatsu R1306 for the energy resolution measurement, and two R329 for the coincidence time resolution measurement. Figure 3-6 shows the dependence of light output and energy resolution on BGO width.

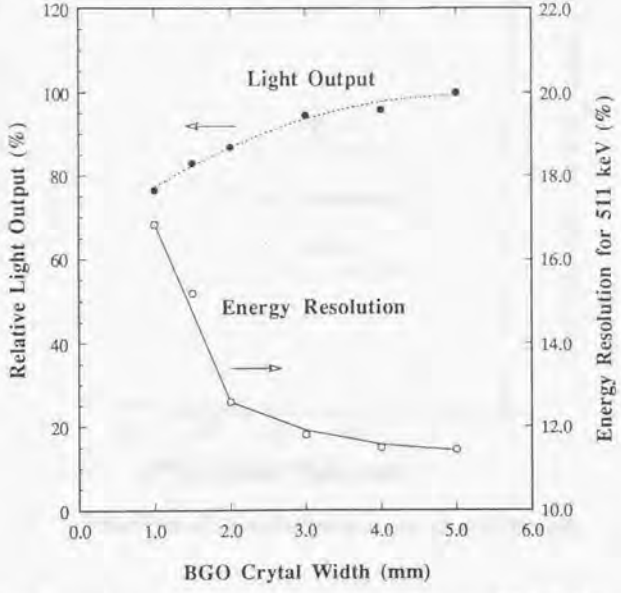

Fig.3-6 Dependence of light output and energy resolution on BGO width

The energy resolution degrades drastically with the BGO thinner than 2 mm, while the decease in light output from thin BGO crystals is not large. In a thin BGO crystal, the scintillation light emitted near the crystal top is reflected on the reflector walls many times before escaping from the crystal. The degree of light attenuation is dependent on the depth of scintillation point (top, middle, bottom) in a thin crystal, and consequently it degrades the intrinsic energy resolution of the crystal. Figure 3-7 shows the dependence of coincidence time resolution on BGO width. The coincidence time resolution is almost independent of the crystal width. In this measurement, the transit time dependence on illumination position on the photocathode (called cathode transit time difference : CTTD) of the PMTs might affect the results with thick crystal arrays which had larger coupling areas on the photocathode.

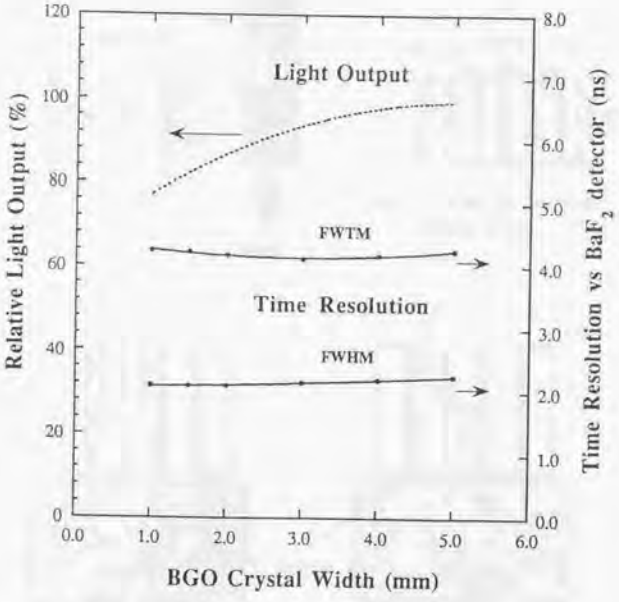

Fig.3-7 Dependence of coincidence time resolution on BGO width

3.2.2 Spatial Resolution Capability

We studied the spatial resolution capability of BGO detectors using a PS-PMT, Hamamatsu R3941. Five segment BGO arrays having different widths were coupled to the PS-PMT, and their detector response functions (DRFs) were measured in the same apparatus described in Section 2.2.5. In addition, to obtain an ideal performance in a one-to-one coupling scheme, we optically coupled only one center segment to the PS-PMT and measured the DRF. Using the DRFs measured under two different conditions above, we calculated the coincidence response functions (CRFs). The configurations of the BGO arrays and the experimental setup are shown in Fig.3-8.

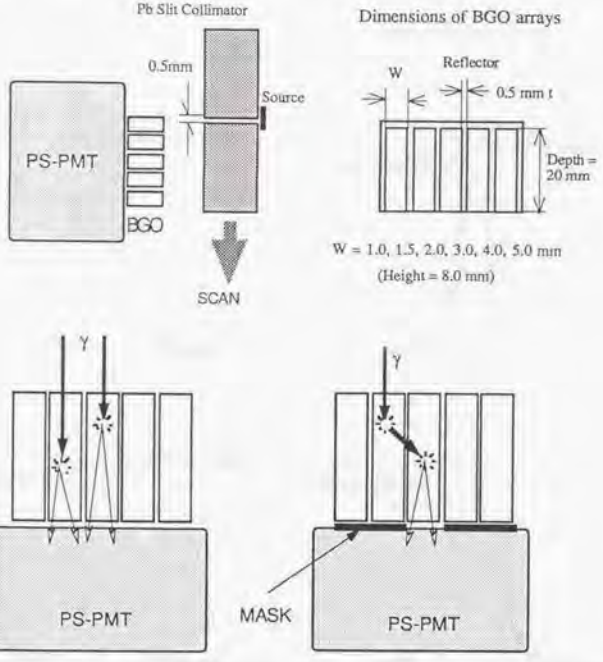

Fig.3-8 Experimental setup for the measurement of intrinsic spatial resolution of detectors (bottom left; coding scheme, bottom right; simulation for individual coupling scheme)

The calculated CRF profiles with these ideal and practical detectors are shown in Figure 3-9. Note that these CRFs are different from those obtained in a PET system, because the calculated CRFs include no physical blurring factors such as a positron range and an angular deviation.

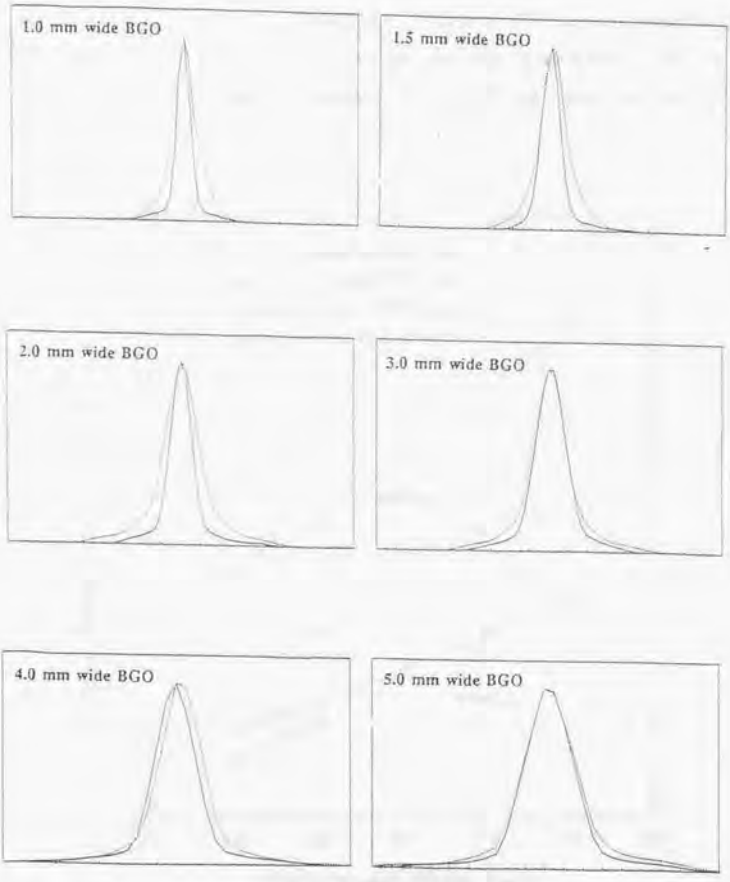

Fig.3-9 CRF profiles with coding scheme using PS-PMT (dotted line) and with ideal detector (solid line) for different widths of BGO crystals

The FWHM and FWTM values of the CRFs are shown in Fig.3-10 as a function of crystal width. The CRFs in a practical condition is poorer than those in one-to-one coupling condition, in particular with thin BGO crystals. The finite resolution capability of the PS-PMT causes crosstalk among the BGO segments, and thus degrades the CRFs, especially their FWTM values. In the ideal condition, only the crosstalk due to γ-ray scattering in the crystals affects the resolution, but this effect is not large . Thinner BGO crystals provide better resolution for both practical and ideal detectors, and a CRF having a FWHM of less than 1.5 mm is obtained with a practical detector composed of a PS-PMT and a BGO array having 1.0 - 1.5 mm wide segments.

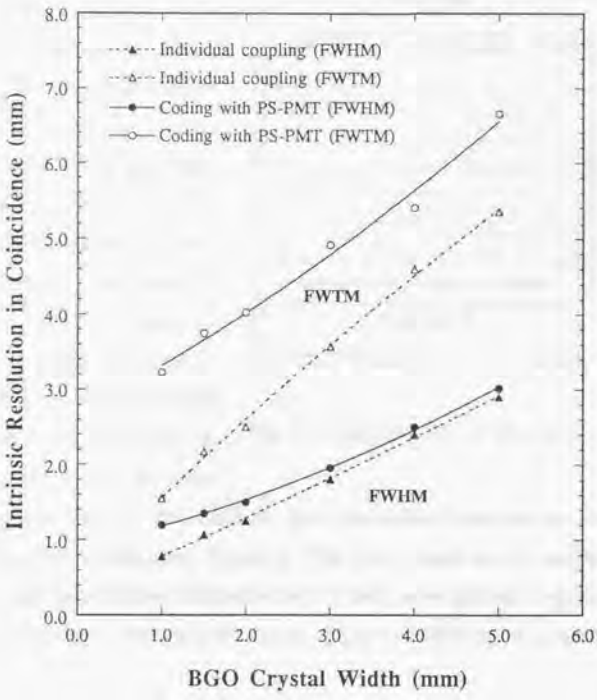

Fig.3-10 FWHM and FWTM values of CRFs as a function of BGO width

3.3 Development of BGO Block Detector for PET

3.3.1 Reduction of Edge Effect

Crystal packing ratio on a detector ring is an important factor in the design of a PET system having reasonable sensitivity. Thus it is desirable to utilize a sensitive area of the PS-PMT as large as possible. To reduce the edge effect of the PS-PMTs and extend the useful area on the photocathode, several approaches have been taken.

The anode outputs from the PS-PMT are not uniform for light inputs incident on different positions of the photocathode : the output for a light input on the peripheral region of the photocathode is smaller than that on the center region of the photocathode. Electrons gradually spread in the cascade multiplication process and some of them are lost at the periphery of the dynodes. To compensate the gain drop at the periphery in the X direction, grids for local gain control were implemented into the PS-PMT in place of the seventh and the ninth dynodes as shown in Fig.3-11. The uniformity of the gain in the X direction was controlled by adjusting the potential at these grids. Figures 3-12 (a) and (b) show the gain uniformity in the X direction and the pulse height distribution for 511 keV γ-rays uniformly irradiated on the BGO blocks, respectively, where an improvement in gain uniformity by the gain control grids is shown.

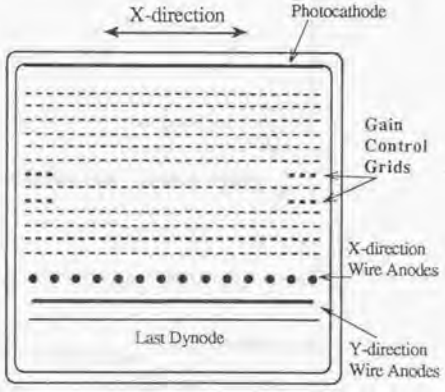

Fig.3-11 Schematic of local gain control grids

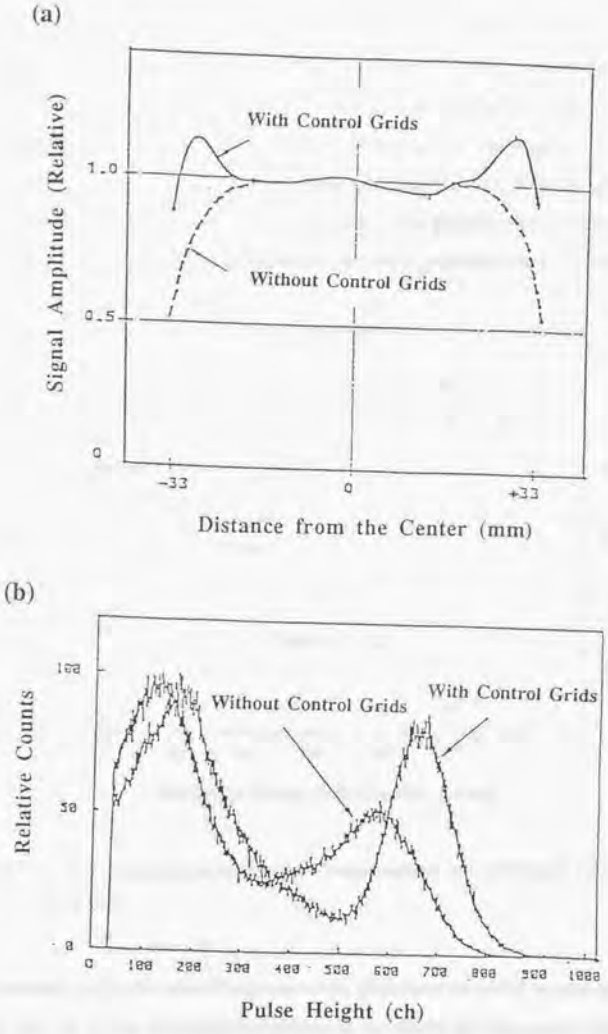

Fig.3-12 Gain uniformity and pulse height distribution of PS-PMT with and without local gain control grids

The other edge effect of the PMT is position distortion at the periphery. We connected all wire anodes in the X direction to a resistor chain, which was the standard anode read-out scheme of the PS-PMT. The responses of two outputs from the resistor chain were measured by scanning a 3 mm wide BGO crystal with 1 mm steps on the PMT window. Figure 3-13 shows the responses of the both outputs for the crystal positions on the window. The positions calculated using two outputs are also shown in the same figure. The position information is lost near the periphery because the electron trajectory of the photoelectrons emitted from the periphery on the photocathode bends and crosses over other photoelectron trajectories.

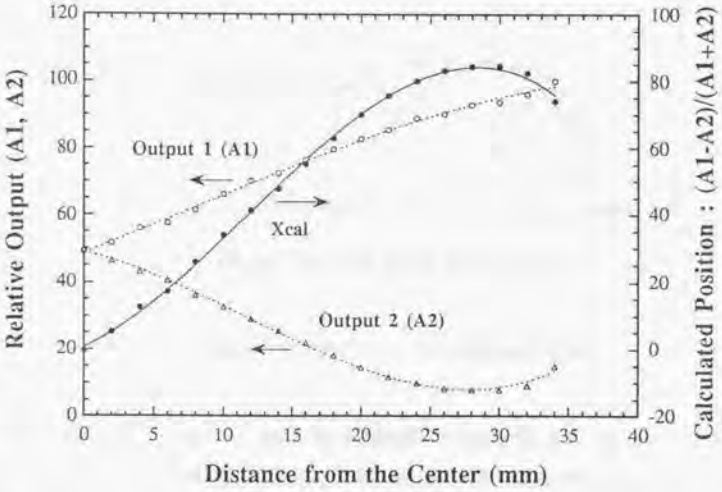

Fig.3-13 Output responses at both ends of resistor chain and calculated positions using them

We measured each wire-anode response at the periphery, of which results are shown in Fig.3-14. As shown by the normalized responses in the figure, the responses with the anode #1 and #2 are quite similar, and thus they provide the same position information. The signals from anode #1 and #2 are much smaller than those from the anode #3 and #4. Therefore, the

peripheral two anodes #1 and #2 (also #17 and #18) were connected and taken out independently.

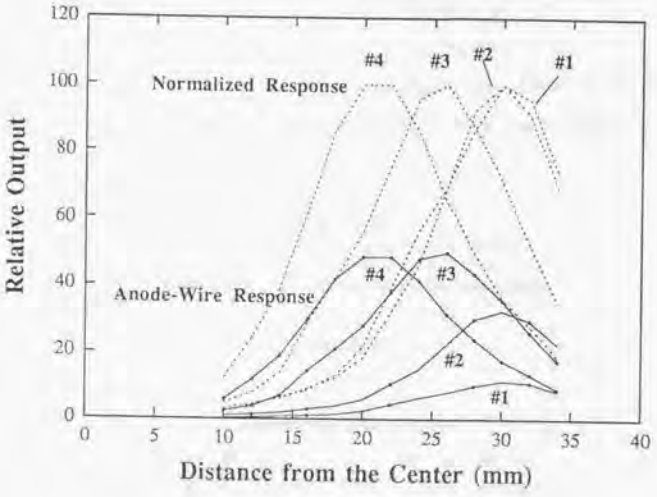

Fig.3-14 Response of peripheral anode wires in PS-PMT

The best position accuracy may be obtained by applying the optimum algorithm (Maximum Likelihood Position Estimation) based on each anode response function [10]. However, it requires rather sophisticated electronics and a number of amplifiers to pick up each anode signal separately. Thus, we modified the simple charge division method using a resistor chain. To improve the resolution in the peripheral regions, we added peripheral position calculators to the conventional calculator (central position calculator) as shown in Fig.3-15. A BGO array having 5 pieces of 3 mm wide segments (4 mm in pitch) was placed on the peripheral region on the PS-PMT window, and the capability for crystal separation was measured with the peripheral and the central calculators. As shown in Figures 3-16 (b) and (c), the peripheral position calculator separates the crystals at the periphery, where the images

obtained using the central calculator are also shown. An image of the BGO array positioned at the center on the PMT window is shown in Fig.3-16 (a) for a reference.

A 3 mm wide BGO was scanned on the PMT window with 1 mm steps, and the FWHM values of the image profiles and calculated positions (X) were measured. We defined the resolution distance as FWHM / (dX/dx). Figure 3-17 shows the results. The position accuracy (resolution distance) in the peripheral region was improved by the addition of the peripheral position calculators, and consequently a useful area on the PS-PMT was increased.

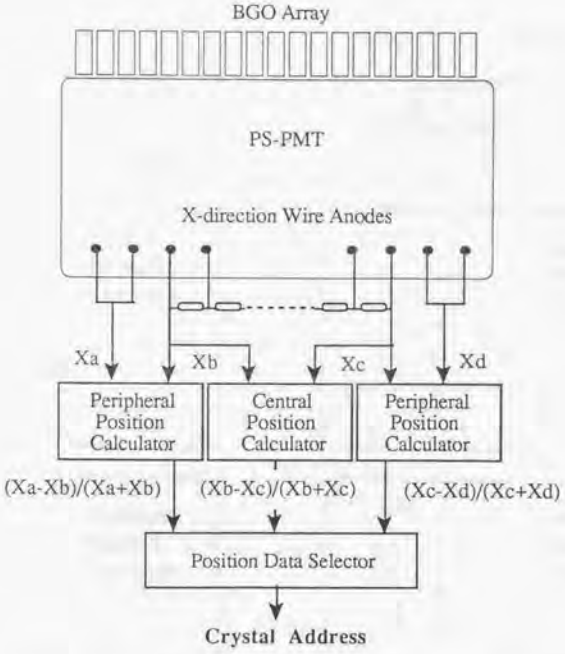

Fig.3-15 Schematic diagram of position calculator composed of a central position calculator and two peripheral position calculators

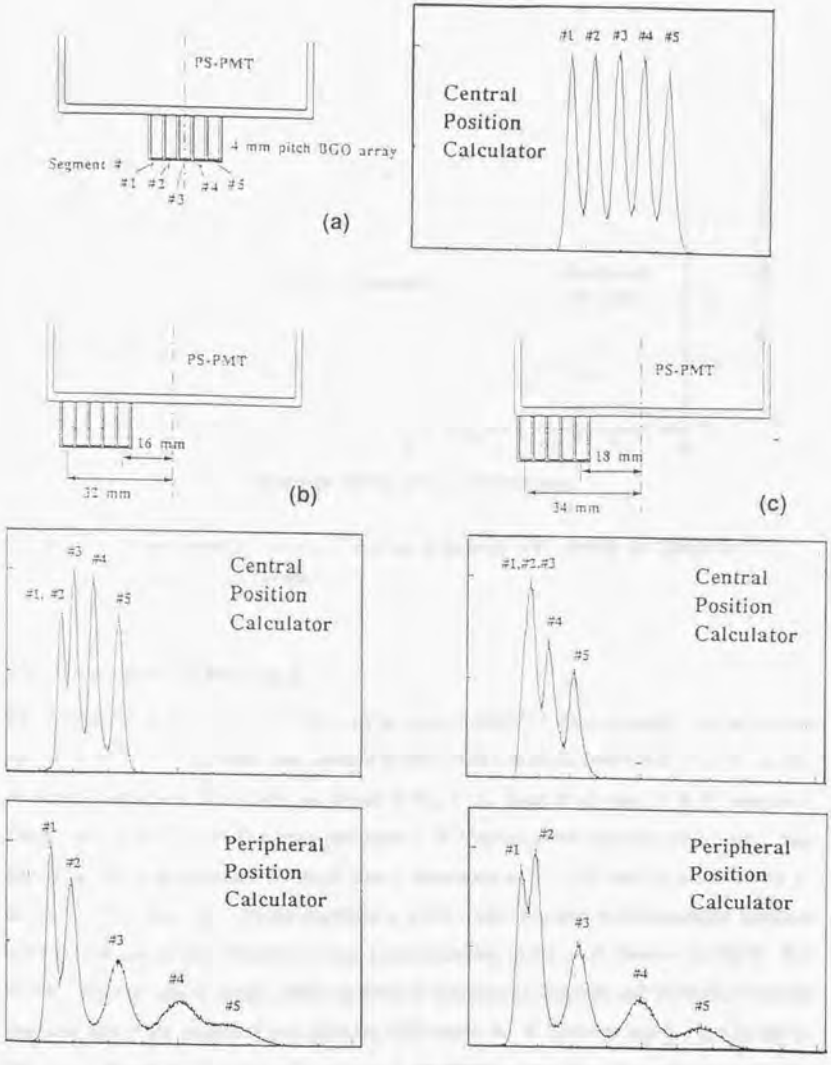

Fig.3-16 Crystal separation capabilities of central and peripheral position calculators.
(A five segment BGO array was placed at different positions on PS-PMT.)

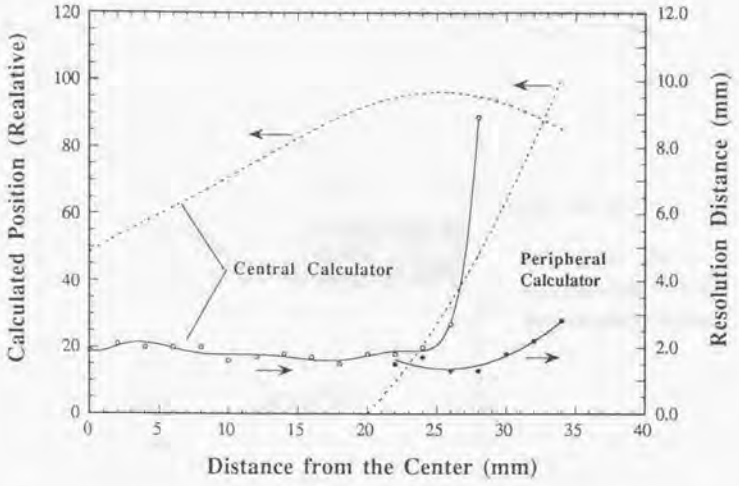

Fig.3-17 Calculated positions and resolution distance with central and peripheral position calculators

3.3.2 Detector Construction

We have developed a BGO block detector using a PS-PMT in order to apply it to an animal PET system [11]. The detector unit consists of four blocks of BGO arrays and a 76 mm square PS-PMT (Hamamatsu R3941-02) as shown in Fig.3-18. Each block has 33 BGO segments. The geometry of four BGO blocks provides a PET system with four detector rings. The individual crystal segments in the block have a dimension of 1.7 x 10 mm^2 cross section by 17 mm depth. The pitch of 33 crystal segments is 2 mm (corresponding to the transaxial direction in PET), and that of four blocks is 13 mm (corresponding to the axial direction in PET). The PS-PMT has two sets of anode wires, 18 in the X (transaxial) direction and 16 in the Y (axial) direction, where the pitches of the wires are 3.75 mm in the X-direction and 3.7 mm in the Y-direction. Figure 3-19 shows the schematic of the signal readout from the crossed-wire anodes. Wire anodes from # 3 to # 16 in the X-direction were connected to a resistor chain, while the peripheral anode wire #1 and #2, and #17 and #18 were bunched, respectively. Two

outputs at the both ends of the resistor chain and the two peripheral outputs were taken out. The anode wires in the Y-direction were connected in groups of four, and the output from each group was taken out independently.

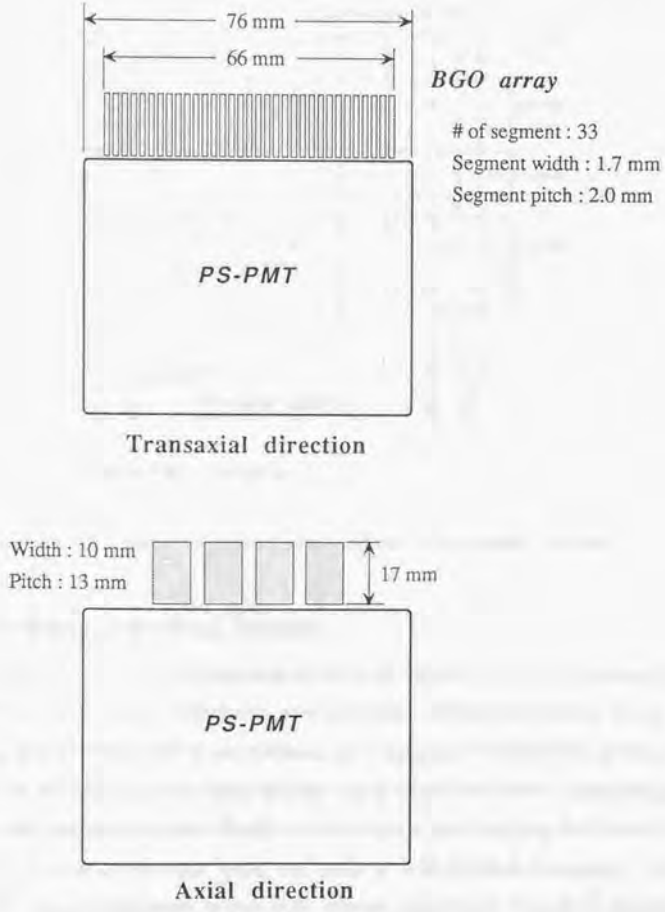

Fig.3-18 Construction of block detector using four BGO arrays coupled to PS-PMT

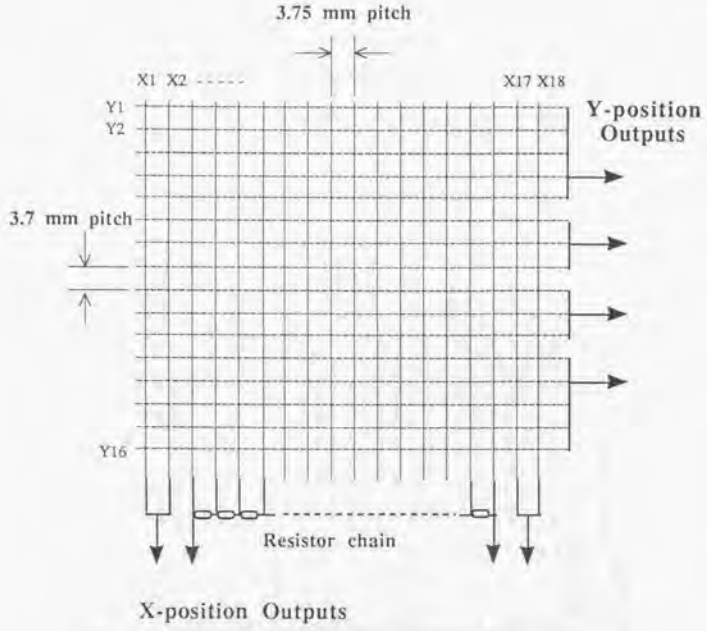

Fig.3-19 Structure of crossed-wire anode and signal readout scheme

3.3.3 Performance of the Block Detector

We evaluated the intrinsic detector resolution of the block detector. Four signal outputs from the PS-PMT for the X-position calculation were integrated and digitized through 8-bit flash analog to digital converters (ADCs), and collected into a computer (HP9000/236) in list mode. One of the four BGO arrays on the block detector was irradiated by uniform γ-rays through a 10 mm wide slit, and the data was collected in the computer until reaching 50 k events. We calculated the X position for each event, and made an 8-bit position histogram. In the histogram, 33 peaks corresponding to each BGO segment were found. We set 33 channels of position windows corresponding to the BGO segments in the histogram by properly determining the position discriminator levels at valleys between peaks. The detector response

functions (DRFs) in the X-direction were measured by scanning a collimated line source through a 1 mm wide slit. The measured DRFs for the 33 channels are shown in Fig.3-20. Each 1.7 mm wide BGO segment (2 mm in pitch) was separated with small crosstalk from the adjacent channels. The FWHM value averaged over the 33 segments is approximately 2.0 mm.

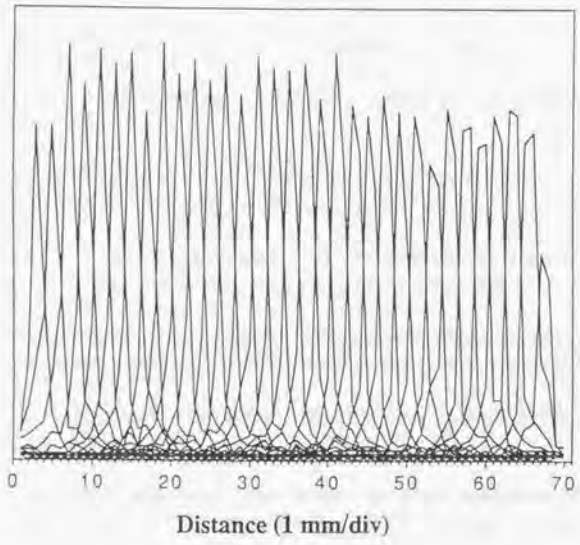

Fig.3-20 Detector response functions of 33 BGO segments of block detector

The time resolution of the block detector was measured using a BaF_2 reference probe in coincidence. A time resolution of 5 ns FWHM was obtained, which could provide BGO-BGO time resolution of 7 ns FWHM. The energy resolution of the block detector is 30 % at full illumination of 511 keV γ-rays on the BGO blocks, which is worse than that obtained for a spot illumination of γ-rays (20 %). The nonuniform anode sensitivity of the PS-PMT degrades the energy resolution at the full crystal illumination.

References

(1) Y. Tsuchiya, E. Inuzuka, T. Kurono et al., "Photon-counting image acquisition system and its applications," *J. Imag. Tech.*, vol.11, pp.215-220, 1985

(2) *Hamamatsu Photonics Catalog* "Electron Tube Product" (1990)

(3) *Hamamatsu Technical Manual* : RES-0795, "Characteristics and applications of microchannel plates"

(4) K. Kuroda, D. Sillou and F. Takeuchi, "New type of position sensitive photomultiplier," *Rev. Sci. Instr.*, vol.52, pp.337-346, 1981

(5) S. Suzuki, T. Suzuki, T. Matsushita et al., "New mesh PMTs for high magnetic environments," *IEEE Trans. Nucl. Sci.*, vol.33, pp.377-380, 1986

(6) H. Kume, S. Suzuki, J. Takeuchi et al., "Newly developed photomultiplier tubes with position sensitivity capability," *IEEE Trans. Nucl. Sci.*, vol.32, pp.448-452, 1985

(7) E. Tanaka, T. Hiramoto and N. Nohara, "Scintillation cameras based on new position arithmetics," *J. Nucl. Med.*, vol.11, pp.542-547, 1970

(8) R.M. Gray and A. Macovski, "Maximum a posteiori estimation of position in scintillation cameras," *IEEE Trans. Nucl. Sci.*, vol.23, pp.849-852, 1976

(9) T. Yamashita, M. Watanabe, K. Shimizu et al., "High resolution block detectors for PET," *IEEE Trans. Nucl. Sci.*, vol.37, pp.589-593, 1990

(10) T.D. Milster, L.A. Selberg, H.H. Barrett et al., "A modular scintillation camera for use in nuclear medicine," *IEEE Trans. Nucl. Sci.*, vol.31, pp.578-580, 1984

(11) M. Watanabe, H. Uchida, H. Okada et al., "A high resolution PET for animal studies," *IEEE Trans. Med. Imag.*, vol.11, pp.577-580, 1992

Chapter 4

Development of Animal PET Using Position-Sensitive Detector

This chapter presents the development of high resolution PET for animal studies, to which newly designed block detectors using the position-sensitive photomultiplier tubes (PS-PMT) were applied.

There are increasing demands for a PET system dedicated to *in vivo* animal studies including oxygen and glucose metabolism, blood flow, and neurotransmission system behaviors. PET animal studies are important not only as pre-clinical studies for human but also as basic studies.

Despite these well recognized advantages, PET animal studies have not been widely performed because current PET systems, designed for human studies, do not have the spatial resolution required for imaging the much smaller animal organs than those of humans. Since detectors using PS-PMTs have the capability of providing much higher resolution than the conventional PET detectors, a new block detector using the PS-PMT was developed and applied to a high resolution PET system dedicated to animal studies.

4.1 Design Criteria of Animal PET

Animal studies using radiotracers have played an important role in biological research. Most animal studies are made using low energy β-emitters such as ^{14}C or ^{3}H, and the analysis of the tracer distribution in the animal bodies is performed by *in vitro* counting of sampled tissue or by autoradiography after sacrificing the animals. The method is therefore not suitable for fast kinetic studies that need a large number of animals, or for experiments using expensive animals such as primates. In addition, the specific activities of these isotopes are limited due to their half-lives, and accordingly it becomes difficult to study the metabolism of extremely small amounts of bioactive substances. With the progress of PET technology, there has been increasing need for scanners dedicated to animal studies. The ability to assess biochemical change in living laboratory animals has great potential in biomedical research. *In vivo* animal imaging is particularly useful for repeated kinetic studies with different tracers or with different conditions within the same animal subject. Animal studies are important not only as preclinical studies for humans but also as basic studies such as physiological experiments by stimulation, investigation of drug efficacy, and the development of new drugs [1][2]. Animal PET studies provide the opportunity to repeat studies without restriction of radiation dose, to control physiological conditions before and during the experiment, and eventually to perform autoradiography or neurochemical studies.

The size of the field-of-view, the spatial resolution, and the mechanical or geometrical specifications of the animal scanner are largely dependent on the species of animals to be used, the target organ of interest, and the purpose of the experiments. Small rodents such as mice, rats or guinea pigs are often useful for the studies of kinetic models of tracers or pathophysiological studies of disease. Larger animals such as rabbits, dogs, cats and monkeys are used in more detailed physiological studies of a particular organ such as the brain, lung, heart, liver, etc. This includes studies of oxygen and glucose metabolism, blood flow, tumor perfusion, and neurotransmission system behaviors.

Due to the fact that there is always a trade-off between resolution and sensitivity in PET system design, emphasis should be placed on an increase in spatial resolution than sensitivity.

This is because of the smaller homotypic structure size within animals as compared to humans. Multi-slice imaging capability is important for acquisition of structural volume information. The detector gantry and the positioning equipment for animals should be more flexible than human scanners and should match the habits of the animals. For example, dogs are usually positioned on their side, rabbits are positioned on their stomachs, and monkeys prefer a sitting position on a chair with a suitable head-holder. Measurement with a primate being able to be positioned and studied in a sitting position will mean a shortening of training times for studies without anesthesia. The gantry should tilt throughout a large angular range, and the bed should move both horizontally and vertically. Compact design of the system, especially that of the gantry, is desired for its installation in the existing animal research laboratories or PET research facilities. The design criteria for the animal PET is summarized as follows [3]:

- High resolution capability
- Moderate sensitivity
- Multi-slice imaging capability
- Capability to measure a variety of animals from rat to primate
- Compactness

4.2 System Construction

We have developed a high resolution PET system dedicated to animal studies (Hamamatsu SHR-2000), to which the block detectors using PS-PMTs (described in Section 3.3) were applied [4]. The block diagram of the system construction is shown in Fig.4-1.

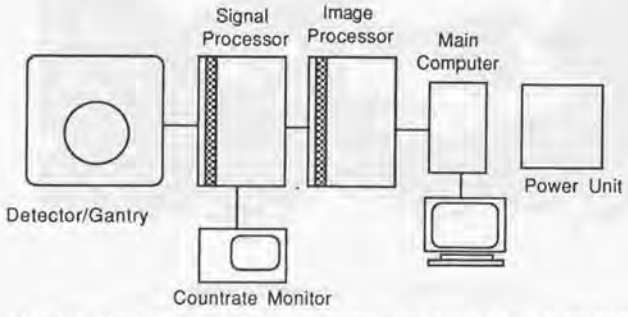

Fig.4-1 Block diagram of system construction; Animal PET SHR-2000

The system consists of a detector/gantry unit, a signal processing unit, a data acquisition unit, a host computer control system, a count rate monitor and a power supply unit. The system is designed compact by virtue of the use of the PS-PMT detectors. The external view of the gantry/detector unit is shown in Fig.4-2. The gantry is designed to provide positioning capabilities allowing flexibility and ease of use in subject positioning. Primate studies can be carried out while the animal is positioned in a sitting position.

Fig.4-2 External view of gantry/detector unit

4.2.1 Detector Ring Geometry

The arrangement of the detector blocks in the gantry is shown in Fig.4-3. Fifteen block detectors, with a total of 1980 crystals (495 per ring), are positioned to form a 35 cm diameter ring. The four blocks of the BGO arrays form four detector rings, which provide the system with a seven slice imaging capability; four direct imaging planes and three cross imaging planes. Annular tungsten alloy slice collimators are mounted internal to the detector rings. The slice collimators are tapered, providing an aperture width of 8 mm at the detector face. The transaxial field of view (FOV) is 17 cm in diameter and the axial FOV is 4.6 cm.

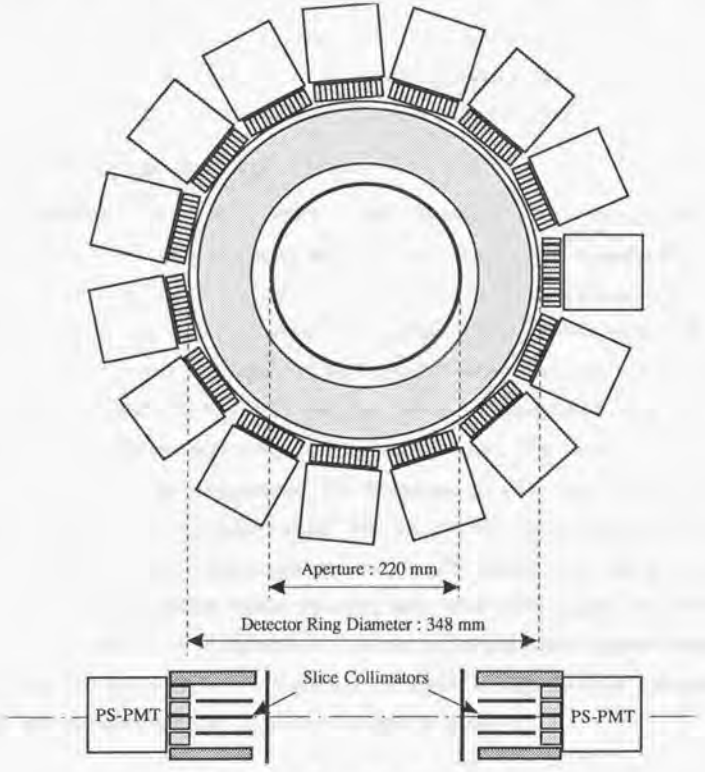

Fig.4-3 Arrangement of block detectors in the gantry

Small gaps between the individual block detectors produce diagonal blank patterns on the projection data map (sinogram), thus small angle rotation scan motion, rotating forth and back by 24° alternatively, has been adopted to fill these blank areas on the sinogram with properly acquired data. The rotation scan of the detector ring improves the uniformity of the detector sensitivity because of an averaging effect in the angular direction on the sinogram. Although the rotation scan does not increase linear sampling density in projections as wobble-motion scan does, the pitch of effective sampling density is equal to a half crystal pitch of the BGO segments. The sampling density of 1.0 mm is much smaller than the resolution distance of the system (3.0 - 3.5 mm as shown later), thereby providing sufficient data sampling density.

The gantry has a detector ring tilt capability of +/-90°, as well as vertical ring movement of 30 cm, so that great flexibility in subject positioning is attained. The gantry entry diameter is 22 cm. The major aspects of the system construction are listed in Table 4-I.

4.2.2 Electronics and Data Acquisition

The block diagram of the signal processing circuit is shown in Fig.4-4. Analog signals from each PMT are sent to a signal processing unit by coaxial cables through a preamplifier/driver circuit mounted on each detector module. The width of the PMT output pulses are shortened to 350 ns by the use of a delay-line pulse clipping method. The signal from the dynode is fed into a timing discriminator. The signals of the Y-direction wire anodes, which are positioned parallel to the direction of the four BGO arrays, are used for the energy discrimination and the determination of a flashed BGO array (coded as ring address). The flashed BGO array is detected by the use of fast comparators. The X-position calculation is carried out with a charge division method using a resistor chain. For an improvement of position accuracy in the peripheral region, four signal output taps are attached to the resistor chain, and the positions are calculated in the peripheral regions separately from those in the central region (refer to Section 3.3.2). The wire anode signals for X-position are integrated and digitized through 8-bit flash analog to digital converters (ADC), and a flashed BGO segment in the X-direction is detected by a centroid calculation using a look-up-table in EPROM.

Table 4-I Major aspects of the system construction

Detector	
Crystal material	BGO
Crystal segment size	1.7 mm (w) x 10 mm (h) x 17 mm (d)
Crystal segment pitch	2.0 mm
PMT	76 mm square position-sensitive PMT (Hamamatsu R3941-02)
Number of crystal segments	1980 (495 /ring)
Ring Geometry	
Number of rings	4
Ring diameter	348 mm
Ring separation	13 mm
Slice aperture	8 mm
Slice collimator	47 mm long, 5-6 mm thick (tapered)
Opening diameter	220 mm
Transaxial field of view	170 mm
Axial field of view	47 mm
Gantry	
Tilt angle of detector ring	–90° to +90°
Vertical stroke of detector ring	300 mm
Scanning motion	Small-angle rotation (24°)
Positioning of subject	by cross-hair laser markers
Normalization source	Orbiting ^{68}Ge rod

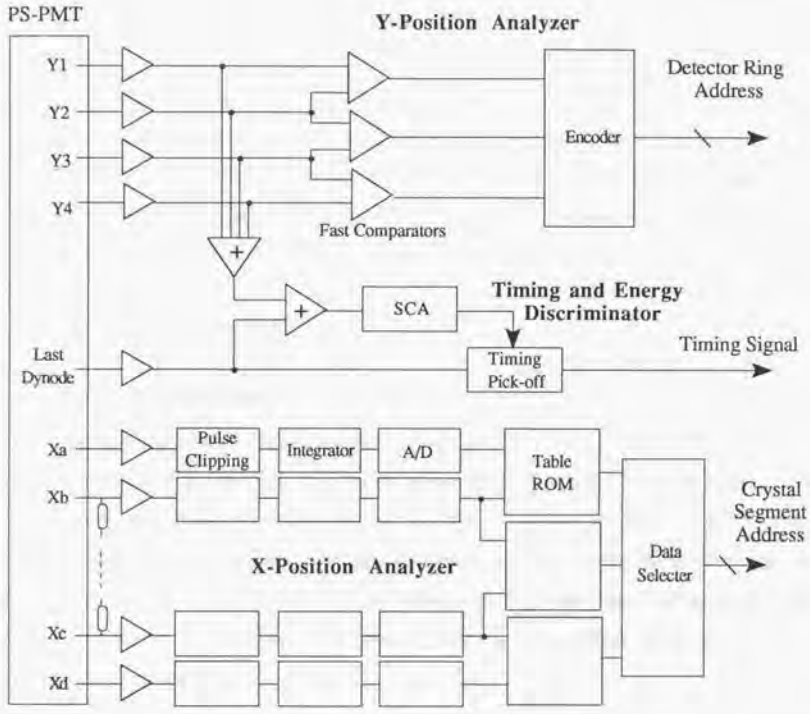

Fig.4-4 Block diagram of signal processing circuit

Each one of fifteen block detectors is in coincidence with the opposing six block detectors. The width of the coincidence time window can be changed electronically from 8 ns to 28 ns in steps of 4 ns and is normally set to 20 ns. The crystal pairs' addresses including their slice address are led to an address conversion circuit through fast-in-fast-out (FIFO) memories, where the detector pair address is converted to a projection data in each angle for sinogram formation, being combined with a detector rotation encoder signal. The converted

data of 180 (bins, sampled every 1 mm) x 225 (angles) are stored in a histogram memory in the data acquisition unit. The histogram memory consists of a pair of memory bank sets, each of which has a 4 MB memory. The acquired data are stored in one of the two histogram memory banks, concurrent with the other bank being dumped to a 300 MB hard disk.

Image reconstruction is performed by a dedicated array processor contained in the data acquisition unit. Pseudo real-time images can be displayed in a 40 x 40 pixel image on a screen during data acquisition. The real-time image monitor provides the investigator with information such as subject positioning or tracer arrival, without the lengthy lag times introduced by the necessity of post-study reconstruction.

4.3 System Performance

4.3.1 Spatial Resolution

Transaxial resolution was measured with a 1 mm diameter ^{22}Na point source placed along the radial direction at 0, 2, 4, 6 and 8 cm from the center of the transaxial FOV in each slice. The images were reconstructed with the Shepp-Logan filter, and the FWHM and FWTM of the profiles were determined in the radial and tangential directions using linear interpolation. Figure 4-5 shows the obtained transaxial resolution with the small angle rotation mode. The FWHM value is 3.0 mm at the center of the FOV, and is less than 3.5 mm in the central region of about 10 cm in diameter.

Axial resolution was measured by scanning a 1 mm diameter ^{22}Na point source in steps of 1 mm increments, in the direction parallel to the ring axis at distance of 0, 2, 4, 6 and 8 cm from the ring axis. The count rate of each slice was recorded at each scanning point. The results are shown in Fig. 4-6. The axial resolution at the center of the FOV is 4.8 mm FWHM and 8.7 mm FWTM in the direct plane, and 4.1 mm FWHM, 7.5 mm FWTM in the cross plane.

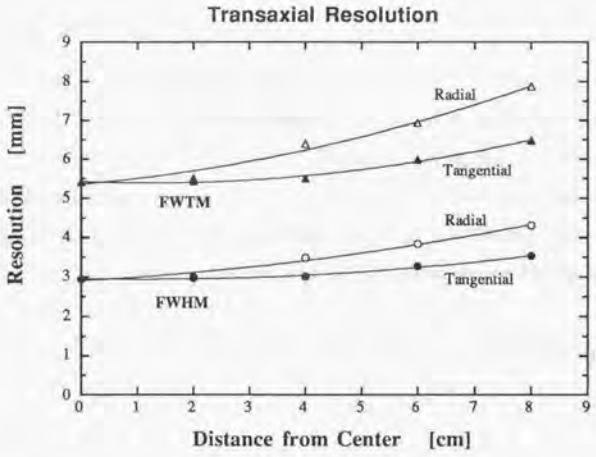

Fig.4-5 Transaxial resolution of the system as a function of distance from the center of the FOV

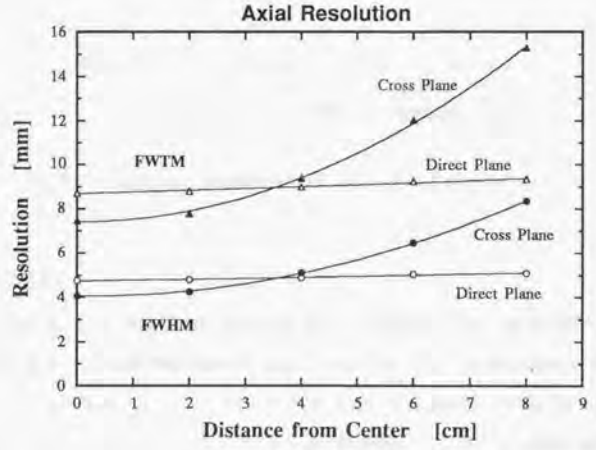

Fig.4-5 Axial resolution of the system as a function of distance from the center of the FOV

4.3.2 Count Rate Performance

Count rate performance was measured with a 10 cm diameter by 10 cm height cylindrical phantom uniformly filled with a $^{13}NH_3$ solution. The initial activity was 48.3 μCi/ml and measurements were performed for 110 minutes. Figure 4-7 shows the count rate performance as a function of the activity concentration. The true event count rate loss is approximately 30 % at 5.0 μCi/ml. The maximum total coincidence count rate is 100 kcps. The count rate loss is corrected referring to the single event rate after the data acquisition in PET studies.

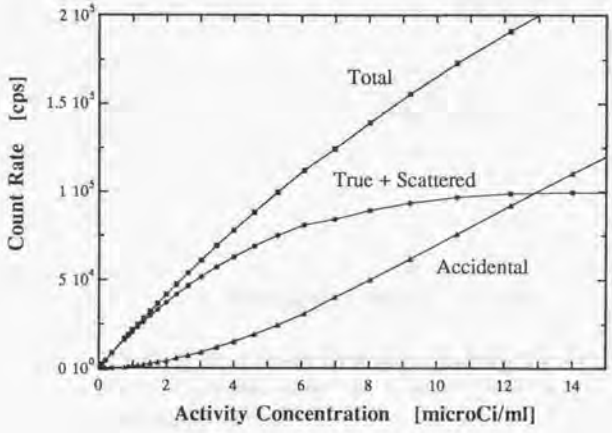

Fig.4-7 Count rate performance as a function of activity concentration

4.3.3 Sensitivity

System sensitivity was calculated from the data acquired in the count rate performance measurements with a 10 cm diameter cylindrical phantom. By extrapolation of the count rate data for low activity less than 0.5 μCi/cc, we calculated the sensitivity as the count rate at 1 μCi/cc. The averaged direct slice sensitivity is 2.3 kcps/μCi/ml, and the cross slice sensitivity is 3.8 kcps/μCi/ml. The total system sensitivity is 20.7 kcps/μCi/ml including the scatter component.

4.3.4 Coincidence Time Window

The coincidence time window width (CTWW) was changed electronically from 8 ns to 28 ns in steps of 4 ns, and then the system sensitivity at each CTWW setting was measured. Figure 4-8 shows the variation of the coincidence count rate by changing the CTWW. Although normally CTWW is set to 20 ns, CTWW can be set down to 16 ns without significant sensitivity losses.

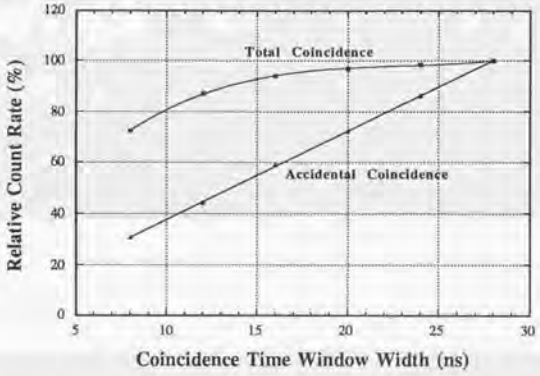

Fig.4-8 Dependence of coincidence event-rate on coincidence time window width (Each coincidence rate is normalized at the coincidence time window of 28 ns)

4.4 Animal Studies

Animal studies have been carried out with rats, dogs and monkeys. Figure 4-9 shows glucose metabolism images with ^{18}F-fluorodeoxyglucose in a rat brain. Data was collected over 120 min (4 frames of 5 min measurements followed by 10 frames of 10 min measurements) following injection of about 10 mCi. The images shown are integrated over 30 min after 30 min from the injection.

Figure 4-10 shows dopamine D_2 receptor images with ^{11}C-N-methylspiperone in a rhesus monkey brain. The images were reconstructed using the data collected for 10 min after 30 min from the tracer injection (5 mCi).

Posterior

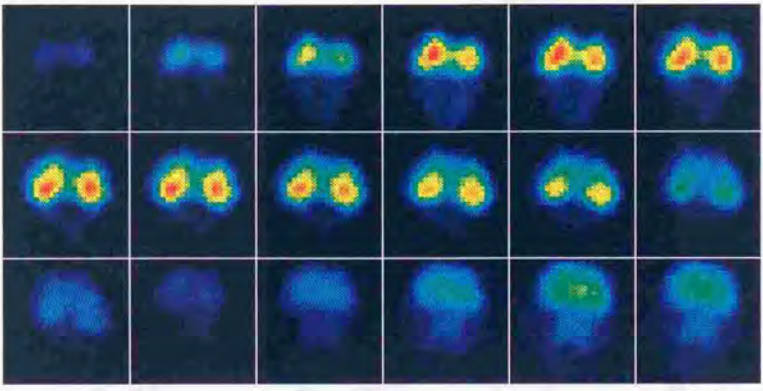

Anterior

Superior

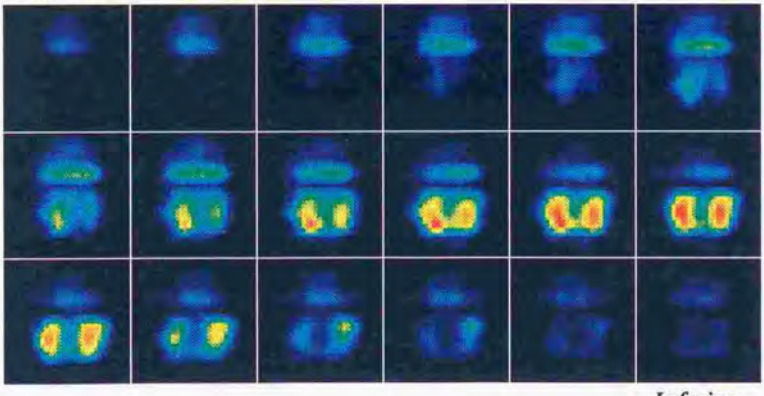

Inferior

Fig.4-9 Glucose metabolism images with ^{18}F-fluorodeoxyglucose in a rat brain
(Bottom images were reconstructed from the upper transaxial images)

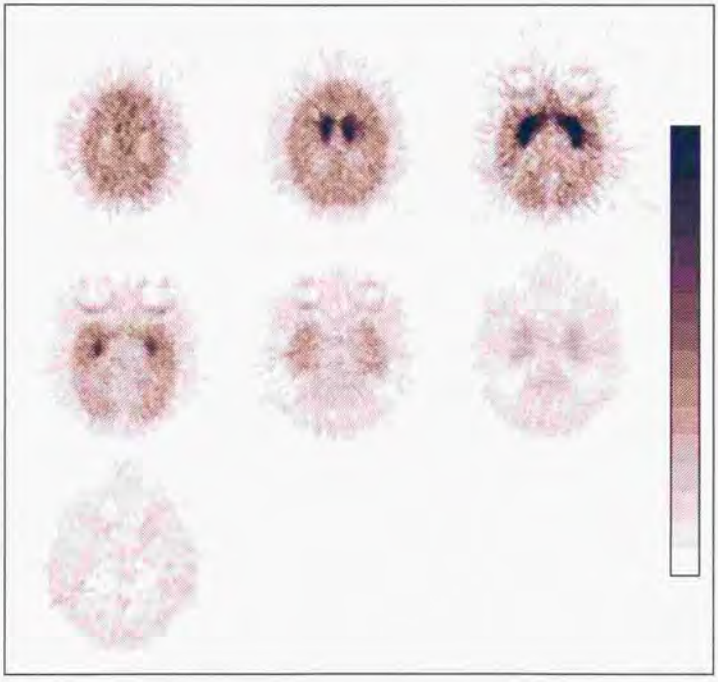

Fig.4-10 Dopamine D_2 receptor images with ^{11}C-N-methylspiperone in a rhesus monkey brain (Courtesy of The National Institute Radiological Sciences)

4.5 Discussion

The radial spatial resolution of a PET system having a ring detector geometry degrades towards the periphery of the transaxial FOV, while a system having a polygonal detector arrangement such as a hexagonal NaI(Tl) bar camera (PENN PET) provides moderately uniform resolution over the entire FOV, due to averaging of detector responses at different angles of γ–ray incidence [5]. Figure 4-11 shows an illustrative explanation of the averaging effect on spatial resolution with a polygonal detector arrangement. The animal PET system having a polygonal arrangement of 15 block detectors shows similar effect, and it provides moderately uniform radial resolution over a large area of the FOV (refer to Fig.4-5 in Section 4.3.1).

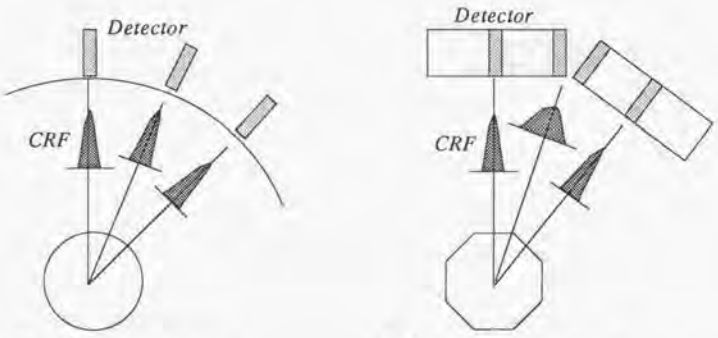

Fig.4-11 Illustrative explanation of averaging effect on spatial resolution with polygonal detector arrangement

Figure 4-12 shows a comparison between the measured system resolution and the calculated coincidence response function (CRF) of detectors in a circular arrangement. The positions of filled-circle symbols are calculated from the relation between the detector ring diameter and the angles of γ–ray incidence on the block detector, assuming a circular

arrangement. The resolution of the animal PET in the center of FOV is largely affected by a blurring effect due to the use of a polygonal detector arrangement, and also by a blur associated with the image reconstruction The radial resolution in the peripheral FOV, instead, is not blurred to large extent, which is contrary to a PET system with a ring detector arrangement.

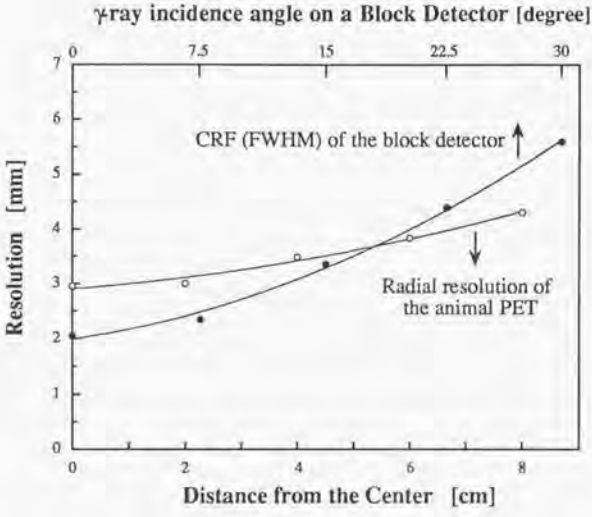

Fig.4-12 Comparison between radial resolution of animal PET at different distance from the center and CRF (FWHM) of block detector at different γ-ray incident angles

A drawback of block detectors is a limitation in count rate capability due to pulse pile-up [6]-[8]. Since the block detector in this system has a dead time of 400 ns due to the period for pulse integration, two or more events detected within this period can not be utilized. In the measurements made with a 10 cm diameter cylindrical uniform phantom, the count rate loss for true events is approximately 30 % at 5.0 μCi/ml. However, the count rate is much lower in most animal experiments using PET. The pulse pile-up events is rejected by the upper energy

discriminators to some extent, but this cannot reject all pile-up events because of the broad pulse height distribution. Since the remaining pile-up events could cause mispositioning, it is desired to introduce an additional fast pulse pile-up rejecter. The most promising scheme for improving the count rate capability of the system will be to use PS-PMTs having independent multi-anodes. An application of PS-PMTs having smaller dimensions than the present 76 mm square PMTs will be another possible way to improve the count rate capability of the system.

References

(1) F.A. King, C.J. Yarbrough, D.C. Anderson et al., "Primates," *Sience*, vol.240, pp.1475-1488, 1988

(2) J.S. Perlmutter, "PET measured evoked brain blood flow responses in an awake, trained nonhuman primate," In *Proceedings of The Third International Conference: Peace through Mind/Brain Science*, pp.45-51, Hamamatsu, 1990

(3) J.M. Links, "Functional criteria for an animal PET scanner," In *Proceedings of The Second International Conference: Peace through Mind/Brain Science*, pp.86-89, Hamamatsu, 1989

(4) M. Watanabe, H. Uchida, H. Okada et al., "A high resolution PET for animal syudies," *IEEE Trans. Med. Imag.*, vol.11, pp.577-580, 1992

(5) J.S. Karp, G. Muhllehner, D. Beerbohm et al., "Event localization in a continuous scintillation detector using digital processing," *IEEE Trans. Nucl. Sci.*, vol.33, pp.550-555, 1986

(6) G. Germano, E.J. Hoffman and M. Dahlbom, "An investigation of methods of pileup rejection for 2-D array detectors employed in high resolution PET," In *Conference Record of the 1990 IEEE Nuclear Science Symposium*, vol.2, pp.1263-1269, 1990

(7) G. Muhllehner and J.S. Karp, "A positron camera using position-sensitive detectors," *J. Nucl. Med.*, vol.27, pp.90-98, 1986

(8) C.J. Thompson and E. Meyer, "The effect of live time in components of a positron tomograph of image quantification," *IEEE Trans. Nucl. Sci.*, vol.34, pp.337-343, 1987

Chapter 5

New Detector Providing 3D Position Information of γ-ray Interaction

This chapter presents a new method which could provide PET systems with uniform spatial resolution over the entire field of view (FOV). In high resolution PET systems using thin slender crystals, the radial resolution degrades toward the peripheral FOV. The proposed detector scheme can detect the depth-of-interaction (DOI) of γ-rays in the scintillation crystals, and thus improves the resolution uniformity.

Section 5.1 describes the origin of spatially-variant resolution in circular ring PET systems, and also reviews the work carried out by other researchers in order to solve this problem. Section 5.2 presents a detector module providing three-dimensional position information, which uses bundled pillar BGO crystals coupled to two PS-PMTs at their both ends.

5.1 Resolution Uniformity in the Field of View

5.1.1 Variations in Coincidence Response Function

In order to obtain high quality image and accurate quantitative data, it is important that the spatial resolution be uniform throughout the transaxial field of view (FOV). Thus the degradation of the radial resolution towards the periphery of the FOV is a serious problem to be dealt with when designing PET to achieve resolution close to the physical limit. The nonuniformity of the spatial resolution is caused partly by the angle of the detector with respect to the source and partly by the fact that γ-rays can penetrate a crystal and be registered in the adjacent detector. (These are similar to an effect known as a parallax error in a scintillation camera.) Figure 5-1 illustrates the schematic of the radial blurring in a PET system. As the depth of crystals is increased to obtain a higher sensitivity and the width of individual detectors is reduced to obtain a higher spatial resolution, the blurring of radial spatial resolution increases. (The variation in shape and width of coincidence response functions (CRF) at different angles of γ-ray incidence can be calculated for a given geometry of crystals using the equation 2-2-5 described in Section 2.2.3.) The CRF variation in the radial direction is distinct, while that in the tangential direction is small. A larger ring PET system has smaller variations of resolution uniformity compared to a smaller ring system, if the same subject is measured.

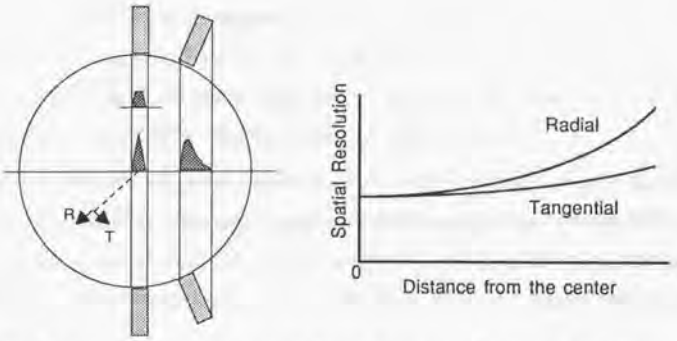

Fig.5-1 Schematic of radial blurring of spatial resolution with circular PET system

5.1.2 Trials Improving Resolution Uniformity in PET

In order to solve the problem of the resolution nonuniformity in the FOV, several attempts have been made. They involve mathematical restoration of the tomograph data or measuring the depth of interaction (DOI) of γ-rays in the detectors.

Huesman et al. reported a compensation method for crystal penetration, which applied a mathematical method of deconvolving the sinogram of the ring detector with a simulated crystal penetration kernel [1]. Although the mathematical method does not require any special design of detectors, it amplifies the statistical noise in the deconvolution process.

Karp et al. proposed the determination of the DOI using a temperature gradient in a scintillator [2]. Since the decay time of scintillation from many scintillators is temperature-dependent, the DOI can be detected by discriminating the shape of pulses from a scintillator having temperature gradient in depth. In this method, temperature controllers have to be attached to all detectors used in a system. The temperature gradient causes variations of light yield in depth, and consequently may degrade the energy resolution and also may cause variations of detection efficiency in depth.

Roger et al. measured the width of the light distribution from a NaI scintillator to detect the DOI; this technology had been used for a scintillation camera having a thick NaI scintillator to detect cosmic γ-rays [3]. This scheme of detector may have relatively low detection efficiency because of the use of the NaI(Tl) scintillator.

McIntyre et al. built an experimental setup using a three dimensional array of many small plastic scintillators coupled to PMTs with many long light pipes [4]. Since it utilized Compton scatterings in the plastic scintillators, the energy resolution would be lost. The detection efficiency would be rather low compared to BGO systems.

Wong proposed staggered layers of BGO, GSO and BaF_2 coupled to PMTs [5]. Bartzakos et al. proposed a detector composed of BGO having a band and two PMTs [6]. The former technique would determine the DOI information by 1/2 or 1/3 of the total depth, but would require a more complicated coding scheme, particularly for a multi-ring system. The

latter technique is simpler than the former one, but it is difficult to form a system having three or more detector rings.

Carrier et al. proposed the use of layers of tilted BGO and GSO scintillators coupled to silicon avalanche photodiodes (APD) [7]. Derenzo et al. developed a position-sensitive silicon photodiode and BGO (SPD/BGO) detector [8]. In this scheme the position-sensitivity is achieved by dividing the rectangular area along the diagonal to form two triangular segments. The use of solid state detectors for PET is an attractive way because of their many potential advantages over PMTs. The performance of the state of the art APD/BGO detectors, however, is still marginal for practical use in PET. In particular, their timing resolution is poorer than that of PMT/BGO detectors. In the use of the solid state detectors, temperature control is necessary. APDs require temperature stabilization in order to be operated at a constant gain, and SPDs require cooling for the reduction of noise. Implementation of temperature controllers into PET would make the system design more complicated, and it is not desirable from an engineering point of view.

5.2 Construction of 3D Detector Having Pillar BGO Bundle

Figure 5-2 shows the schematic drawing of a detector designed to provide three-dimensional (3D) position information of γ-ray interactions in the detector [9]. Pillar shaped BGO elements are bundled up and coupled to two position-sensitive PMTs at their both ends. The schematic diagram of the detector read-out is shown in Fig.5-3. The positions of γ-ray interactions in the crystals in the tangential direction (X) and the radial or depth direction (Y) are independently calculated from the crossed-wire anode outputs of the both PMTs. The positions in the axial direction (Z) are calculated by comparing one PMT dynode output to the other. The dynode signals of both PMTs are summed up in an adder, and led to timing and energy discriminators.

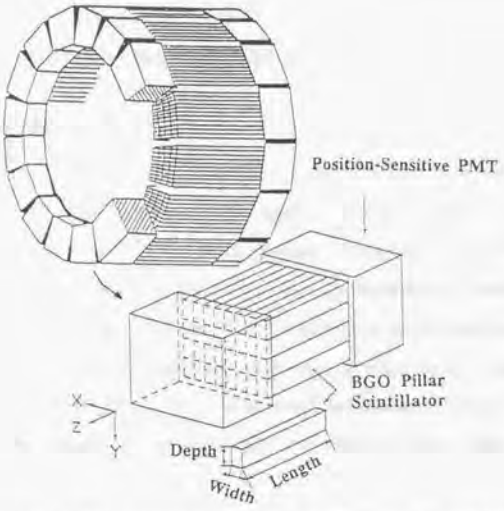

Fig.5-2 Construction of 3D detector having pillar BGO crystals and PS-PMTs

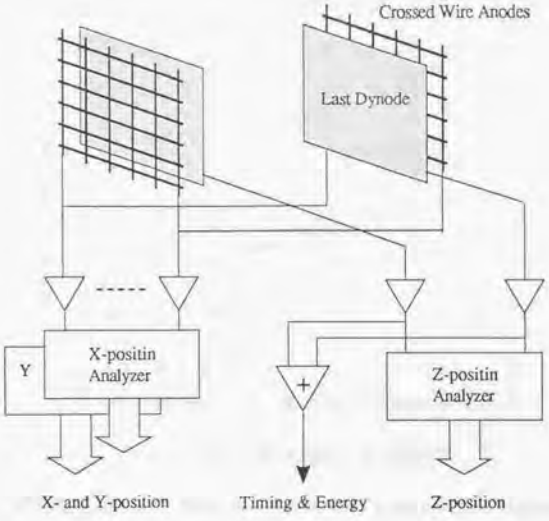

Fig.5-3 Schematic diagram of detector readout

5.3 Simulation Studies on Spatial Resolution

5.3.1 Resolution in the X and Y Directions

A simulation study was performed to estimate the spatial resolution with the BGO bundle detector. A Monte Carlo code written for this application tracks the Compton and the photoelectric interactions of γ-rays in the BGO crystals. Coincidence response functions (CRF) with both a conventional detector without DOI and the proposed 3D detector with DOI were calculated for different incident angles of γ-rays, where the conventional detector uses 20 mm deep crystals, and the 3D detector uses four layers (row) of 5 mm deep crystals. Figure 5-4 shows the FWHM values of CRFs of the conventional detector as a function of the γ-ray incident angle, where the calculation was performed with detectors using different widths of BGO crystals.

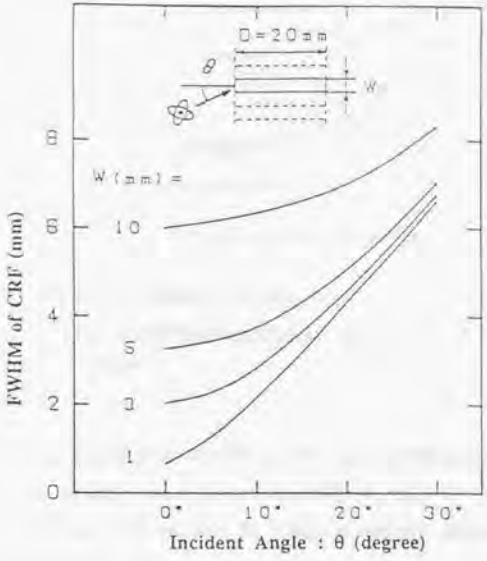

Fig.5-4 FWHM values of CRFs as a function of γ-ray incident angles calculated with detectors (no DOI) having various depths of BGO crystals

The FWHM values of CRFs calculated with different widths of BGO crystals at different rows in the 3D detector are shown in Fig. 5-5. The spatial resolution for deep-interaction of γ-rays is slightly poorer than that for shallow-interaction of γ-rays, because a fraction of γ-rays are scattered in the upper segments and spread towards the lower segments.

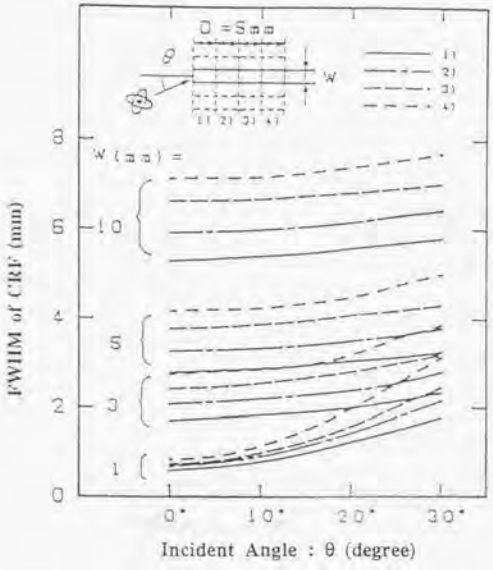

Fig.5-5 FWHM values of CRFs as a function of γ-ray incident angles calculated with 3D detector (DOI) having different widths of BGO piles (each layer is 5 mm in depth)

Figure 5-6 shows a comparison of CRF profiles between the conventional detector and the 3D detector, both of which have 3 mm wide BGO crystals. It was found that the 3D detector offers better spatial resolution for γ-rays at oblique incident angles than the conventional detector because of the use of DOI information.

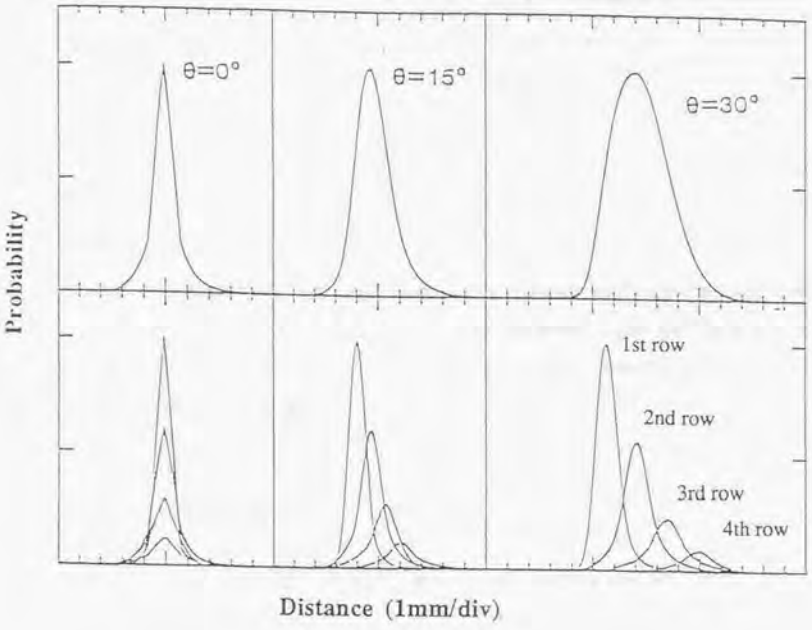

Fig.5-6 Comparison of CRF profiles between detector having no DOI capability and 3D detector providing DOI information
(The width of the BGO segments is 3.0 mm for both detectors)

5.3.2 Resolution in the Axial (Z) Direction

To obtain a good spatial resolution in the axial (Z) direction, the light response function (LRF) of a pillar BGO was studied; LRF is defined as the light output response at each end of an element as a function of incident γ-ray positions along the pillar (Z direction).

When a maximum likelihood position estimation is applied, a minimum resolution (R_{min}) for given LRFs is derived as follows: [10]

$$R_{min} = 1/\left[\left\{\frac{df_1(z)}{dz}\right\}^2 / f_1(z) + \left\{\frac{df_2(z)}{dz}\right\}^2 / f_2(z)\right], \qquad (5\text{-}2\text{-}1)$$

where $f_1(z)$ and $f_2(z)$ are the output from each end of a BGO pillar. LRFs are optimized when the following criteria are simultaneously satisfied: both the energy signal and the minimum resolution should be independent of incident γ-ray positions. Both criteria for optimization are satisfied, if $f_1(z)$ and $f_2(z)$ are given by

$$f_1(z) = k \sin^2 az$$
$$f_2(z) = k \cos^2 az \ , \qquad (5\text{-}2\text{-}2)$$

where $a = \pi / (2L)$ (L: pillar length), z is scintillation position, and k is a constant [11].

5.4 Experimental Studies

State-of-the-art BGO crystals have excellent transparency so that the scintillation light propagates in the BGO pillar in the similar manner as in an optical fiber. The LRF of a BGO pillar having mirror polished surfaces is rather flat as shown in Fig.5-7 (case a), and thus providing little information for the positions of γ-ray incidence. We found that the slope of the LRF could be changed by coarsely grinding the side surfaces of a pillar. We examined the LRF of BGO pillars with different patterns of ground surfaces as shown in Fig.5-7. Although the optimum LRF was hardly realized with a BGO pillar, parabolic shape of LRFs could be obtained with some BGO pillars having particular patterns of ground surfaces; parabolic LRFs also satisfy the criterion for constant resolution but not for constant energy.

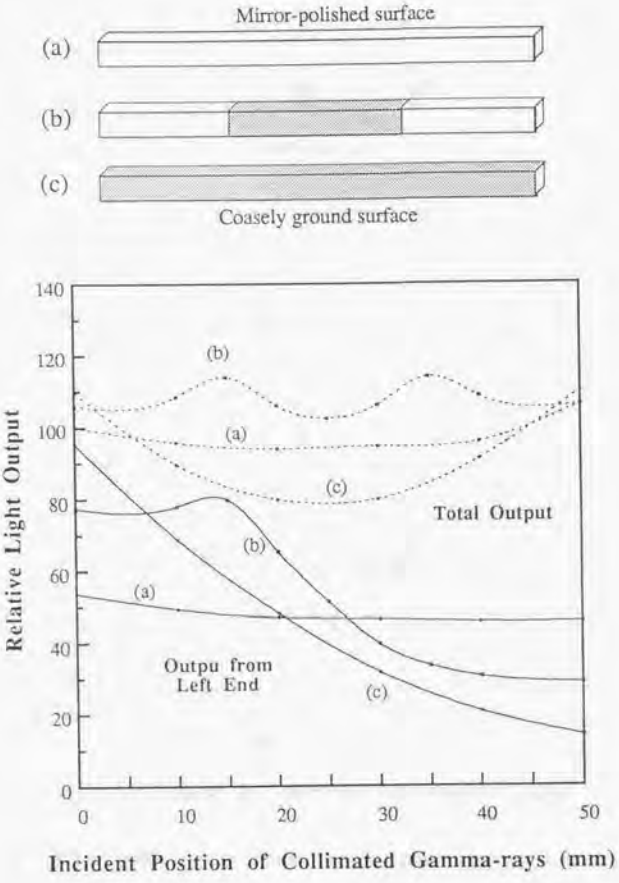

Fig.5-7 Light responses for BGO pillars having different surface conditions

As an interesting result, a BGO pillar with striped ground surfaces provides a stair-shaped LRF as shown in Fig.5-8. It is applicable to a conventional multi-ring configuration, in which slice collimators be set on the ground portion of BGO pillars.

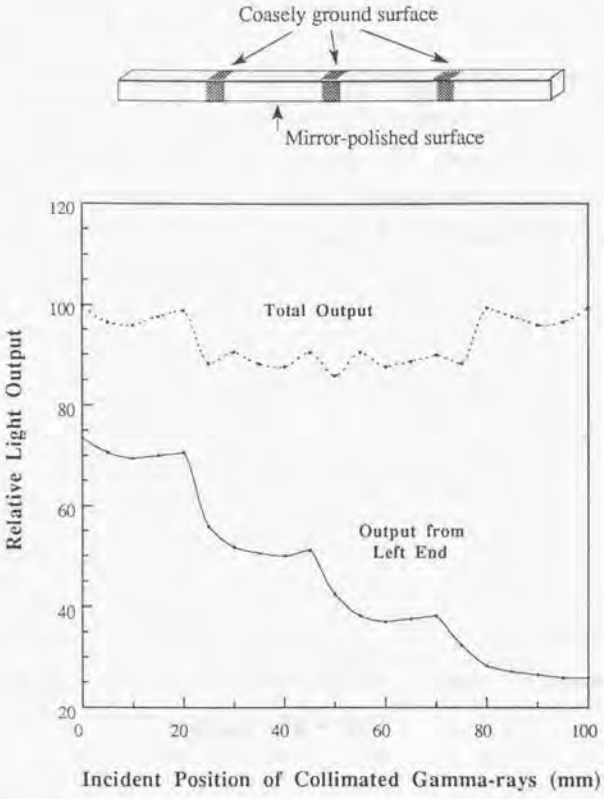

Fig.5-8 Stair-shaped light response obtained with a pillar having zebra-pattern of ground surfaces

We made a bundle of BGO pillars having four rows in the Y direction and eight columns in X direction; forming an 8 (X) x 4 (Y) pillar matrix. Each BGO pillar had a dimension of 3 mm width (X) x 5 mm depth (Y) x 50 mm length (Z). The 32 BGO pillars were coupled to two 76 mm square PS-PMTs (Hamamatsu R2487), where the BGO pillars were held in an aluminum case having a grid cross section. The crystal pitches in this arrangement are 3.75

mm in X and 7 mm in Y. The whole area of the side surfaces of each crystal was coarsely ground, of which the LRF is shown in Fig. 5-7 (case c).

The detector response function (DRF) with each BGO pillar was measured by scanning a collimated source in the directions inclined to X by 0°, 15° and 30°. The CRF with each BGO row was calculated for the measured DRF. Typical CRF profiles and their FWHM values with each BGO row at different incident angles are summarized in Fig.5-9. (The DRF and CRF profiles of all segments at γ-ray incident angles of 0°, 15° and 30° are shown in Figures 5-10 to 5-12.)

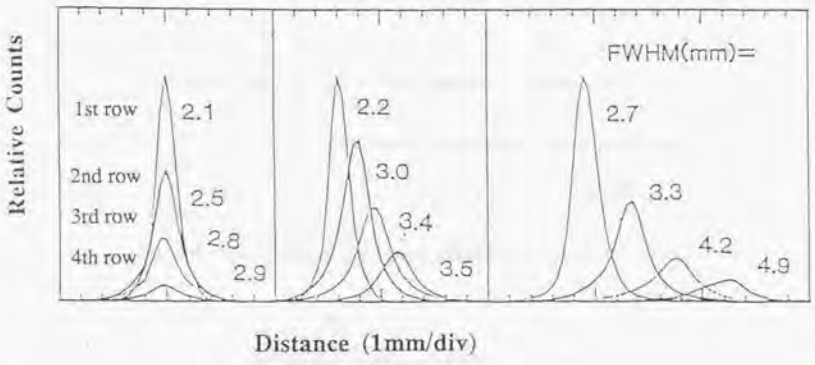

Fig.5-9 Typical CRF profiles with each BGO row measured at different γ-ray incident angles

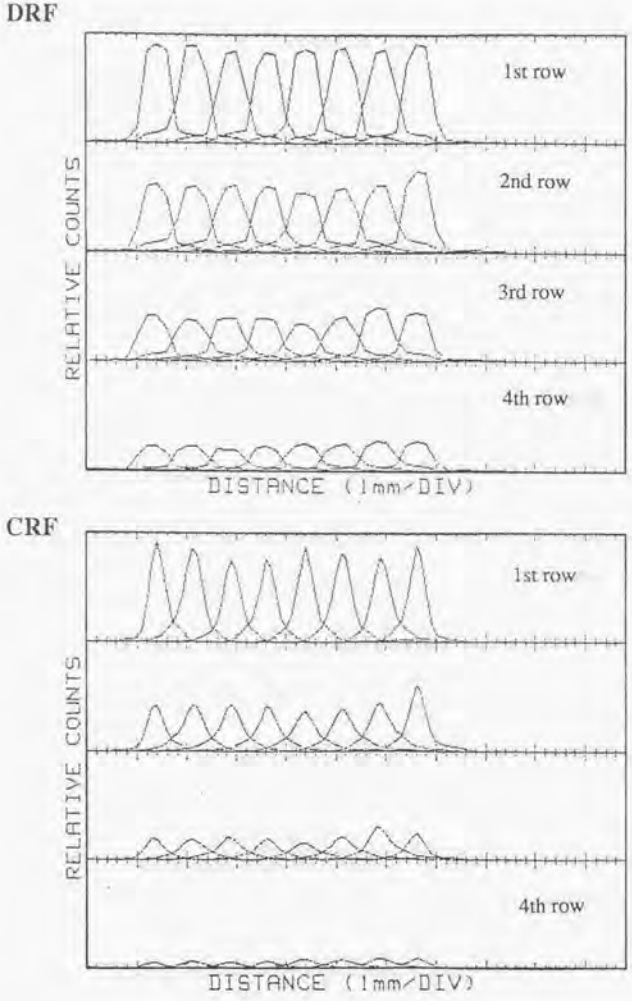

Fig.5-10 DRF and CRF profiles of 3D detector at γ-ray incident angle of 0°

Upper figures: DRFs measured by scanning 0.5 mm collimated γ-rays

Lower figures: CRFs calculated using above DRFs

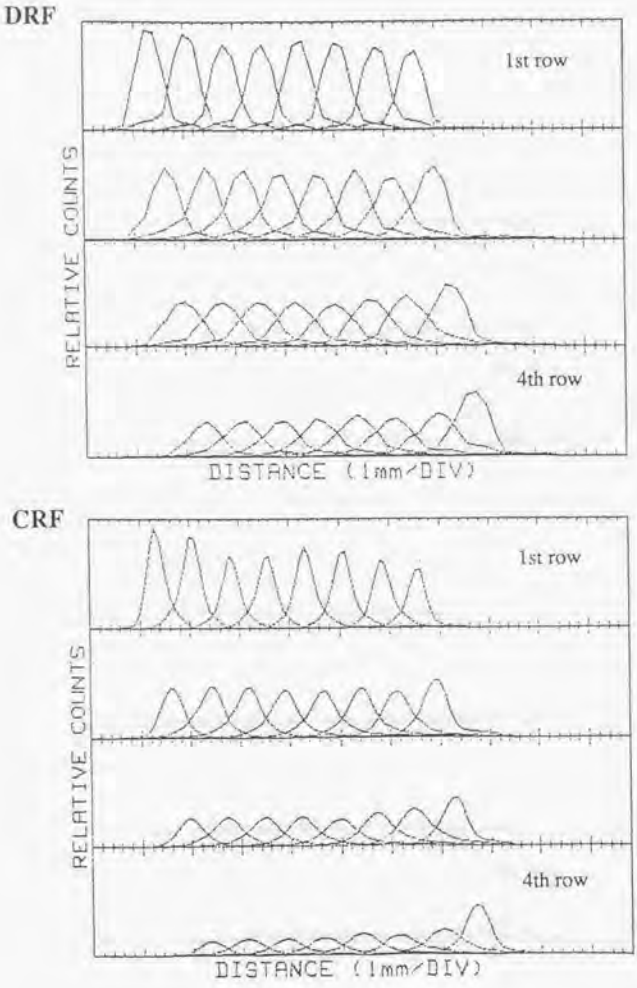

Fig.5-11 DRF and CRF profiles of 3D detector at γ-ray incident angle of 15°

Upper figures: DRFs measured by scanning 0.5 mm collimated γ-rays

Lower figures: CRFs calculated using above DRFs

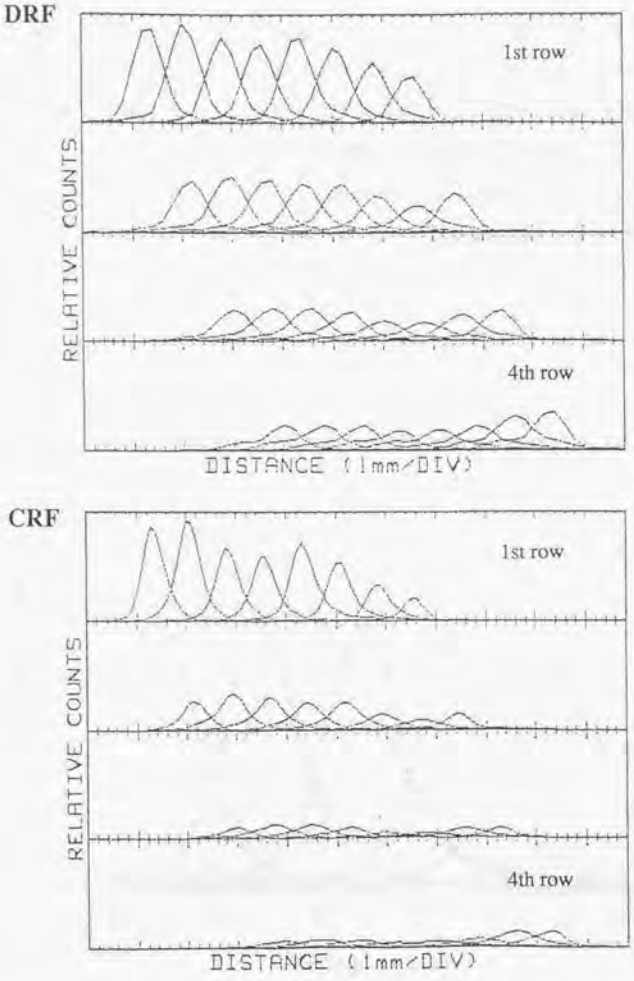

Fig.5-12 DRF and CRF profiles of 3D detector at γ-ray incident angle of 30°

Upper figures: DRFs measured by scanning 0.5 mm collimated γ-rays

Lower figures: CRFs calculated using above DRFs

We measured the detector response in Z direction for collimated γ-rays. The position in Z direction was obtained by adopting a maximum likelihood position estimation to each PMT output signal through A/D converters. Figure 5-13 shows the line spread functions measured for different positions of γ-ray irradiation, where the distance between the irradiation positions was 10 mm. A resolution of approximately 9.5 mm FWHM was obtained at each position.

The time resolution of the detector in coincidence with a BaF_2 detector was measured to be 5.3 ns FWHM, where two 50 mm diameter PS-PMTs (Hamamatsu R2486) were used coupled to the BGO bundle.

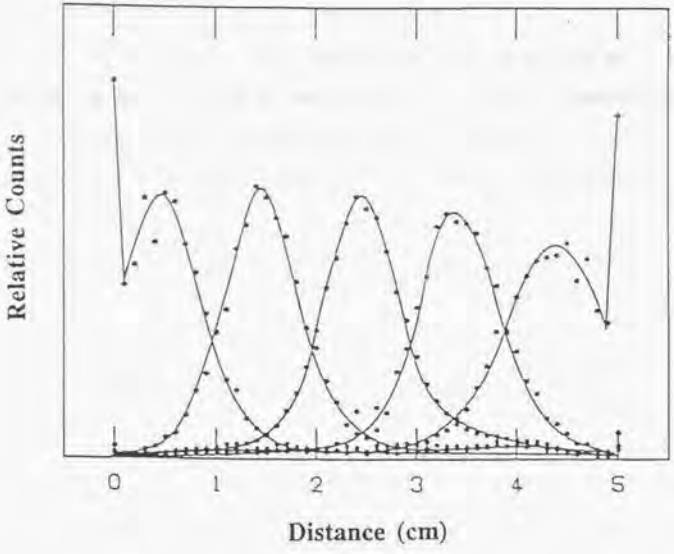

Fig.5-13 Line spread functions for collimated γ-rays in the axial (Z) direction

5.5 Discussion

The CRFs obtained on the basis of the experiment were broader than those expected from the simulation study. Since we used aluminum spacers between BGO pillars to hold them at their exact positions in the experimental setup, an effect of scattered γ-rays on the detector resolution was more dominant in the experiment, particularly with deeper BGO rows. It will be improved by packing the BGO pillars closely. The crystal separation capability of the PS-PMTs is another factor affecting the detector spatial resolution in the X and Y directions. The resolution in the axial (Z) direction is inversely proportional to the square root of the number of photoelectrons per event in the PMTs. Better timing and spatial resolution of the detector can be expected with an improvement of PMT performance characteristics such as photocathode sensitivity and photoelectron collection efficiency.

If BGO pillars are piled up with a spatial shift of a half pitch in the X-direction alternatively and the depth of each BGO row is designed to provide equal detection efficiency, which was proposed by Wong [5], they will be applicable to a stationary PET system because of increasing sampling density and uniform detection efficiency among the segments.

References

(1) R.H. Huesman, E.M. Salmeron and J.R. Baker, "Compensation for crystal penetration in high resolution positron tomography," *IEEE Trans. Nucl. Sci.*, vol.36, pp.1100-1107

(2) J.S. Karp and M. Daube-Witherspoon, "Depth-of-interaction determination in NaI(Tl) and BGO scintillation crystals using a temperature gradient," *Nucl. Instr. Meth.*, vol.260, pp.509-517, 1987

(3) J.G. Rogers, D.P.Saylor, R. Harrop et al., "Design of an efficient position sensitive gamma ray detector for nuclear medicine," *Phys. Med. Biol.*, vol.31, pp.1061-1090, 1986

(4) J.A. McIntyre, R.L. Spross and K.H. Wang, "Construction of a positron emission tomograph with 2.4 mm detectors," *IEEE Trans. Nucl. Sci.*, vol.33, pp.425-427

(5) W.H. Wong, "Designing a stratified detection system for PET cameras," *IEEE Trans. Nucl. Sci.*, vol.33, pp.591-596, 1986

(6) P. Bartzakos and C.J. Thompson, "A depth-encoded PET detector," *IEEE Trans. Nucl. Sci.*, vol.38, pp.732-738, 1991

(7) C.Carrier, C. Martel, D. Schumitt et al., "Design of a high resolution positron emission tomograph using solid state scintillation detectors," *IEEE Trans. Nucl. Sci.*, vol.35, pp.685-690, 1998

(8) S.E. Derenzo, W.W. Moses, H.G. Jackson et al., "Initial characterization of a position-sensitive photodiode/BGO detector for PET," *IEEE Trans. Nucl. Sci.*, vol.36, pp.1084-1089, 1989

(9) K. Shimizu, T. Ohmura, M. Watanabe et al., "Development of 3-D detector system for positron CT," *IEEE Trans. Nucl. Sci.*, vol.35, pp.717-720, 1988

(10) H.L. Van Trees, *"Detection, estimation and modulation theory,"* John Wiley and Sons Inc., New York

(11) T.D. Milster, L.A. Selberg, H.H. Barrett et al., "A modular scintillation camera for use in nuclear medicine," *IEEE Trans. Nucl. Sci.*, vol.31, pp.578-580, 1984

Chapter 6

Comb-Slit BGO Detector Providing Single Bit of Depth Information

In this chapter, a block detector with a single bit of depth of interaction information is demonstrated, which consists of a PS-PMT and a block BGO crystal having comb-shaped slits in it. The proposed detector efficiently utilizes the high spatial resolution capability of the PS-PMT. The experimental results have proven their usefulness in PET applications. Since the detector has a relatively simple structure and does not require particular read-out electronics, it can be applied to the existing animal PET system.

6.1 Structure and Principle of Comb-Slit BGO Block Detector

A block detector composed of a PS-PMT and BGO blocks having comb-shape slits is proposed to improve the resolution uniformity of a PET system [1]. Figure 6-1 shows the structure of the detector. The BGO block has slits both in the upper and lower half portions, where the positions of the upper slits shift by a half of each slit pitch from those of the lower slits.

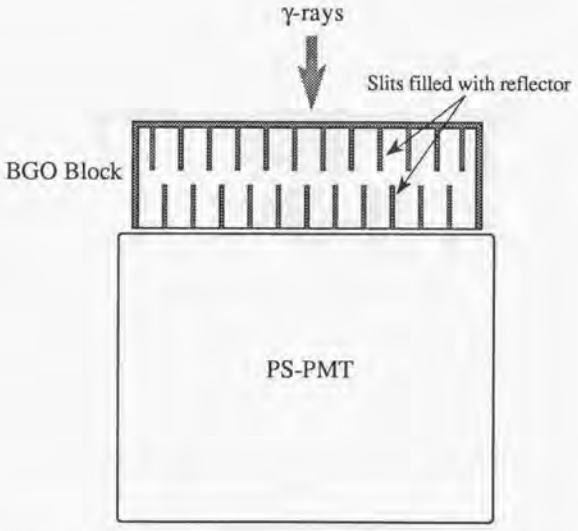

Fig.6-1 Schematic drawing of comb-slit BGO block detector

Figure 6-2 shows the principle of position and depth detection in the comb-slit BGO block detector. When an incident γ-ray is absorbed in the upper portion of the block, the scintillation photons propagate towards the lower portion and are divided into two lower segments. Thus the centroid of the output light distribution is located in the middle of the two lower segments, which corresponds to the position of the upper segment in which the γ-ray is

absorbed. On the other hand, if a γ-ray interacts with a segment in the lower portion, the scintillation light output is mostly from the one lower segment. Consequently, the centroid of the output light distribution corresponding to the γ-ray interactions in the upper and lower portions should shift by a half of the slit pitch (d). Thus, if the position discriminator windows are properly set on a position map obtained by a centroid calculation, a single bit of depth information of the γ-ray interaction can be derived as well as the position information used for the segment identification.

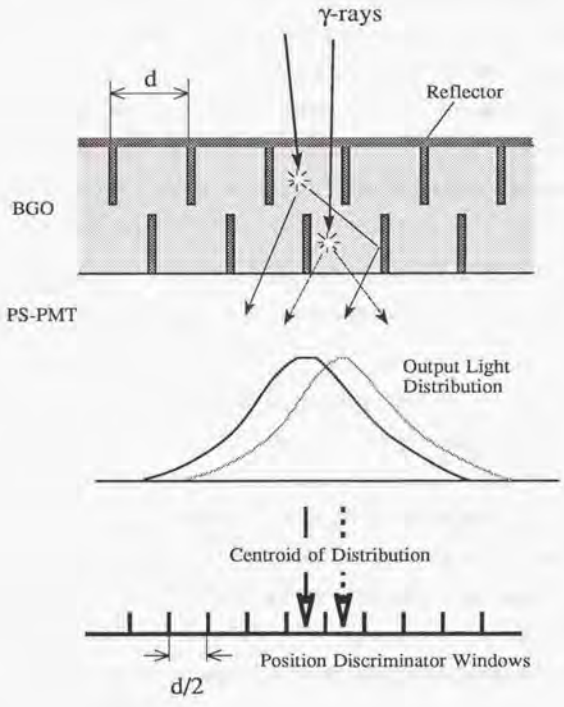

Fig.6-2 Principle of depth-of-interaction detection with comb-slit BGO detector

6.2 Effect of Slit Depth

If there is a large space between the bottom of the upper slits and the top of the lower slits, scintillation photons spread over multiple segments, where the gap space works as a light guide. A test sample of a 20 mm deep BGO block having different depths of slits in it was made to investigate the effect of the space between the upper and lower segments on the crystal separation capability. The gap distances between the upper and the lower slits in the BGO block were 1 mm, 2 mm and 3 mm. The peak to valley ratio (P/V) of the segment profile on the position map was measured with the upper and the lower segments separately. The mean P/V values were 4.4, 3.7 and 2.1 for 1 mm, 2 mm and 3 mm gap distances, respectively. As the gap becomes larger, the spatial resolution degrades because of increasing light distribution spread. Although a narrower gap between the upper and lower slits provides better performance, a gap distance of at least 1 mm is necessary to keep a reasonable mechanical strength with a comb-slit BGO block.

It is desirable that the upper and the lower portions have an equal detection efficiency for 511 keV γ-rays [2]. Thus, the depth of the upper and the lower slits should be designed to provide an equal detection efficiency.

In consideration of conditions above, we fabricated a comb-slit BGO as a trial-manufacturing as shown in Fig.6-3. The block is 60 mm x 10 mm x 20 mm in size and has comb-shape slits in it, where the depth of the upper slits is 6.6 mm and that of the lower slits is 12.4 mm. The block has 33 segments, 17 upper segments and 16 lower segments, each which is 3.25 mm in width and 3.75 mm in pitch except two upper segments at the both ends. We also made a block composed of 3.75 mm pitch of 10 discrete BGO segments to compare its performance with that of the comb-slit BGO. The segment size of the discrete BGO array is 3.25 x 10 mm^2 cross section by 20 mm depth. Both BGO blocks were measured coupled to a PS-PMT, Hamamatsu R3941-02.

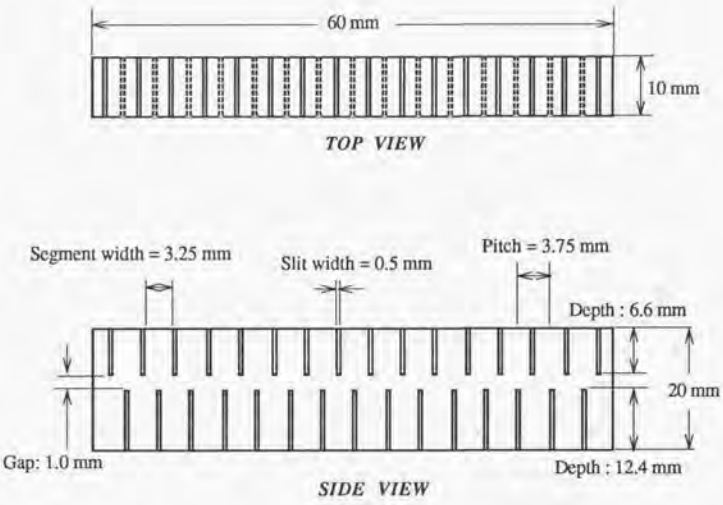

Fig.6-3 Dimensions of comb-slit BGO used for the experiment

6.3 Detector Resolution for Different Angles of γ-ray Incidence

To determine the position discriminator windows, the detector was irradiated by γ-rays with full BGO block illumination. Peaks corresponding to each BGO segment were clearly seen in the position map with the discrete BGO block, but not with the comb-slit BGO block. In order to find the positions of peaks and valleys for the comb-slit BGO, either upper or lower segments of the BGO block were irradiated at their sides with slit collimated γ-rays. Their profiles on the position map are shown in Fig.6-4. With properly setting the position discriminator windows, i.e. setting them as each window includes only one peak corresponding to either an upper segment or a lower segment, we measured the detector response functions (DRFs) using a scanning collimated source at different incidence angles of

0°, 7.5°, 15°, 22.5° and 30°. To eliminate the edge effect on this study, we used the data with 25 segments in the central part of the BGO block, 13 upper segments and 12 lower segments, for the performance evaluation.

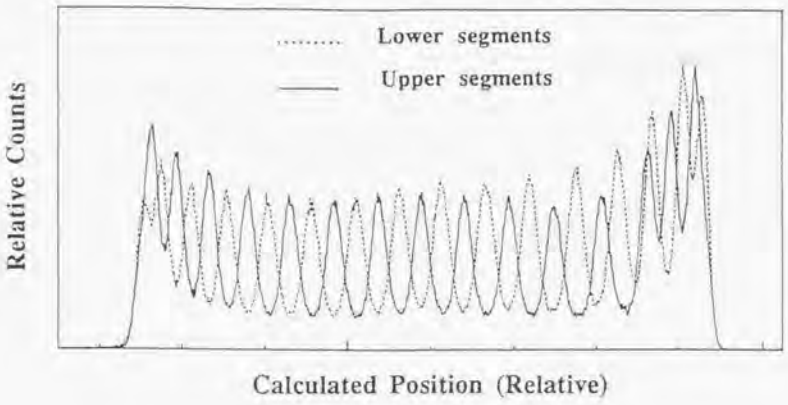

Fig.6-4 Image profiles for γ-ray irradiation on upper and lower segments (The profiles with the upper segments and those with the lower segments were measured separately.)

The DRF profiles with the central segments at an incident angle of 0° are shown in Fig.6-5. Since the width and shape of the DRFs are different with the upper and lower segments, there are three kinds of combinations to calculate the CRFs, upper segment versus upper segment (U-U), upper segment versus lower segment (U-L) and lower segment versus lower segment (L-L). The CRF profiles for the U-L combination at γ-ray incident angles of 0°, 14.5° and 30° are shown in Fig.6-6.

The FWHM and FWTM values of CRFs were calculated with those three combinations for the comb-slit BGO detector. Table 6-I shows the FWHM and FWTM values of CRFs with the discrete BGO array detector and the comb-slit BGO block detector.

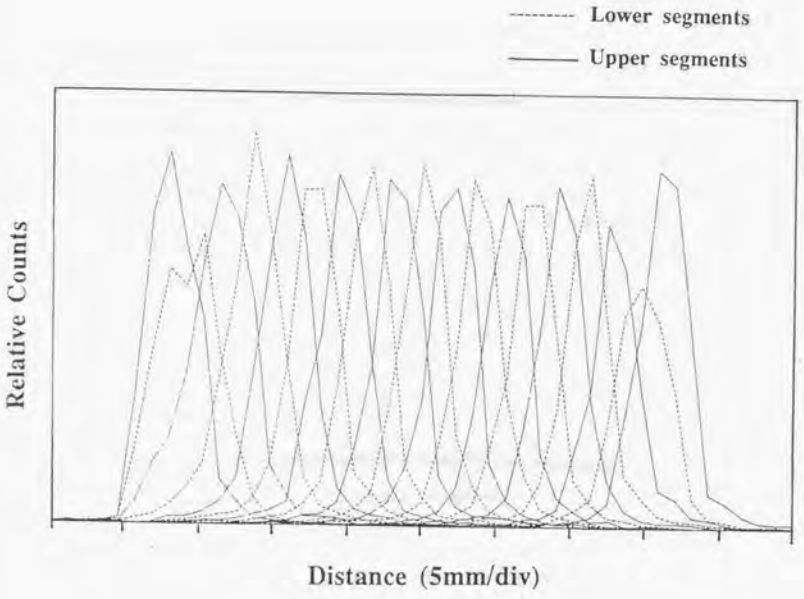

Fig.6-5 DRF profiles measured for comb-slit BGO detector

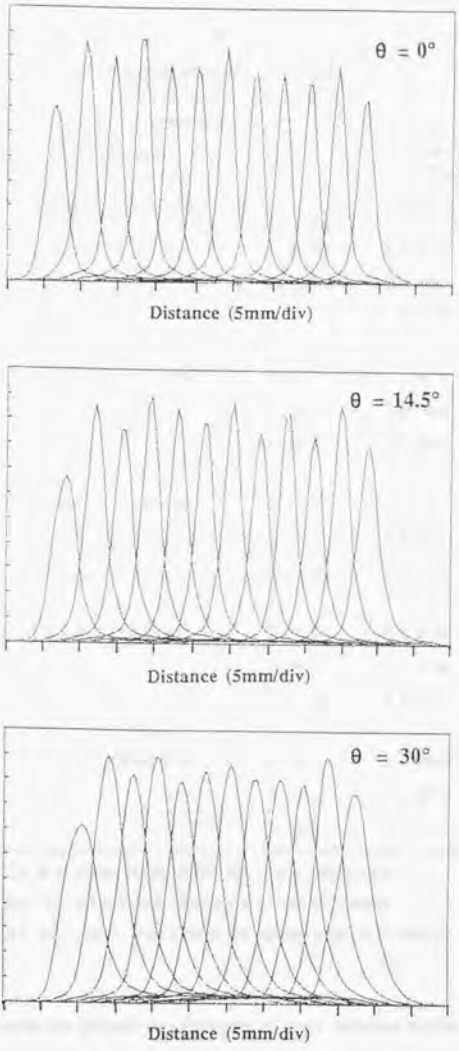

Fig.6-6 CRF profiles for different incidence angles of γ-rays calculated from DRFs of comb-slit BGO detector

Table 6-I FWHM and FWTM values of CRFs at different angles of γ-ray incidence with discrete BGO detector and comb-slit BGO detector

Incident Angle	Discrete BGO (3.25 mm wide)			Comb-slit BGO (3.25 mm wide)	
	FWHM	FWTM		FWHM	FWTM
$\theta = 0°$	2.1 mm	5.3 mm	U vs U	2.4 mm	5.4 mm
			L vs L	2.3 mm	5.6 mm
			U vs L	2.4 mm	5.5 mm
$\theta = 7.2°$	2.4 mm	5.6 mm	U vs U	2.5 mm	5.8 mm
			L vs L	2.6 mm	6.0 mm
			U vs L	2.5 mm	6.0 mm
$\theta = 14.5°$	3.1 mm	6.6 mm	U vs U	2.7 mm	6.4 mm
			L vs L	3.2 mm	7.1 mm
			U vs L	2.8 mm	7.0 mm
$\theta = 22°$	4.3 mm	8.3 mm	U vs U	3.1 mm	7.6 mm
			L vs L	4.0 mm	8.5 mm
			U vs L	3.5 mm	8.4 mm
$\theta = 30°$	5.6 mm	10.2 mm	U vs U	3.7 mm	8.9 mm
			L vs L	5.2 mm	10.5 mm
			U vs L	4.5 mm	10.2 mm

U vs U: CRF calculated with DRFs for upper segments
L vs L: CRF calculated with DRFs for lower segments
U vs L: CRF calculated with DRFs for upper segments versus lower segments

Their FWHM values are plotted as a function of γ-ray incident angles as shown in Fig.6-7. The discrete BGO array detector provides better resolution at normal incidence, and on the contrary the comb-slit BGO detector provides better resolution for large angles of γ-ray

incidence. Thus an improvement in resolution uniformity is expected with a PET using the comb-slit BGO detector.

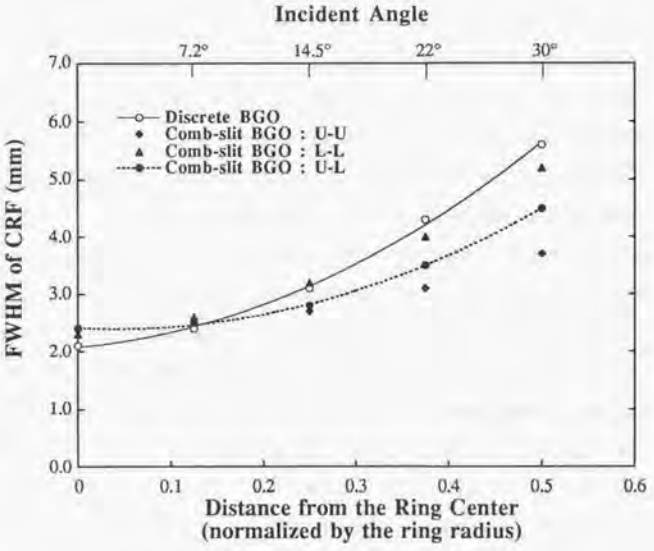

Fig.6-7 Comparison of FWHM of CRFs between discrete BGO detector and comb-slit BGO detector at different distance from the center corresponding to γ-ray incident angles

A ratio of the detection efficiency between the upper and the lower segments were calculated by integrating the counts in their DRFs at different incident angles of γ-rays. The ratio (upper / lower) was 1.02, 1.05 and 1.07 for the angles of γ-ray incidence at 0°, 14.5° and 30°, respectively. It was found that almost equal detection efficiency was obtained with the upper and the lower segments, as expected in the design of the slit depth; 6.6 mm for the upper slits and 12.4 mm for the lower slits.

6.4 Discussion

The block detector having comb-slit BGOs has a potential capability to provide a PET system with uniform resolution in the field of view because of its ability to provide high resolution and a single bit of depth information. Our experiments with prototype detectors confirmed the efficacy and applicability of the comb-slit block BGO detector for PET. The ability to provide the depth information strongly depends on the resolution capability of the detector. If the peak-to-valley ratio on the position map slightly degrades, the depth information is lost to a large extent. This is because the width of the position discriminator windows with the comb-slit BGO detector is a half of that with a discrete BGO array detector having the same segment width, and it causes the crosstalk from the adjacent channels corresponding to the opposite portion (upper or lower). Thus the PS-PMT used for this application is specifically required to have a high spatial resolution capability. The gap space between the upper and the lower segments is desired to be as small as possible. If we find good reflector materials having a thermal expansion coefficient similar to that of BGO to fill the slits with, the comb-slit BGO having small gaps will be fabricated. The surfaces in the slits are not smooth because of no post-process after cutting the slits. The light output can be improved by making slits having smooth wall surfaces, which may be possible through application of a chemical etching process after cutting the slits in the block.

If the refractive index of the scintillator is close to that of an optical coupling compound, we can use two or three layers of stacked scintillators in the same manner as the comb-slit BGO scheme. This is the case for BaF_2 scintillators, while the refractive index of BGO is 2.15. (Most optical coupling compounds have a refractive index of 1.47.).

The other interesting trial is detecting the spatial spread of light output [3]. In the comb-slit BGO, the light spread due to γ-ray interaction in the upper portion should be broader than that in the lower portion. Thus the detection of light spread from the comb-slit BGO will provide a single bit depth information of γ-ray interaction. We have not yet evaluated this method and a further investigation is necessary.

References

(1) T. Yamashita, M. Watanabe, K. Shimizu et al., "High resolution block detectors for PET," *IEEE Trans. Nucl. Sci.*, vol.37, pp.589-593, 1990

(2) W.H. Wong, "Designing a stratified detection system for PET cameras," *IEEE Trans. Nucl. Sci.*, vol.33, pp.591-596, 1986

(3) J.G. Rogers, D.P.Saylor, R. Harrop et al., "Design of an efficient position sensitive gamma ray detector for nuclear medicine," *Phys. Med. Biol.*, vol.31, pp.1061-1090, 1986

Chapter 7

Summary and Future Work

In this chapter, we summarize the results of this research and what this work has contributed to the field of PET system development and the research using it, and discuss a future prospect with PET and detectors. There exist many interesting subjects that require future work.

7.1 Summary

Positron Emission Tomography (PET) has been used as a research tool to obtain functional images of the human body, and today, there is a demand to use it as a diagnostic tool in various clinical fields and also as a research tool for basic studies using experimental animals. Improvement of PET performance has been a consistent requirement for better imaging and quantification capability.

In this thesis, we have proposed new detectors for PET, which use position-sensitive photomultiplier tubes (PS-PMTs) and fine segments BGO arrays. Further development of the detector has resulted in the proposal of two types of PET detectors providing depth information of γ-ray interaction in the crystals. The goal of this study is the development of PET detectors for a practical use in PET systems. We have demonstrated the usefulness of the new detector by applying it to an animal PET system. It was proven that a high resolution PET could be constructed by applying the new detector scheme.

The main results of this research are summarized as follows:

- New detector schemes using PS-PMT have been proposed and investigated.
- The optimum design of BGO detector for PET has been investigated on the basis of an analysis on scintillation photons with BGO crystals.
- Various apparatus to accurately measure the performance characteristics of PET detectors have been developed.
- Characteristics of BGO detectors have been studied, which include the time resolution and the spatial resolution.
- An intrinsic detector resolution in coincidence of less than 2 mm was achieved with fine BGO crystals coupled to the PS-PMT, which is close to the physical limit of PET resolution.
- A high resolution PET dedicated to animal studies has been developed by applying the new detector, and a spatial resolution of 3.0 mm was obtained with this system.

- Two types of new detectors utilizing depth information of γ-rays have been proposed, and the usefulness of their applications to PET has been proven by preliminary experiments.

The research contained in this thesis, in particular, has contributed to basic research using experimental animals by offering researchers an in-vivo imaging tool; a high resolution PET dedicated to animal studies. Up to the present, five animal PET systems have been installed in research facilities in Japan, and advanced research using them is now being performed.

7.2 Areas of Future Investigation

7.2.1. Detectors for 3D PET

Currently, there is an increasing interest in PET systems providing data suitable for three dimensional (3D) volumetric imaging. Most of the present PET designs use interplane septa between the detector rings, and eliminate coincidence lines-of-response between pairs of detectors more than one ring apart. The circular interplane septa reduce the scattered and accidental coincidence noise at the cost of sensitivity for true coincidence events. The PET systems using the interplane septa utilize only about 0.5 % - 1 % of the total events emitted isotropically from the source of activity. The sensitivity (S) of PET using interplane septa is geometrically given by the following equation:

$$S = k\, R^2 / D\ , \qquad (7\text{-}2\text{-}1)$$

where R is the axial resolution (determined by the slice thickness) , D is the detector ring diameter, and k is a geometrical factor including detector packing fraction and the detection efficiency of the scintillators. If we plot measured sensitivity reported with the existing PET systems versus the geometrical sensitivity calculated by eq.7-2-1, a close correlation between them can be seen as shown in Fig.7-1. This result shows that the slice sensitivity of PET is uniquely determined by the geometrical design of detector rings.

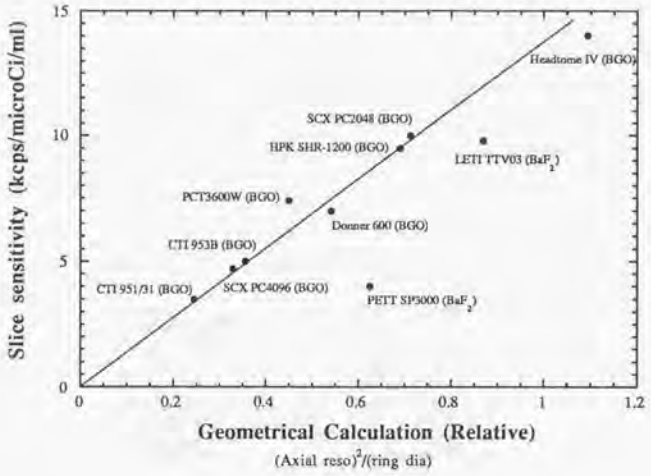

Fig.7-1 Correlation between measured sensitivity and geometrically calculatied sensitivity

A dramatic improvement of the sensitivity is obtained by increasing the axial acceptance angle of detection with the removal of the interplane septa as shown in Fig.7-2. Some pioneering work for 3D PET has been performed by Townsend et al [1]. They retracted the interplane septa in a commercial PET system, and evaluated the performance compared to that of the original design with interplane septa. They reported an improvement in sensitivity due to the removal of the septa of a factor of 5.1, while the the scatter fraction (scatter/true) increased from 12 % to 35 % for the energy threshold at 350 keV, and from 15 % to 48 % at 250 keV.

True three dimensional image reconstruction has been studied by many researchers [2]-[8]. Since the mathematical solution of 3D image reconstruction has already been established, the emphasis of the research is now placed on the development of a practical algorithm applicable to a 3D PET system [7][8]. The effort includes shortening of the calculation time and improvement of image quality by suppression of the statistical noise effect.

Improvements in detector performance are required for 3D PET : The good time resolution of the detector allows the use of narrow coincidence time windows, which results in a reduction of the accidental coincidence rate : The good energy resolution allows accurate setting of energy thresholds for scatter reduction : The reduction of dead time in signal processing extends the maximum count rate capability of the system because the single event rate in 3D PET increases dramatically. Thus the scintillator should have a fast decay time and the detector unit should have a smaller area.

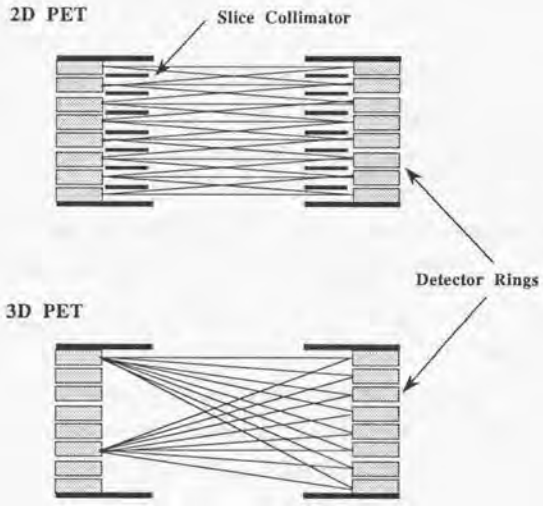

Fig.7-2 Line of responses with 2D PET and 3D PET
(Cross-sectional view in the axial direction)

7.2.2 Detectors for Clinical PET

Since PET has the power to provide unique diagnostic information that is not available with any other imaging modality, clinicians are anticipating the use of PET in clinical fields such as brain and cardiac diagnosis [9]. Each application requires PET to provide different performance capabilities. The complexity of the brain requires significantly high resolution of PET, because a small lesion in a critical location can cause serious problems in the brain. A

PET system designed to produce high quality heart images should have high count rate capability. In cardiac studies, gated imaging capability is required, in which the motion of the heart is minimized and/or measured by synchronizing image collection with the cardiac cycle. In dynamic PET studies, rapid PET imaging of 1 sec to 10 sec per frame may be required. PET is then required specifically to have high sensitivity and high count rate capability. As the use of PET becomes more popular in the clinical fields, systems having special performance characteristics may be designed in accordance with the specific requirements from each clinical field.

In the present diagnostic procedures using PET, it takes several minutes to hours before obtaining the final data for diagnosis. To obtain higher throughput in PET measurement, improvements in system sensitivity and image/data processing time are of major importance, as well as the establishment of protocols for PET measurement. Once PET diagnostic techniques and procedures are established for some diseases, other instrumentation such as simple positron probe systems may be applicable instead of PET [10][11].

Because the isotope production capability of a cyclotron is large enough for several PET systems and probe systems, it is possible to place several satellite PET imaging sites around a cyclotron facility. The other possible way to expand the PET utility is to establish a delivery system of compounds labeled with a relatively long half-life radionuclide (^{18}F) from a cyclotron center, which may be managed by commercial companies.

The cost-effectiveness of the detectors including both scintillators and PMTs is of major concern in clinical applications of PET, especially for a 3D-PET using a large number of the detectors. Better stability and liability will be required to detectors for clinical PET.

7.2.3 Possible Detectors for Future PET

Scintillators having faster decay time and higher light yields than BGO have been investigated by many researchers [12]-[17]. Rare-earth oxyorthosilicates (LSO, GSO, YSO), CeF_3, $PbCO_3$ and other new materials have recently been introduced. Table 7-I shows the performance characteristics of these scintillators reported by investigators [12][13][15][16].

Table 7-I Characteristics of new scintillators compared to BGO characteristics

	BGO	CeF_3	$PbCO_3$	$PbSO_4$	LSO
Density (g/cc)	7.13	6.16	6.6	6.4	7.4
Linear attenuation coefficient for 511 keV γ (1/cm)	0.903	0.42	1.1	1.2	0.88
Relative light yield (%) relative to NaI(Tl)	15	8	1.4	12	75
Scintillation decay time (ns)	300	2 (fast) 31 (slow)	5.6 (fast) 27 (slow)	1.8, 19 95, 425	40
Emission peak wavelength (nm)	480	310 (fast) 340 (slow)	475	335	420
Refractive index	2.15	1.68	1.8 2.08	1.88, 1.82 1.89	1.82
Hygroscopic ?	no	no	no	no	no

Among them, LSO has superior characteristics to BGO; high stopping power for 511 keV γ-rays (as high as that of BGO), 3.5 times better light yield than BGO, and fast decay time of 47 ns [16]. We have measured the time resolution of LSO for a 2.8 x 10 mm^2 cross section by 10 mm depth LSO crystal coupled to a 19 mm diameter fast PMT (Hamamatsu R1668), where a BaF_2 detector was used as a reference probe. Figure 7-3 shows the comparison of the time resolution between an LSO-BaF_2 coincidence pair and a BGO-BaF_2 coincidence pair.

We coupled the small LSO crystal to a PS-PMT (Hamamatsu R3941), and measured the image profile of the crystal for ^{137}Cs γ-rays (662 keV). As shown in Fig.7-4, the uncertainty of the crystal position is 1.0 mm FWHM for LSO, while that of BGO having the same dimension is 2.4 mm FWHM. In spite of these excellent characteristics, LSO will be rarely used as a PET detector because of its extremely high manufacturing cost due to the material cost of Lutetium. These experimental results, however, encourage us to develop new detectors using a PS-PMT which would be coupled to a new possible scintillator in the future.

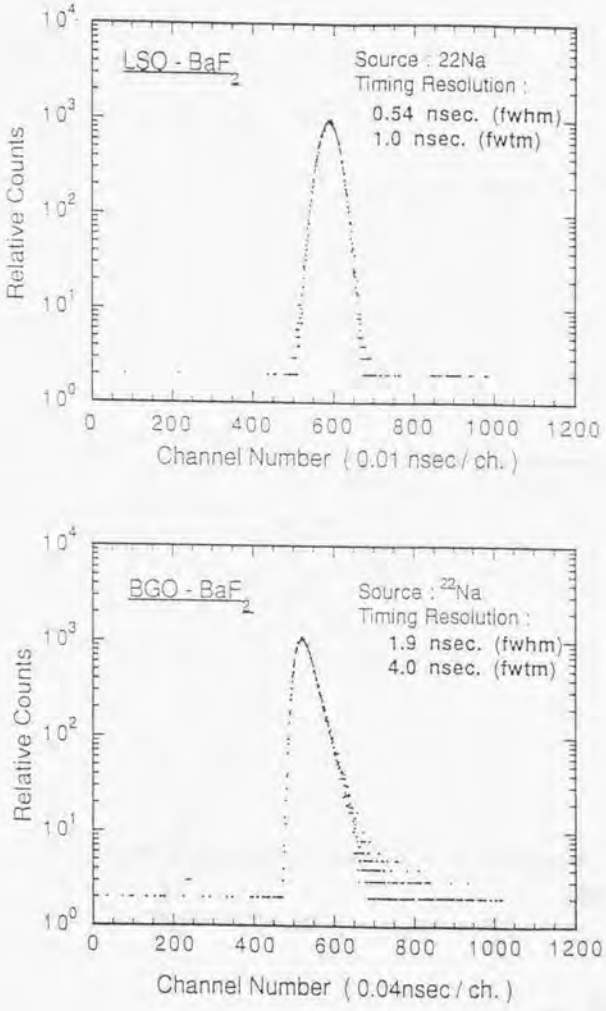

Fig.7-3 Time resolution obtained with BGO-BaF_2 and LSO-BaF_2 detectors

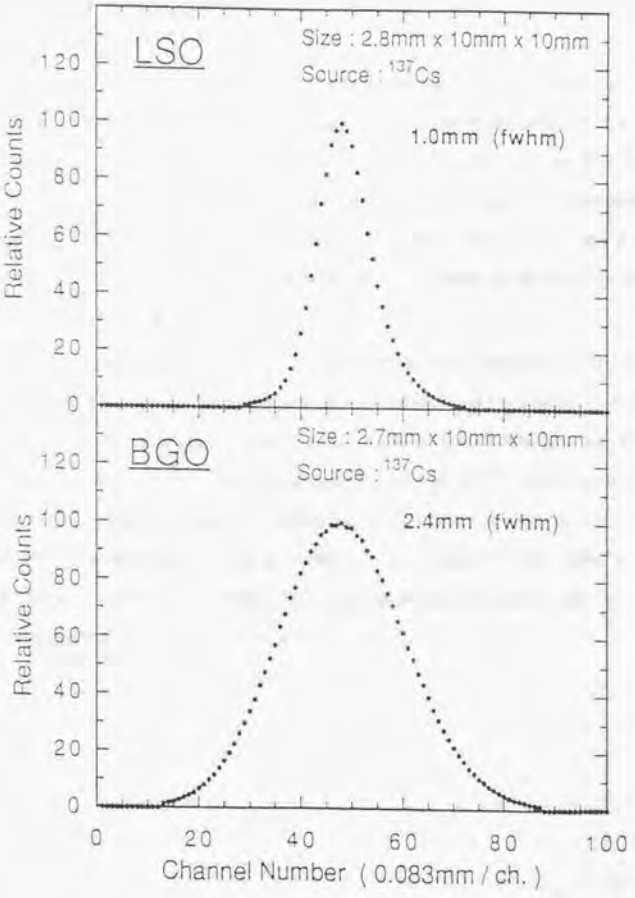

Fig.7-4 Image profiles for BGO and LSO coupled to PS-PMT

The PS-PMT has the capability of high spatial resolution in two dimensions. Desirable improvements of the PS-PMT for a future PET include implementation of a multi-anode, reduction of the unit area, and development of an electron multiplier having better electron collection efficiency and faster timing properties.

Application of a neural network to position calculation of the PS-PMT would be a challenging work in the future. Recently, a fast analog neural network chip (Intel 80170NX) has become available, and has begun to be applied to various fields [18]. A neural network for the PS-PMT readout would offer position estimation near an optimal condition and a capability utilizing multiple events without rejecting them. Since there are still many problems to be solved, further investigations are necessary to develop a detector system using the PS-PMT with a neural network.

An avalanche photodiode (APD) would be another possible detector for a future PET system [19]. The APD array has the advantage of compactness and possible cost reduction through mass production, although it requires a stable temperature controller and low noise amplifiers. Use of solid state detectors for intrinsic detection of 511 keV γ-rays will be a challenging work in the future. High Z materials such as CdTe are possible candidates for PET detectors [20]. The drawback is their poor time resolution due to slow carrier mobility in the bulky detector and high manufacturing cost. Some technology breakthroughs in the future may realize the application of intrinsic γ-ray detectors to PET.

References

1) D.W. Townsend, T. Spinks, T. Jones et al., "Three dimensional reconstruction of PET data from multi-ring camera," *IEEE Trans. Nucl. Sci.*, vol.36, pp.1056-1065, 1989

(2) J.G. Colsher, "Fully three-dimensional positron emission tomography," *Phys. Med. Biol.*, vol.25, pp.103-115, 1980

(3) Z.H. Cho, J.B. Ra and S.K. Hilal, "True three-dimensional reconstruction (TTR) - Application of algorithm toward full utilization of oblique rays," *IEEE Trans. Med. Imag.*, vol.2, pp.6-18, 1983

(4) C.W. Stern, D.A. Chesler and G.L. Brownell, "Three-dimensional image reconstruction in the Fourier domain," *IEEE Trans. Nucl. Sci.*, vol.34, pp.374-378, 1987

(5) J.G. Rogers, R. Harrop, and P.E. Kinahan, "The theory of three-dimensional image reconstruction for PET," *IEEE Trans. Med. Imag.*, vol.6, pp.239-243, 1987

(6) M. Defrise, D.W. Townsend and R. Clack, "Three-dimensional image reconstruction from complete projections," *Phys. Med. Biol.*, vol.34, pp.573-587, 1989

(7) E. Tanaka, S. Mori, K. Shimizu et al., "Moving slice septa and pseudo three-dimensional reconstruction for multi-ring PET," *Phys. Med. Biol.*, vol.37, pp.661-672, 1992

(8) M. Defrise, D.W. Townsend and R. Clack, "Favor: a fast reconstruction algorithm for volume imaging in PET," In *Conference Record of 1992 IEEE Medical Imaging Conference*, vol.2, pp.1919-1923, 1992

(9) H.N. Wagner Jr, "Clinical PET: Its time has come," *J. Nucl. Med.*, vol.32, pp.561-564, 1991

(10) A.N. Bice, H.N. Wagner Jr, J.J. Frost et al., "Simplified detection system for neuroreceptor studies in the human brain," *J. Nucl. Med.*, vol.27, pp.184-191, 1986

(11) M. Yamamoto, N. Nohara, N. Satoh et al., "Time-of-flight positron imaging with eight detectors," In *Proceedings of World Congress on Medical Physics and Biomedical Engineering*, p.406, Kyoto, 1991

(12) S.E. Derenzo, W.W. Moses, T.A. Delvo et al., "Discovery of lead sulfate, a new scintillator for high-rate high-resolution PET," *J. Nucl. Med.*, vol.32, p.995, 1991

(13) W.W. Moses and S.E. Derenzo, "Lead carbonate, a new fast, heavy scintillator," *IEEE Trans. Nucl. Sci.*, vol.37, pp.96-100, 1990

(14) C.L. Melcher, J.S. Schweizer, T. Utsu et al., "Scintillation properties of GSO," *IEEE Trans. Nucl. Sci.*, vol.37, pp.161-164, 1990

(15) D.F. Anderson, "Properties of the high-density scintillator cerium fluoride," *IEEE Trans. Nucl. Sci.*, vol.36, pp.137-140, 1989

(16) C.L. Melcher and J.S. Shweizer, "A promising new scintillator: cerium-doped lutetium oxyorthosilicate," *Nucl. Instr. Meth.*, vol.314, pp.212-214, 1992

(17) P.Lecoq, M. Schussler and M. Schneegans, "Progress and prospects in the development of new scintillators for future high energy physics experiments," *Nucl. Instr. Meth.*, vol.315, pp.337-343, 1992

(18) *Intel Corporation, 80170NX*, "Neural Network Technology & Applications," 1992

(19) R. Lecomte, C. Martel and C. Carrier, "Status of BGO-avalanche photodiode detectors for spectroscopic and timing measurement," *Nucl. Instr. Meth.*, vol.278, pp.585-597, 1989

(20) F. Casali, D. Bollini, P. Chirco et al., "Characterization of small CdTe detector to be used for linear and matrix array," *IEEE Trans. Nucl. Sci.*, vol.39, pp.598-604, 1992

BIBLIOGRAPHY

Subject Relating to PET or Positron Imaging

- **T. Yamashita**, M. Itoh and T. Hayashi., "New dual rectangular photomultiplier tube," In *Proceedings of International Workshop on Physics and Engineering in Medical Imaging, IEEE Comput. Soc.* 82CH1751-7, pp.209-211, Pacific Grove, 1982

- **T. Yamashita** and T. Hayashi, "Photomultiplier tube for TOF tomography," In *Proceedings of Workshop on Time-of-Flight Tomography, IEEE Comput. Soc.* 82CH1791-3, pp.45-49, St.Louis, 1982

- H. Uchida, Y. Yamashita, **T. Yamashita** and T. Hayashi, "Adventageous use of new rectangular photomultiplier tube for positron CT," *IEEE Trans. Nucl. Sci.*, vol.30, pp.451-454, 1983

- Y. Yamashita, H. Uchida, **T. Yamashita** and T. Hayashi, "Recent development in detectors for high spatial resolution positron CT," *IEEE Trans. Nucl. Sci.*, vol.31, pp.424-428, 1984

- T. Hayashi, T. Hirohata, H. Uchida, Y. Yamashita ans **T. Yamashita**, "Recent development in photomultipliers for positron CT," In *Proceedings of the 2nd Joint Meeting on Positron Emission Tomography between Japan and Sweden*, Stockholm, 1984

- **T. Yamashita** and T. Hayashi, "A new detector for positron emission tomography," In *Proceedings of the 3rd Joint Meeting on Positron Emission Tomography between Japan and Sweden*, pp.18-19, Kyoto, 1985

- H. Uchida, **T. Yamashita,** M. Iida and S. Muramatsu, "Design of a mosaic BGO detector for positron CT," *IEEE Trans. Nucl. Sci.*, vol.33, pp.889-893, 1986

- K. Shimizu, T. Ohmura, M. Watanabe, H. Uchida and **T. Yamashita**, "Development of 3-D detector system for positron CT," *IEEE Trans. Nucl. Sci.*, vol.35, pp.717-720, 1988

- T. Hayashi and **T. Yamashita**, "New development of photomultipliers for PET," In *Proceedings of Fifth Japan-Sweden Conference on Positron CT*, pp.82-89, Tokyo, 1988

- **T.Yamashita**, "A new high resolution PET for animal studies," In *Proceedings of the Second International Conference on Peace through Mind/Brain Science*, pp.90-97, Hamamatsu, 1989

- N Nohara, **T. Yamashita**, H. Uchida, H. Okada, T. Kurono, E. Yoshikawa and E. Tanaka, "Physical performance of a high resolution PET scanner," *ibid.*, pp.56-67, 1989

- N. Nohara, H. Murayama, M. Endo, T. Yamasaki, H. Uchida, E. Yoshikawa, H. Okada, T. Kurono, **T. Yamashita** and E. Tanaka, "Development of and preliminary results with a high resolution positron emission tomography system," *J. Nucl. Med.*, vol.30(5), p.892, 1989

- M. Yamamoto, N. Nohara, E. Tanaka, T. Tomitani, H. Murayama, N. Satoh, K. Shimizu and **T. Yamashita**, " *ibid..*, vol.30(5), p.746, 1989

- **T. Yamashita**, M. Watanabe, K. Shimizu and H. Uchida, "High resolution block detectors for PET," *IEEE Trans. Nucl. Sci.*, vol.37, pp.589-593, 1990

- **T. Yamashita**, H. Uchida, H. Okada, T. Kurono, T. Takemori, M. Watanabe, K. Shimizu, E. Yoshikawa, T. Ohmura, N. Satoh, E. Tanaka, N. Nohara, T. Tomitani, M. Yamamoto, H. Murayama and M. Endo, "Development of a high resolution PET," *IEEE Trans. Nucl. Sci.*, vol.37, pp.594-599, 1990

- **T. Yamashita**, N. Satoh, K. Shimizu, T. Kosugi, M. Itoh and E. Tanaka, "Development of new imaging technologies," In *Proceedings of the Third International Conference on Peace through Mind/Brain Science*, pp.261-267, Hamamatsu, 1990

- H. Saji, Y. Magata, Y. Yenekura, N. Tamaki, T. Sasayama, J. Konishi, A. Yokoyama, M. Watanabe, H. Okada, E. Yoshikawa and **T. Yamashita**, "Performance characteristics of newly developed positron emission tomography system for animal studies," *J. Nucl. Med.*, vol.38(5), p.1064-1065, 1991

- M. Watanabe, H. Uchida, H. Okada, K. Shimizu, E. Yoshikawa, N. Satoh, T. Ohmura, **T. Yamashita** and E. Tanaka, "High resolution positron emission tomography for animal studies," In *Proceedings of World Congress on Medical Physics and Biomedical Engineering*, p.408, Kyoto, 1991

- M. Yamamoto, N. Nohara, N. Satoh, K. Shimizu, **T. Yamashita** and E. Tanaka, "Time-of-flight positron imaging with eight detctors," *ibid.*, p.406, Kyoto, 1991

- M. Watanabe, H. Uchida, H. Okada, K. Shimizu, N. Satoh, E. Yoshikawa, T. Ohmura, **T. Yamashita** and E. Tanaka, "A high resolution PET for animal studies," *IEEE Trans. Med. Imag.*, vol.11, pp.577-580, 1992

- E. Tanaka, S. Mori, K. Shimizu, E. Yoshikawa, **T. Yamashita** and H. Murayama, "Moving slice septa and pseudo three-dimensional image reconstruction for multi-ring PET," *Phys. Med. Biol.*, vol.37, pp.661-672, 1992

- **T. Yamashita**, "High resolution PET system dedicated to animal studies," submitted to *Pharmaceutical Manufacturing International*, 1993

- E. Tanaka, S. Mori and **T. Yamashita**, "Simulation studies on pseudo three-dimensional filtered algorithm for volume imaging in multi-ring PET," Presented at *1993 International Meeting on Fully Three-Dimensional Reconstruction in Radiology and Nuclear Medicine*, Snowbird, June1993 (will be published in *Phys. Med. Biol.*)

- **T. Yamashita**, "Recent advances in detectors for future PET," In *Proceedings of Second International Symposium on Clinical PET in Oncology,"* (in Press) Sendai, 1993

Other Subject

- H. Nagata, **T. Yamashita**, Y. Iguchi, T. Sugie, H. Kubo and M. Shiho, "Modular-type flat-field grazing-incidence spectrographs for large TOKAMAK (JT-60) plasma diagnosis," *Nucl. Instr. Meth.*, vol.A294, pp.292-298, 1990

- S. Sawaki, **T. Yamashita**, Y. Iguchi et al., "Photoefficiency evaluation of photodcathodes for soft X-ray experiments," *KEK National laboratory for High Energy Physics Photon Factory Activity Report (1982/1983)*, 1983

PATENTS

- **T. Yamashita** and H. Uchida, "Position-sensitive radiation detector," *U.S.A. patent* #4929835 (1990)

- **T. Yamashita**, H. Uchida, K. Shimizu, and T. Ohmura, "A scintillation detector for three dimensionally measuring the gamma-ray absorbing position," U.S.A. patent #4929835 (1990): "A scintillation detector and positron CT apparatus incorporating it," *U.K patent* #2198620 (1990)

- **T. Yamashita**, H. Uchida, and T. Ohmura, "Radiation detector," *U.S.A. patent* #4870280 (1989) : *U.K. patent* #2200205 (1990)

- **T. Yamashita**, "Position-sensitive radiation detector," *U.S.A. patent* #4831263 (1989) : *U.K. patent* #2204769 (1991)

- **T. Yamashita** and K. Shimizu, "Method and apparatus for positioning transformation of projection data for use in positron computed tomography system," *U.S.A. patent* #5003474 (1991) : *U.K. patent* #2231474 (1992)

- **T. Yamashita** and H. Uchida, "Position-sensitive radiation detector," *U.S.A. patent* #4945241 (1990) : *U.K. patent* #2216760 (1992)

- **T. Yamashita**, M. Watanabe, H. Okada and K. Shimizu, "Data correcting device for use with computed tomography apparatus," *U.S.A. patent* #5023894 (1991) : *U.K. patent* #2230927 (1992)

Bibliography Written in Japanese

本論文に関係した解説、技術ノート、研究会、学術講演等

- 林 達郎、山下貴司, "シンチレーション計測用光電子増倍管," 映像情報、vol.9(2), pp.57-61, 1977
- 山下貴司, 林 達郎, "放射線計測用光電子増倍管," 放射線、vol.6(2), pp.64-79, 1979
- 山下貴司, 久米英浩, 山本晃永, "放射線位置検出器," ぶんせき, vol.2, pp.78-84, 1982
- 山下貴司, "放射線検出用光電子増倍管," *O plus E*, vol.53, pp.53-57, 1984
- 山下貴司, 林 達郎, "放射線検出器用光電子増倍管," *RADIOISOTOPES*, vol.33(3), pp.38-45, 1984
- 山下貴司, "ポジトロンCTについて－検出器について," 第17回日本アイソトープ・放射線総合会議 報文集, pp.318-321, 1985
- 山本幹男, 富谷武浩, 野原功全, 田中栄一, 山下貴司, 林 達郎, "タイムオブフライト型ポジトロンCT用高解像力BaF2検出器の検討," 医用画像工学シンポジウム, 1985
- 内田 博, 飯田昌宏, 山下貴司, "二次元位置検出器型光電子増倍管のポジトロンCTへの応用," *Medical Imaging Technology*, vol.4(3), pp.314-318, 1986
- 大村知秀, 山下貴司, 内田 博, 清水啓司 , "BGO位置検出器," 応用物理学会 春季大会, 1988
- 山下貴司, "PETシステムの現状と将来," イオンビーム利用生体機能解明研究会報告, 1989
- 山下貴司, 塚田秀夫, "PET技術の現状と将来展望," 第５回 非破壊生体計測シンポジウム資料, pp.22-25, 1991
- 山下貴司, "高分解能ポジトロンCT開発の現状," 176回 レーザー学会研究会報告, pp.13-18, 1991
- 山下貴司, "PET検出器の現状と将来," 日本医学物理学会 第９回研究発表会抄録集, p.229, 1992
- 山下貴司, "ポジトロン・エミッション・トモグラフィ：最近の装置と検出器," *RADIOISOTOPES*, vol.42, pp.237-243, 1993
- 内田 博, 渡辺光男, 清水啓司, 大村知秀, 佐藤仲弘, 山下貴司, 藤村 卓, 大道英樹, "モザイクBGO検出器の開発及びその応用," 第30回 理工学における同位元素研究発表会要旨集, p.121, 1993

その他

- 山下貴司, 沢木昭弘, 井口裕夫, 前沢秀樹 他, "軟X線検出器－MCP, Siフォトダオード," 応用物理学会 春季大会, 1983

- 沢木昭弘, 山下貴司, 井口裕夫, 前沢秀樹 他, "EUV領域における各種光電面の分光感度特性," 応用物理学会 春季大会, 1983

- 山口政弘, 山下貴司, 山内邦茂, 日野利彦, "VUV領域におけるMCP感度の入射角依存性," 応用物理学会 春季大会, 1984

- 沢木昭弘, 山口政弘, 山下貴司, 斉藤輝文, 小貫英雄, "極紫外領域におけるMCPの特性," 応用物理学会 春季大会, 1984

- 山口政弘, 沢木昭弘, 山下貴司, 斉藤輝文, 小貫英雄, "極紫外領域における各種光電面の分光感度特性," 応用物理学会 春季大会, 1984

- 山下貴司, 杉山 優, 奥山千代志, 山本晃永 他, "真空紫外、軟X線分光分析用多チャンネル検出器," 応用物理学会 春季大会, 1985

- 永田 浩, 木原直人, 浦川文明, 山下貴司 他, "斜入射平面結像分光器," 応用物理学会 春季大会, 1985

- 山下貴司, 杉山 優, 奥山千代志, 山本晃永 他, "プラズマ不純物分光分析用多チャンネル検出器," プラズマ核融合学会 第2回年会, 1985

- 芳本雅彦, 浦川文明, 木原直人, 山下貴司 他, "重金属ドップラー幅測定サブシステム," プラズマ核融合学会 第2回年会, 1985

- 永田 浩, 木原直人, 浦川文明, 萩原雅彦, 山下貴司 他 ; "斜入射平面結像分光器（JT-60,A4-a,d）," プラズマ核融合学会 第2回年会, 1985

- 出野一夫, 仁野和夫, 宮野英治, 山下貴司 他, "軽元素ドップラー幅測定サブシステム," プラズマ核融合学会 第2回年会, 1985

- 岡田裕之, 塚田秀夫, 清水啓司, 山下 貴司、小林 薫, 井上 修, "β-プローブシステムの開発とその評価," 核医学 vol.29, p.823, 1992

(書籍)

- 山下貴司, "光電子増倍管とその用い方," 日本分光学会　測定法シリーズ22 光検出器とその用い方 1章, pp.1-44 （学会出版センター 1991）

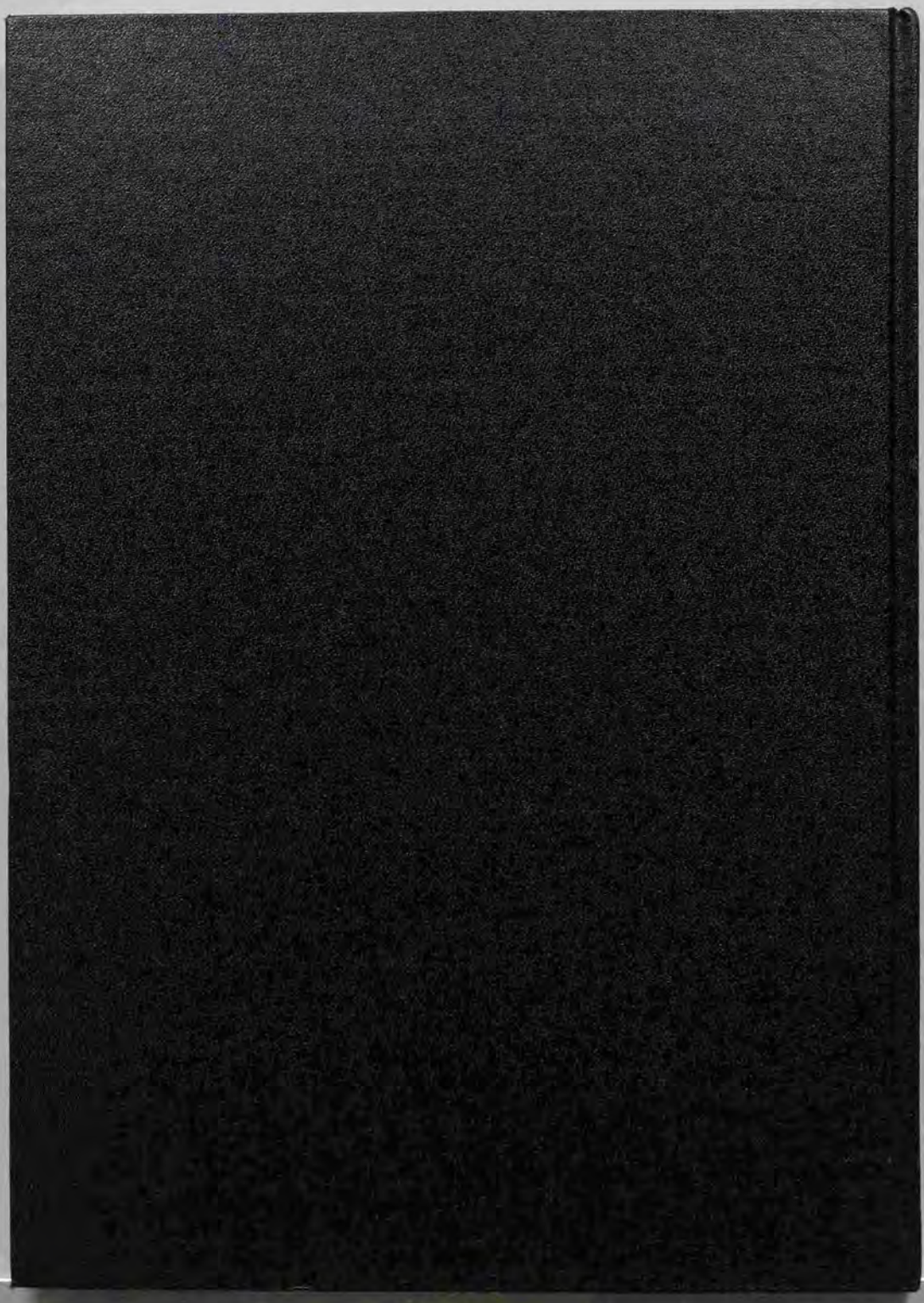

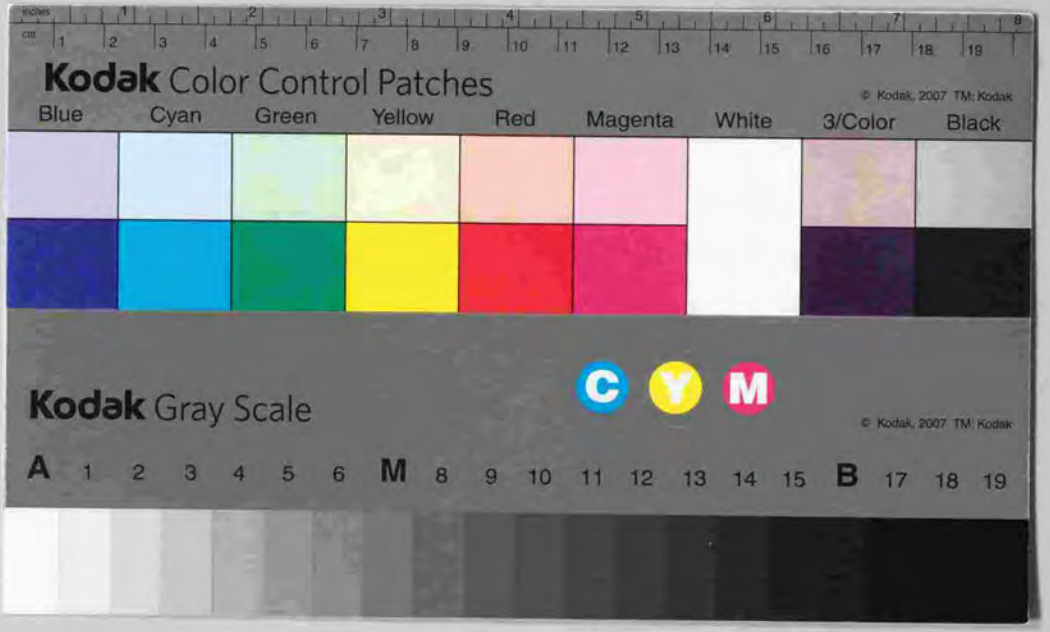
Kodak Color Control Patches
© Kodak, 2007 TM: Kodak
Blue
Cyan
Green
Yellow
Red
Magenta
White
3/Color
Black
Kodak Gray Scale
C
Y
M
© Kodak, 2007 TM: Kodak
A 1 2 3 4 5 6 M 8 9 10 11 12 13 14 15 B 17 18 19